The Sphere Anemometer – Optimization for Atmospheric Wind Measurements

Hendrik Heißelmann

CARL
VON
OSSIETZKY
universität OLDENBURG

Abstract

This thesis deals with the development of a sphere anemometer for the measurements of wind speed and direction in the complex conditions of wind energy and meteorology applications. It is optimized in several development stages regarding its 2D calibration and temporal resolution. Systematic investigations on the impact of tube material and sphere surface properties on the 2D calibration function yield a final development stage of the anemometer.

The assessment in wind tunnel experiments confirms this prototype to be competitive with commercial anemometers regarding the measurement accuracy, precision and temporal resolution. A tilt experiment is performed to mimic vertical wind components and thereby quantify their impact on the cross-flow response of the sphere anemometer. The observed asymmetric response characteristic shows a reduction of the measured wind speeds in down-wind scenarios, which is explained by considerations of the flow around the sphere and its support tube.

Comparative measurements of the sphere anemometer and two commercial anemometers are performed in two different turbulent flow situations. In the first experimental campaign, the sphere anemometer, a cup anemometer and a sonic anemometer are exposed to a reproducible turbulent flow in the wind tunnel, while the second campaign is a multi-day field test in real atmospheric turbulence. The compared wind speed and direction measurements of the sphere anemometer agree well with the sonic anemometer in the wind tunnel. Some deviations are found in the field data for the wind speeds and in particular for the wind directions, as effects of the ambient conditions and the imperfections of the installation site come into play.

Zusammenfassung

Diese Arbeit befasst sich mit der Weiterentwicklung eines Kugelanemometers zur Messung der Windgeschwindigkeit und -richtung unter den komplexen Bedingungen von Windenergie- und Meteorologieanwendungen. Es wird in mehreren Entwicklungsschritten hinsichtlich seiner 2D Kalibrierung und seiner Zeitauflösung optimiert. Der Einfluss der eingesetzten Materialien und Kugeloberflächen wird dabei systematisch untersucht und mündet in einer finalen Entwicklungsstufe des Kugelanemometers. Windkanaluntersuchungen bestätigen, dass dieser Prototyp in Bezug auf Zeitauflösung und Messgenauigkeit mit kommerziellen Anemometern wettbewerbsfähig ist. Der Einfluss von vertikalen Windkomponenten auf das Kugelanemometer wird in einem Neigungsexperiment quantifiziert. Ein asymmetrisches Antwortverhalten wird dabei beobachtet und mittels der Strömung um die Kugel und ihre Halterung erklärt.

Um Kenntnisse über die Leistungsfähigkeit des Kugelanemometer zu gewinnen, werden vergleichende Messungen mit zwei kommerziellen Anemometern in turbulenten Strömungen durchgeführt. Dazu werden das Kugelanemometer, ein Schalensternanemometer und ein Ultraschallanemometer zunächst in einer künstlichen, turbulenten Anströmung im Windkanal untersucht und anschließend in einem mehrtägigen Freifeld-Experiment realer, atmosphärischer Turbulenz ausgesetzt.
Die mit dem Kugelanemometer und dem Ultraschallanemometer gemessenen Windgeschwindigkeiten und -richtungen stimmen in den Labormessungen gut überein. In den Freifeldmessungen zeigen sich hingegen einige Abweichungen, die insbesondere bei der Windrichtungsmessung zu Tage treten. Sie können auf die Umgebungsbedingungen und die baulichen Gegebenheiten des Installationsorts zurückgeführt werden.

Contents

List of Figures

List of Tables

Chapter 1

Introduction

1.1   Motivation and Objective

The worldwide demand for energy is projected to increase by 48% from 2012 to 2040 [EIA, 2016]. As the vast majority of countries committed to the Paris climate accord in 2015, the need for renewable energy sources to play a major role in the future energy supply is undeniable. Renewables are the fastest growing source of electric energy and wind energy in particular is one of its most powerful contributers. Hence, wind energy is of paramount importance to achieve the climate protection goals while coping with mankind's growing demand for electricity.

Wind energy projects vary in size and type, ranging from single wind turbines to large wind farms at on-shore and off-shore sites. All of these projects rely on the wind resource itself and a thorough site assessment is crucial for the estimation of the wind power generation of a wind turbine or wind farm. Even small errors in the wind speed measurements can make a significant difference in terms of the annual energy production due to the cubic relation between wind speed and wind power. Accurate knowledge of the prevailing wind conditions on-site is thus paramount for the estimation of the expected annual energy production and consequently the generated revenue of any wind energy project.

The site assessment and the characterization of the wind turbine's power curve are typically performed in measurement campaigns with conventional anemometers installed on meteorological masts. However, the emergence of ground-based remote sensing techniques, such as Light Detection And Ranging (LiDAR), can change this practice in the future. In any case, it is important to minimize the errors in the wind speed and wind direction measurements.

Today, mainly cup anemometers are used for wind resource assessment. Developed in the 19th century, their design is intriguingly simple: A vertical axis rotor with attached cups is rotating due to the horizontal wind speed and its rotational frequency is proportional to the wind speed. Cup anemometry has been intensively investigated over the years and several issues have been identified [Wyngaard, 1981]. Most notably, cup anemometers suffer from the effects related to their rotational mea-

suring principle: the wear-out of bearings and the high moment of inertia. These issues have been investigated since the 1920s [Schrenk, 1929] and optimizations nowadays focus mostly on the design of the light-weight rotors and the conical shape of the cups, in order to reduce inertial effects and mitigate the unfavorable over-speeding [Strangeways, 2003; Deacon, 1951; Kristensen, 1993].

During the last decades, sonic anemometers evolved into an alternative to cup anemometers. They make use of the velocity-dependent time shift, which is experienced by an ultrasonic wave when it passes through the measurement volume. Sonic anemometers can provide a higher temporal resolution than cup anemometers and lack any wearing parts. The combination of several transducer pairs additionally allows for the measurement of all three velocity components of the wind, i.e. horizontal wind speed, wind direction and vertical wind speed. The required ultrasonic transducers are, however, more vulnerable to mechanical disturbances as even small misalignments of the transducers may prevent the anemometer from correct measurements. For years, cup anemometers were the only certified sensors for the measurement of the wind conditions during site assessment and for the characterization of a wind turbine's power curve according to the IEC standard 64100-12-1 [IEC, 2005]. The latest revision of the standard, however, includes sonic anemometers as an alternative sensor for those purposes [IEC, 2015]. Although it even allows for the use of ground-based LiDARs for the power curve characterization in flat terrain, those are required to be complemented by conventional anemometers on a nearby met-mast.

Motivated by the shortcomings of the established anemometers for atmospheric applications, the sphere anemometer has been developed at the University of Oldenburg as an alternative. The employed principle of drag-based flow measurements is not entirely new and various attempts have been made in the past to incorporate it in an anemometer setup [Smith, 1980; McNally, 1970; Kirwan et al., 1975]. Nevertheless, none of those anemometer prototypes could be established and most of them disappeared shortly after their introduction.

The aim of the sphere anemometer is to combine the robustness of cup anemometers with the sonic anemometers' capability of wind speed and direction measurements at a high temporal resolution. The concept pursued at the University of Oldenburg relies therefor on a highly resolving laser measuring technique to detect the drag-dependent displacement of a sphere. Conceptual studies have been performed at the University of Oldenburg in the past and a first prototype of this sphere anemometer for two-dimensional measurements has been realized [Heißelmann, 2008]. It constitutes the basis for the further developments.

The objective of this thesis is the optimization of the sphere anemometer towards its application in atmospheric field measurements. It is therefore essential to characterize the issues of the existing sphere anemometer prototypes and improve it based on the gained insights. A systematic investigation of the different design parameters of the sphere anemometer, in particular the sphere surface patterns and the tube material, is thus indispensable. The knowledge of these properties and their im-

pact on the sphere anemometer can than be employed for the improvement of the sphere anemometer setup. It is therefor crucial to achieve a reliable and unique two-dimensional calibration function and a sufficiently high natural frequency of the mechanical setup.

Once the design parameters are found, the setup can be adapted to the application in the complex outdoor conditions by making it weather-proof.

In a final step of this thesis, the sphere anemometer prototype is characterized in detail by means of wind tunnel experiments, before a field measurement campaign is performed as a proof of its capability to operate in atmospheric wind conditions.

1.2   Structure of this Thesis

This thesis starts in Chapter 2 with a brief introduction of the velocity measurement techniques used during the course of this work. Methods for pressure measurements using mechanical and electrical gauges will be introduced as well as the commonly used hot-wire anemometry. Moreover, cup and ultrasonic anemometers as the two mostly used commercial wind speed sensors for meteorological applications are described. A selection of previously developed drag-based anemometers – mainly spherical anemometers of different kinds – is also presented to provide a historic overview of the topic.

Chapter 3 introduces the general operational principle of the sphere anemometer and the laser-based measuring technique in particular. Basic properties of the flow around a sphere and its implications on the generated drag will be explained and properties and issues of the previous sphere anemometer prototypes developed at the University of Oldenburg are summarized. It is followed by a brief overview of the design criteria for the sphere anemometer development in Chapter 4. Key features like the measuring range and resolution are treated as well as the expected calibration function. The entanglement of different design parameters is explained to assist in the selection of proper materials and geometry for the sphere anemometer setups.

Constituting the starting point of the further development of the sphere anemometer towards a robust and reliable sensor for wind energy applications in complex environments, the 1st generation sphere anemometer is presented in Chapter 5. Its sensor setup is described in detail and its characteristics are concluded from calibration measurements and spectral analyses. Particular emphasis is given to the identification of the impact of the tube material and the sphere surface on the 2D calibration.

These findings trigger modification of the mechanical setup, which are embodied in the 2nd generation sphere anemometer, specified in Chapter 6. It can be considered an intermediate development stage, before a further improvement of the setup towards field applications is made in the final development stage – the 3rd generation sphere anemometer. A description of the changes made and a detailed analysis of the sensor properties is presented in Chapter 7. Special emphasis is given to the accuracy, precision and the resolution of the sphere anemometer as well as its response to up-

and down-wind components.

Turbulent inflow under laboratory conditions is used to compare the performance of the 3$^{\text{rd}}$ generation sphere anemometer with commercial cup and ultrasonic anemometers. The results of these measurements are presented in Chapter 8. In a further assessment of the anemometers, a field test is carried out with these three sensors. Preparative investigations and the actual wind speed and direction measurements on-site are addressed in Chapter 9.

Finally, Chapter 10 concludes this thesis as it summarizes the different stages of the sphere anemometer development and the findings from the various wind tunnel and field experiments. An outlook at the future of the sphere anemometer is attempted and some investigations and modifications for the further advancement of the sensor are recommended.

Chapter 2

Reference Sensors for Laboratory and Field Applications

This chapter will give a brief introduction to the anemometers, which served as reference sensors for the evaluation of the sphere anemometer prototypes during the wind tunnel measurements presented later on in Chapters 5–8. Additionally, the most common techniques for atmospheric wind measurements in wind energy and meteorology applications will be introduced as they were used for comparison during wind tunnel and field testing of the sphere anemometer (Ch. 8 & 9). The focus will be on invasive sensors such as cup anemometers and sonic anemometers. For information on non-invasive laser-based methods (LDA, PIV) and remote sensing techniques (LiDAR, SoDAR) it is referred to literature, e.g. Ruck [1987]; Raffel et al. [2007]; Werner [2005].

2.1   Reference Sensors for Wind Tunnel Applications

One of the crucial demands for the development and characterization of wind speed and wind direction sensors is the choice of proper reference anemometers for the evaluation. The question of which reference anemometer should be used cannot be generally answered, since each type of anemometer has certain features, like resolution, accuracy, and many others. Whether an anemometer feature is considered advantageous or a limitation is subject to the field of application. For example, a highly resolving hot-wire anemometer may be suitable for the assessment of the quality of other small sized laboratory anemometers, such as a 2D-LCA [Barth, 2004; Hölling, 2008; Puczylowski, 2015] or an NSTAP (Princeton probe) [Bailey et al., 2010]. However, it may be a case of comparing apples and oranges if miniaturized anemometers are used for comparison with larger meteorological sensors or even remote sensing devices such as LiDARs or SoDARs. A comprehensive assessment of an anemometer needs to cover different features and can therefor only be achieved by comparison to different reference sensors.

Moreover, the accuracy of any wind tunnel experiment or calibration of anemometers

is limited by the reproducibility of the wind tunnel reference speed and the accuracy of the used reference sensors. Although some sensors, such as Laser Doppler Anemometers (LDA), do not require calibration with reference sensors, still the accuracy is what determines the quality of the results obtained from their application. Thus, the choice of well-adjusted and calibrated reference sensors is crucial for the reliability of any wind tunnel study.

The subsequently presented studies will rely on the widely used and very well established pressure sensor technology as a calibration reference in laminar flows. Although semiconductor pressure gauges can allow response times in the range of 1 kHz or even faster, pressure sensors typically feature a lower temporal resolution. This can be mainly attributed to the tube connections which result in a low-pass filtering depending on the length and diameter of the used tubings. For common wind tunnel applications, temporal response times in the order of 10–100 ms may be achieved which makes pressure gauges less suitable for the use in turbulent flows. For these cases, highly resolving hot-wire anemometers are chosen for comparison. Both techniques will be briefly presented hereafter, but for more details, the reader is referred to standard literature, e.g. by Bruun [1995]; Eckelmann [1997] or Baker [2000].

2.1.1 Pressure Sensors

Pressure sensing can be considered a standard measurement technique for a wide range of applications in laboratory flows. According to Bernoulli's Equation

$$\underbrace{\frac{\varrho}{2}u^2}_{p_\mathrm{d}} + \underbrace{\varrho g z_0 + p_0}_{p_\mathrm{s}} = const \tag{2.1}$$

$$p_d + \quad p_s \quad = p_t \tag{2.2}$$

the total pressure p_t along a trajectory of constant velocity (a stream line) can be considered constant for the case of incompressible flows and is given as the sum of the static pressure p_s and the dynamic pressure p_d. For Mach numbers $Ma \leq 0.3$, i.e. fluid velocities smaller that 30 % of the speed of sound, the above stated simplified Bernoulli Equation (Eq. (2.1)) is valid and can be used to determine the wind speed u along a stream line from the pressure p_d in a fluid flow of constant density ϱ [Baker, 2000]. This will be the case for all pressure measurements treated within this work.

Practically, pressure sensors often consist two parts: A probe with one or more pressure holes which is placed in the flow and a sensing device such as a manometer or an electrical transducer. So-called Pitot probes feature a single hole at their tip, which is to be aligned such that it coincides with the front stagnation point of the flow around the device. The pressure at the front stagnation point is equal to the total pressure p_t. While Pitot tubes possess only a single pressure hole, Pitot-static tubes feature an additional ring (or a set of connected holes, cf. Figure 2.1) located about 4–5 probe diameters downstream the tip [Eckelmann, 1997]. This type of probe is also often referred to as Prandtl tube, originating from the special design Ludwig Prandtl developed for it during the early 20th century. For visualization purposes, the concept of
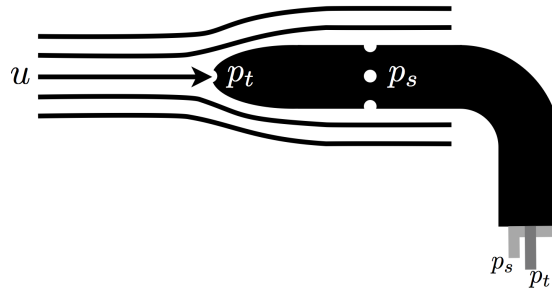
Figure 2.1: Sketch of the Pitot-static tube probe head. The total pressure p_t is obtained at the front stagnation point (arrow) and the static pressure p_s is measured via a set of holes downstream the probe tip.

stream lines, which can be used for laminar flow situations, is adapted here. Each stream line marks the trajectory of a infinitesimal fluid element with a fixed flow velocity. The downstream pressure holes are aligned perpendicular to the stream lines of the flow around the tip of the Prandtl tube and thus allow for the detection of solely the static pressure p_s.[1] The differential pressure, which in fact is the dynamic pressure $p_d = p_t - p_s$, can be measured and thus the flow velocity can be calculated accordingly from Equation (2.3)

$$u = \sqrt{\frac{2 \cdot p_d}{\varrho}}.$$ (2.3)

The probe head of the Pitot-static tubes has to be carefully aligned with the main flow direction. Otherwise flow distortions may occur which can clearly affect the measurement of the static pressure at the pressure holes downstream the probe tip. The severity of such flow distortions depends on the geometry of the probe tip and the downstream distance of the static pressure holes. Squared probe tips are less prone to flow distortions and offer an larger acceptance angle than Prandtl probes, which feature acceptance angles of about ±10°, while hemispheric tips are even stronger affected [Eckelmann, 1997; Baker, 2000]. Pressure readings obtained with Pitot-static probes may be subject to errors stemming from different sources, like placement close to boundary layers or too low flow velocities. These errors may vary depending on the design of the probe tip as may blockage effects and flow accelerations around the tip. The Prandtl probe design used for many measurements presented within this work has been designed by Ludwig Prandtl in an effort to achieve error cancellation by carefully choosing the probe dimensions and the downstream distances of the pressure holes and support tube [Baker, 2000].

Pitot- and Prandtl probes cannot measure the flow velocity by itself, but have to be connected to a manometer or pressure sensor. Classical setups employ different types of liquid manometers, such as U-tube manometers or inclined tube manometers with one or more fluid columns. These manometers may display several pressure chan-

---

[1]Note that the static pressure p_s is not equivalent to the hydrostatic pressure at height z_0, $p_g = \varrho g z_0$, due to Eq. (2.1).

nels at the same time, but the readings are usually obtained manually or by means of image analysis techniques. Their analog nature makes them unfeasible for most of today's measurement applications, in particular considering the comparably low temporal resolution of less than 1 Hz and the low degree of measurement automation. Thus, pressure probes are mainly used in combination with fast pressure transducers utilizing either small deforming diaphragms or solid state piezoelectric sensors. Both types provide high time resolutions in the order of 100 Hz or even 1 kHz, respectively. These sensors usually maintain their calibration over a long time and their electric output can be directly connected to the used analog-digital (AD) conversion system. The piezoelectric system is employed in the Setra C239 pressure gauges [Setra Systems Inc., 2013], which are used for the comparisons throughout this work.

The differential pressure measurement via Prandtl tube is practically carried out directly within the pressure gauge or manometer. Therefore, the total pressure tubing is connected to one side of the detector and the static pressure tubing to the other one. In case of the liquid manometer, both pressure connections are separated internally by the liquid column, which is consequently shifted due to the pressure difference p_d between the connections. The dynamic pressure p_d can either be directly read (as for a Betz manometer) or has to be calculated from the height difference z of the liquid with density ϱ_{liq}. For the inclined tube manometer used during some measurements within this work, p_d and consequently the flow velocity can be obtained by

$$
\begin{aligned}
p_{\text{d}} \quad &= \quad \frac{\varrho}{2}\,u^2 \\
&= \quad \varrho_{\text{liq}}\,g\,z\,\xi \\
\Rightarrow u \quad &= \quad \sqrt{\frac{2\,\varrho_{\text{liq}}\,g\,z\,\xi}{\varrho}}.
\end{aligned}
\tag{2.4}
$$

Here, ϱ and g denote the air density and gravitational constant, respectively, while ξ is an inclination factor of the manometer.
Electric pressure gauges function quite similarly with both tubing being separated either by the diaphragm or the piezo element. The reading of the transducer is usually a voltage or current signal which has to be translated to a pressure via the device's calibration function. It can than be converted to a velocity using Equation (2.3).

Pressure measurements are not independent of the air density ϱ, as is evident from Equations (2.3) and (2.4). The actual air density can be calculated from the ambient pressure and temperature readings using

$$
\varrho = \frac{p}{R_h \cdot T}
\tag{2.5}
$$

with gas constant of humid air

$$
R_h = \frac{R_s}{1 - rH \cdot p_d/p \cdot (1 - R_s/R_v)}.
\tag{2.6}
$$

Here, R_s and R_v are the specific gas constants of dry air and water vapor, respectively. T and rH are the absolute temperature and relative humidity of the air and p is the hydrostatic pressure.

2.1.2 Hot-wire Anemometry

Hot-wire anemometry is probably the most used measurement technique for flow measurements under laboratory conditions. The small probe head of the sensor consists of an electrically conducting wire which is spanned between the tips of a pair of prongs. The prongs are connected to a regulated supply voltage, causing the wire to heat up due to the applied current I. Since any metallic wire material changes its resistance R_{hw} with temperature, once the hot-wire is exposed to the flow, the thermal transport of the fluid causes the wire to cool down depending on properties like temperature of fluid and wire and the flow velocity u. A Wheatstone bridge circuit is used to measure the changing resistance of the wire. In order to relate the bridge output voltage Q to the flow velocity, a calibration function of the hot-wire system has to be performed. The resulting calibration function can be fitted by a 4th order polynomial

$$u = u_0 + a_1 Q + a_2 Q^2 + a_3 Q^3 + a_4 Q^4 \qquad , \qquad (2.7)$$

where u is the wind speed and the parameters $a_1 \ldots a_4$ are obtained from the fitting.

Hot-wire anemometers can be either operated in constant current mode (CCA) or constant temperature mode (CTA), which is used for all applications throughout the presented work. A single hot-wire or hot-film sensor can only be utilized to measure the magnitude of the flow velocity without directional information, since all parts of the wire contribute equally to the thermal transport. However, several differently oriented wires can be combined to one multi-component sensor, permitting the calculation of two (for a x-wire) or three (for a three or more wires) components of the flow velocity. While these multi-wire probes can be very useful for the detailed characterization of turbulence and near wall flows, only single hot-wires were used as reference anemometers in the presented work.

The hot-wire anemometer's spatial resolution is determined by the sensor dimensions, i.e. the length of the wire for a single hot-wire or the spatial extent of the probe prongs for multi-wire probes. Even for single wire probes, the wire length may vary significantly from several millimeters down to fractions of a millimeter. The probe dimensions are mainly dictated by the field of application and the wire's length-to-thickness ratio, which should not exceed $l/d = 200$ [Bruun, 1995]. The standard Dantec Dynamics 55P01 single wire probes used within the presented work consist of a gold-plated tungsten wire with a 1.25 mm long active length and a thickness of 5 μm, resulting in $l/d = 250$.

Hot-wires are in general quite filigree probes due to the filament, which may be easily broken by mishandling or even by larger particles suspended in the flow. In order to avoid rapid breakage of the hot-wire probe in more hostile environments such as water and atmospheric flows, hot-film probes are usually preferred. While the general sensor principle is equivalent to hot-wires, their mechanical stability is increased by using thicker, metal-coated quartz cylinders instead of single wires. Electric insulation from the flow is also achieved by additional coatings. The thermal inertia of the wire as well as the response time of the used electronics impacts the temporal

resolution of the hot-wire anemometer. Thus, it is only logical, that smaller hot-wires feature a higher temporal resolution and that on the consequently the added stability of hot-film probes yields a reduced temporal resolution compared to hot-wires of the same size.

Hot-wire anemometers served only as a reference for turbulent laboratory measurements presented in Chapter 8 of this work, because of the above mentioned issues regarding robustness in outdoor applications. In these cases, the commercial Dantec 55P01 hot-wire probes were operated with the Dantec StreamLine® 90S10 frame and the Dantec StreamWare® software (version 3.1) [Dantec Dynamics A/S, 2003]. All outdoor reference sensors were either cup or sonic anemometers described in the following Sections 2.2 & 2.3.

2.2   Cup Anemometer & Vane

The most used anemometers in meteorological applications and in wind energy are cup anemometers. The invention of the cup anemometer dates back to 1845 when J. T. R. Robinson[2] first used a four-armed vertical axis rotor with hemispherical drag bodies fixed to its tips [Wyngaard, 1981; Strangeways, 2003]. While the sensor principle remained widely unchanged during the last decades, the dimensions of the cup anemometers decreased significantly from about $L = 2$ m diameter of Robinson's anemometer to $L = 0.1–0.2$ m in modern types allowing for faster response times and improved spatial resolution. Figure 2.2 shows two state-of-the-art cup anemometers from *Vector Components* and *Thies Clima* as an example.

Measuring Principle

Cup anemometers make use of the drag force F_D acting on the cups which are mounted to each tip of the vertical axis rotor. The drag force caused by the wind speed u on a body of cross-section A is given by

$$F_D = \frac{1}{2} \cdot \varrho \cdot c_D \cdot A \cdot u^2, \tag{2.8}$$

with air density ϱ and dimensionless drag coefficient c_D. The different shapes of the closed side and the open side of the cup yields different drag coefficients c_D, i.e. different drag forces F_D. This translates into a torque differential, which causes a rotation of the rotor with a rotational frequency ω proportional to the prevailing wind speed u [Eckelmann, 1997]

$$\omega \propto u. \tag{2.9}$$

The measurement of the rotational frequency is mostly done in common anemometers using either light barriers, magnetic reed relays or hall sensors. Some lower quality cup anemometer models still use mechanical potentiometers to measure the rotation, but these are outdated due to unavoidable wear-out. The sensor output can

---

[2]John Thomas Romney Robinson, 1792–1882

either be a pulsed (frequency), current or voltage signal and is usually factory-set by the manufacturer upon request. The pulsed output is favorable for any application with constraints of the power consumption, as they often occur in field campaigns.
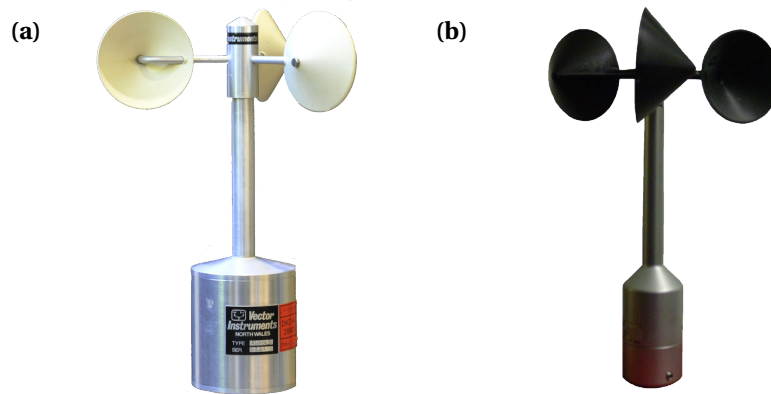
Figure 2.2: Photos of two state-of-the-art cup anemometer models with three cups (not to scale). (a) Vector Components model with conical plastic cups on a three-armed wire rotor. (b) Thies First Class Advanced cup anemometer with three conically shaped cups on a lightweight carbon fiber rotor. The rotor features tilted cups and horizontal extensions to minimize the effect of cross-flows.

Properties and Issues of Cup Anemometers

Typically, the response of an anemometer is characterized by the time τ the anemometer needs to reach 63% (1/e) of the maximum value of a velocity step Δu. However, MacCready and Jex [1964] showed that a better characterization of cup anemometers can be achieved by using the concept of a distance constant l_0 instead, which is linked to τ via Taylor's hypothesis, $l_0 = u \cdot \tau$. The distance constant l_0 can be considered a measure of the reaction of a cup anemometer being initially in equilibrium at a velocity u when it is exposed to a velocity step of magnitude Δu. Practically, the distance constant l_0 corresponds to the length of a fluid column which passes the anemometer until it reaches 63% of the value of the wind speed step $u + \Delta u$ [MacCready and Jex, 1964; Wyngaard, 1981; Kristensen, 1999]. Although the distance constant does not depend on the actual (mean) wind speed, it may differ significantly between various cup anemometer types. The Risø WindSensor for example is listed with $l_0 = 1.8$ m, while the significantly cheaper NRG 40C anemometer's distance constant is a mere 50% larger at $l_0 = 2.55$ m.

Although the cup anemometer is widely used in wind energy and meteorology, there are several shortcomings of these sensors – amongst them the lack of direction measurement, the vulnerability to vertical flows and the wear of mechanical parts like bearings. Still, the most significant problem of cup anemometry is the so-called over-speeding, which constitutes the over-estimation of the wind speed under turbulent conditions. Over-speeding is caused by the asymmetric characteristics of the

drag forces for increasing and decreasing wind speeds u with it's severity depending on the rotor design and inertia. This issue has been very well known for decades and many models for the description have been developed, e.g. by Schrenk [1929]; Kaganov and Yaglom [1976]; Busch and Kristensen [1976] and Wyngaard [1981], but since the asymmetric characteristics of the anemometer is an intrinsic feature of its principle of operation, it will never be entirely avoided. Nevertheless, many attempts of improvement have been carried out over the years. A lot of research has been done on the number and the shape of the cups aiming at a reduction of the inertial forces of the rotor and faster response dynamics. Nowadays rotors of advanced cup anemometers usually consist of a three-armed rotor made of light weight materials, e.g. carbon fibers, since they provide a more constant torque over a single revolution [Strangeways, 2003]. They mostly employ conically shaped cups, which provide better characteristics and less vulnerability to turbulent wind speed fluctuations than hemispheres [Deacon, 1951]. Special designs of the rotor bars are also often pursued in an attempt to reduce the impact of cross-flows on the cup anemometer readings.

Additionally, anemometer specific correction schemes for the impact of over-speeding on the wind measurements have been developed and are usually applied on the measured data [Kristensen, 1993, 1998; Hristov et al., 2000].
As already mentioned, cup anemometers only allow for the measurement of the horizontal wind speed magnitude and do not provide any directional informations. Tho overcome this shortcoming of the anemometer principle, cup anemometers are usually complemented with an additional direction sensor, mostly a vane. The wind vane translates a change of wind direction into a rotational motion, which can be measured in a similar way as described for the cup anemometer rotation itself. Since a second sensor is utilized, the wind speed and direction measurements are not obtained at the same point in space[3], but from two spatially separated points. This makes the combination of cup anemometer and vane inappropriate for some applications, e.g. the measurement of fluxes.
Among today's commercially distributed anemometers, cup anemometers and vanes constitute the most used type. This is on the one hand due to its very simple principle of operation and the rather low pricing of high-end cup anemometers. On the other hand, no other anemometer (or combination) could be used as reference anemometer for certification purposes according the International Electrotechnical Commission standard 64100-12-1 [IEC, 2005, Ch. 6.2] for years. Only a recent revision of the IEC standard 64100-12-1 (Ed. 2) allowed sonic anemometers and LiDAR techniques for the wind resource assessment and power curve measurement, which is required for wind turbine installation and financing [IEC, 2015].

---

[3]No measurement is performed in a single (perfect) point, but the effect of integration over the sensor volume is neglected here.

2.3 Ultrasonic Anemometers

In order to avoid the shortcomings of the cup anemometers – e.g. the low temporal resolution and the lack of direction measurements – ultrasonic anemometers can be used for wind speed measurements. Ultrasonic anemometers (often just called sonic anemometers) have been applied in meteorology for years and lately are gaining ground in wind energy applications as well. They can provide measurements of several components of the wind speed depending on their design.

Measuring Principle

There are three different principles of sonic anemometer operation, which are used for various applications. The most used sonic anemometers employ the run-time method to determine velocities along the sound path [Baker, 2000]. For this purpose two combined emitter-receiver-modules – so-called transducers – are aligned opposing each other in a known distance d, as sketched in Figure 2.3 (a). The time of flight of the acoustic wave traveling from the emitting transducer T_1 to the receiving transducer T_2 is measured when it is oriented with the flow direction (t_1) and when it is oriented against it (t_2). The difference in time of flights is used to calculate the line of
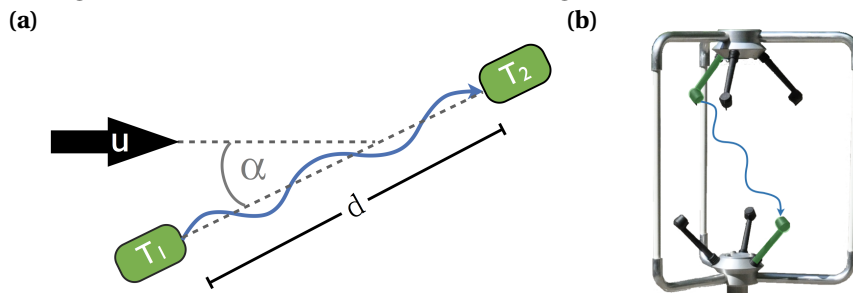
Figure 2.3: (a) Sketch of the sound path between two transducers, which are inclined to the flow direction by an angle α. A sonic pulse (blue) sent between one pair of transducers (green) is used to detect the velocity along the transducer axis. (b) Sensor head of the Gill 3D sonic anemometer with three pairs of inclined transducers.

sight velocity along the transducer axis according to

$$u = \frac{d}{2} \cdot \left(\frac{1}{t_1} - \frac{1}{t_2} \right) \cdot cos(\alpha).$$

(2.10)

If the flow direction is inclined with respect to the transducer axis, only the projection on the sound path is obtained. The inclined transducer alignment can be utilized by combining two or three transducer pairs, which allows for the simultaneous measurement of two or three velocity components, respectively. This technique was for example realized in the commercial Gill WindMaster 3D sonic anemometer shown in Figure 2.3 (b).

Two alternative techniques of ultrasonic anemometry are used for some applications. They will be briefly introduced for completeness in the following, but constitute

only a niche.

The first of these methods to use ultrasonic signals for the detection of flow velocities is based on the Doppler shift of the scattered signal from tracer particles suspended to the flow. These tracers can either be artificially seeded, e.g. glass spheres in a Rayleigh-Bénard system, or be of natural descent like aerosols in the atmosphere. The scattered sonic wave is Doppler shifted once it interacts with the particles and by overlaying the backscattered signal with the reference sonic signal, a Doppler shift frequency is obtained. This Doppler frequency f_D is directly related to the line of sight velocity of the reflecting particle,

$$u = \frac{c}{2} \cdot \frac{f_D}{f_S},$$
(2.11)

which is assumed to be traveling with the speed of the surrounding fluid. Here, f_S denotes the sonic frequency of the emitter and c is the speed of sound. While this principle is rarely used for atmospheric sonic anemometer applications, it is widely used for the remote sensing LiDAR devices (Light Detection And Ranging).

As a second alternative, sonic anemometer based on acoustic resonance have been recently developed for wind energy applications. These anemometers use piezoelectric actuators to create a standing acoustic wave inside a horizontally aligned cavity. The flow across the cavity alters the phase of the sonic signal, which in turn is readjusted by the piezoelectric actuators to conserve the standing wave. Thus, the flow velocity can be concluded [FT Technologies Ltd., 2015].

Since no anemometer used for the presented work employed these two alternative principles, the following sections will only treat properties of common time-of-flight sonic anemometers like the Gill WindMaster Pro [Gill Instruments Ltd., 2009].

Directional Bias and other Error Sources

Some sonic anemometer setups have been known to systematically distort the flow due to their sensor design and the alignment of the transducers and support structures. Wiesner et al. [2001] have investigated the angular dependency of these flow distortions for five different anemometers manufactured by Kaijo Denki, METEK and Gill Instruments Inc. Their study included the comparison of three different sensor head designs made by Kaijo Denki, amongst them a three component anemometer with predominant acceptance direction featuring two horizontal sound paths and one vertical sound path. A combination of a two-dimensional sensor head with vertical sound path and a one-dimensional transducer pair with vertical alignment was employed in another anemometer head, while the third anemometer head consisted of three transducer pairs whose sound paths were tilted against the horizontal and vertical direction – much like it is shown in Figure2.3 (b). Wiesner et al. concluded from the comparison of these different sensor head concepts, that the least deviations from the reference wind speed occurred for the combination of three tilted sound paths in one sensor head. Besides the three Kaijo Denki anemometers, they also investigated the flow distortion produced by a Gill 3D Research anemometer - with the

anemometer showing the least distortions of all tested devices. This is of particular
interest, since the sensor geometry is similar to the one of the Gill 3D WindMaster Pro
anemometer used for the investigations in this work.

The Gill 3D WindMaster Pro 3D employs three pairs of transducers, which are sym-
metrically aligned as sketched in the top view in Figure 2.4. The sensor head has
three support structures, which are located along the north direction (north spar)
and ±120° apart. The measurement volume is entirely enclosed in the sensor head.
The WindMaster Pro features an internal calibration correction scheme, which can
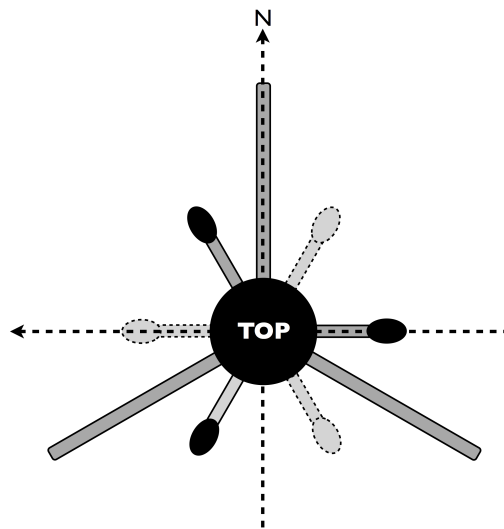
Figure 2.4: Top view of the transducer alignment inside the sensor head of the Gill 3D Wind-
Master Pro anemometer (nt to scale). The solid transducers are on top of the measurement
volume, while the dashed counterparts are at the bottom. The three support structures are
120° apart and enclose the transducers with one support coinciding with the north align-
ment. The coordinate system indicates the direction of positive Cartesian wind speed com-
ponents in the horizontal plane.

be switched on and off via the user interface of the anemometer.

2.4   Drag Force Anemometers

Besides the above mentioned cup and sonic anemometers, which are today's stan-
dard anemometers in wind energy and meteorology applications, a couple of dif-
ferent approaches have been made on the development of drag force anemometers.
Starting in the 1960s, Reed III and Lynch [1963] proposed a spherical anemometer for
the measurement of the dynamic pressure (thus also wind speed) at a NASA rocket
launch site. Two types of anemometers were investigated: the one-dimensional "Ping-
Pong Ball Anemometer" and the two-dimensional "Hole Ball Anemometer". The "Ping-
Pong Ball Anemometer" utilized a commercially available load cell to which a ping
pong ball with smooth surface was mounted. In case of the "Hole Ball Anemometer"

a sphere with about 90 mm diameter and about 16 mm large holes was fixed to a vertically mounted tube of 31 mm diameter. Both anemometer types used metallic strain gauges in a Wheatstone bridge circuit [Hoffmann, 1987] for the detection of the acting drag force.

Based on the idea of Reed III and Lynch, Norwood et al. [1966] later designed a drag based sensor using a hole ball in combination with semiconductor strain gauges (Figure 2.5). The advantage of semiconductors over conventional metallic strain gauges is an up to 60 time higher sensitivity. Despite their ability to detect smaller material strains, they exhibit several disadvantages, among them are higher costs and difficult handling. But mainly the non-linear signal characteristics and temperature dependence causes problems which make them unfeasible even for many of today's industrial applications [Hoffmann, 1987]. Norwood et al. also tested a setup including a cylindrical drag body, but they favored the spherical body since it is less prone to vertical flow components due to the higher degree of symmetry [Norwood et al., 1966].
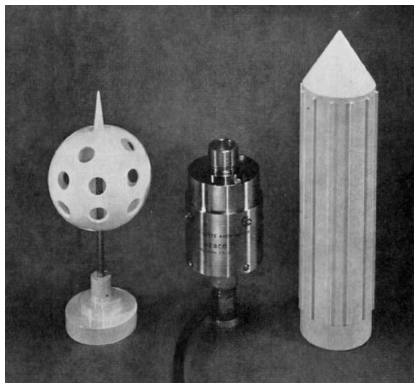
Figure 2.5: Drag based Hole Ball Anemometer by Norwood et al. [1966] utilizing semiconductor strain gauges in a force cell with interchangeable drag bodies. Taken from [Norwood et al., 1966, p. 888, Fig.1]. ©American Meteorological Society. Used with permission.
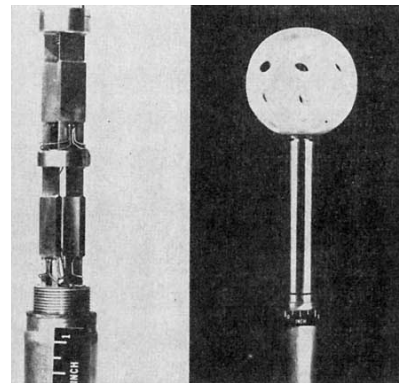
Figure 2.6: Photo of drag based Ping-Pong Ball Anemometer by Reed III and Lynch [1963]. Taken from [Reed III and Lynch, 1963, p. 413, Fig.2; p. 415, Fig.6]. ©American Meteorological Society. Used with permission.

In 1980, Smith made another attempt to construct a sphere anemometer, mounting the spherical drag body on top of a vertical rod which was supported by several springs. The displacement of the sphere was translated via the rigid rod and detected by means of proximity sensors instead of strain gauges.

In contrast to the above mentioned approaches, McNally [1970] and later on Kirwan et al. [1975] designed a drag based anemometer consisting of a perforated polystyrene sphere, which was supported by several rods: Four rods in the vertical plane and one additional rod in the horizontal plane kept the sphere in place with the restoring force for the rods being achieved via connected springs. The movement of the rods is measured via differential transformers, translating directly into a movement of

a metal core inside a coil. The vertical axis transducer signals are canceling (no vertical wind detection), while horizontal transducer signals are used for calibration. The authors claim that silicon-oil filled dash-pots provide additional damping for each rod, thus allowing for a maximal time resolution of up to 10 Hz. Reduced vortex shedding from the sphere was accomplished due to the porous polystyrene sphere, which was previously also observed for Reed III and Lynch's "Hole Ball Anemometer". Properties which also distinguish Kirwan et al.'s thrust anemometer from the previously described sensors are the limitation to an acceptance angle of $\pm 40°$ and a limited measurement range to below 14 m/s.

While all previously described anemometer prototypes are based on mechanically detecting sensors, Gunnlaugsson et al.'s "Telltale Wind Indicator" device of the "Phoenix" mission's Mars lander stands out by an optical measurement of a drag-based displacement. An ultra-light cylindrical pendulum body supported by thin Kevlar fibers is deflected by the wind in the Martian atmosphere. The magnitude and direction of the deflection is detected using a digital camera, which is observing both the pendulum and its mirror image [Gunnlaugsson et al., 2008]. However, this device not only stands out due to the used measurement technique, but also due to the unique field of application: The expected very low wind speeds ($u << 30$ m/s) in the much thinner Martian atmosphere (atmospheric pressure $p_{Mars} \approx 0.006\, p_{Earth}$) in combination with the restrictions on payload and power consumption during astrophysical missions. In this special field of application, the limited velocity range (2–10 m/s) and even the extremely poor temporal resolution of up to one sample per minute (1/60 Hz) can be accepted, while both are way below standards for meteorologic sensors in terrestrial sites.

Generally speaking, various different types of drag based sensors have been developed during the last couple of decades. The sensors not only varied widely in terms of used measuring techniques – partly owed to the constraints of the technological level of the epoch. There have also been quite different approaches regarding the form and the surface of the used drag bodies. Simple ping pong balls have been used as well as hole balls, (rough) cylinders and even porous spheres. None of the mentioned drag-based anemometers could be established either in oceanography, meteorology or atmospheric turbulence research. Since literature usually does not cover the reasons for this, one can only speculate or make some guesses about the reasons, amongst which one might find the long-term instabilities of strain gauges and maybe the issues regarding the drag body design itself. Since the most recent attempts to construct a sphere anemometer date back to the early 1990s, it may well be worth taking another shot at it, using today's advanced sensors and measuring techniques.

Chapter 3

The Sphere Anemometer Principle

The aforementioned drawbacks of conventional anemometers – e.g. fragility, low resolution or systematic biases – give rise to the idea of following a different approach for wind measurements. While previous drag-based anemometers using various types of sensors could not be established, the simplicity of the drag-based measurement is still intriguing and well worth approaching with todays measurement techniques. This chapter introduces the general principle of operation of the sphere anemometer developed in Oldenburg. An overview of the past and current setups of the sphere anemometer will be given including a comparison of the setups as developed by Schulte [2007] and Heißelmann [2008].

3.1 Principle of Operation

The sphere anemometer is a drag based wind speed sensor. The measuring principle exploits the drag force, which is acting on a body when it is exposed to whatsoever flow. In general, the drag force F_D acting on a body of cross-section A is proportional to the flow velocity u, where the exact relation is given by

$$F_D = \frac{1}{2} \cdot \varrho \cdot c_D \cdot A \cdot u^2.$$ (3.1)

ϱ denotes the fluid density and c_D is the non-dimensional drag coefficient, which depends on the shape of the body. Once a body of characteristic dimension D, e.g. sphere diameter, is attached on top of a flexible support rod of length l, the acting drag force F_D when the setup is exposed to the flow will cause the flexible support to bend by an amount of s_1' (Fig. 3.1). If the force acting on the support rod is taken into account as well, this will cause an additional displacement s_2' of the tip, and the total tip displacement is $s' = s_1' + s_2'$. If we assume that the drag force F_s of the sphere is acting in a single point at the tip of the support, while the drag force of the support F_t is acting as an areal force [Barth, 2004], the total tip displacement s' can then be calculated as

$$s' = \frac{l^3}{E \cdot J} \cdot \left(\frac{F_s}{3} + \frac{F_t}{8} \right).$$ (3.2)
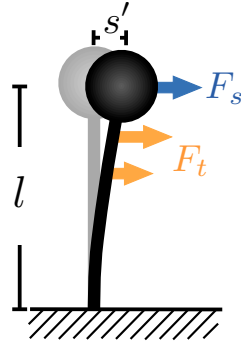
Figure 3.1: Displacement s' of a tube with sphere on top bending due to the drag forces F_s and F_t acting on sphere and tube, respectively.

The product of the material-dependent elasticity modulus E and the geometry-dependent second moment of the area J of the support constitutes the stiffness $E J$. The second moment of the area for the case of a support tube with inner radius R_i and outer radius R_o is given by

$$J = \frac{\pi}{4} \cdot (R_o^4 - R_i^4) \tag{3.3}$$

and thus the tip displacement is

$$s' = \frac{l^3}{E \cdot \frac{\pi}{4}(R_o^4 - R_i^4)} \cdot \left(\frac{F_s}{3} + \frac{F_t}{8} \right). \tag{3.4}$$

Consequently, the choice of a certain material and its dimensions can be used to adjust the tip displacement s' for a given (or required) velocity range by choosing proper values for E, J and l. Inserting the expression for the drag force from Equation (3.1), Equation (3.2) transforms to

$$s' = \frac{\varrho \cdot l^3}{2 \cdot E \cdot J} \cdot \left(\frac{A_s \cdot c_{Ds}}{3} + \frac{A_t \cdot c_{Dt}}{8} \right) \cdot u^2, \tag{3.5}$$

where the indices s and t denote the contributions from the sphere and the support tube, respectively.

Thus, the tip deflection s' is proportional to the drag coefficients c_{Ds} and c_{Dt} and the square of the flow velocity u^2

$$s' \propto (c_{Ds} + c_{Dt}) \cdot u^2. \tag{3.6}$$

The measurement of the tip displacement s' can be utilized for the calculation of the prevalent wind speed u once a calibration function of displacement s' versus wind speed u is known.

3.2   Drag Coefficients of Sphere and Cylinder

The relation of the wind speed u causing the anemometer's tip displacement s' given in Equation (3.6) includes the respective drag coefficients of the sphere and the tube,

c_{Ds} and c_{Dt}. In order to narrow the meaning of this equation down, one should have a closer look at the properties of the drag coefficient. A direct comparison of drag forces acting on objects is only reasonable, if the objects have the same size and properties while being exposed to the same flow situation. Practically, this is very hard to achieve and results of experiments or simulations are not immediately comparable. Considering the drag coefficient instead is a way out of this dilemma, since it is a non-dimensional representation of the drag force acting on a body in a certain flow situation. The characterization and comparison of flow situations by means of non-dimensional quantities is an oft-used concept in fluid dynamics. The most prominent non-dimensional quantity is the Reynolds number, but other non-dimensional characteristic numbers such as the Mach number Ma or the Strouhal number St may be used depending on the field of investigation.

The Reynolds number Re relates the turbulent production in the flow to the energy dissipation due to viscous forces and is given by

$$Re = \frac{\varrho \, u \, D}{\mu} = \frac{u \, D}{\nu}.$$

(3.7)

Here D is the characteristic dimension (or length scale) of the flow with mean velocity u. ϱ is the fluid density and μ and $\nu = \frac{\mu}{\varrho}$ are the dynamic and kinematic viscosity, respectively. The value of the Reynolds number is typically used to distinguish different flow regimes or to match similar flow conditions for various characteristic length scales D.

A similar approach for the definition of a non-dimensional drag coefficient c_D can be found by means of dimensional analysis yielding

$$c_D = \frac{2 \cdot F_D}{\varrho A u^2},$$

(3.8)

with drag force F_D, and cross-section A of the exposed object. This drag coefficient depends on the flow velocity and density and thus is a function of the Reynolds number Re.

Experiments conducted by Wieselsberger [1914] using smooth spheres of different size proved the scaling with Reynolds number, since the obtained results for the drag coefficients were in fair agreement when plotted against the Reynolds number. A subcritical flow regime could be identified, which is marked by a rather constant drag coefficient of about 0.45–0.5 for a smooth sphere. Towards higher Reynolds numbers, a sudden drop in the drag coefficient occurs until a minimal value is reached at the critical Reynolds number Re_c. This critical regime is followed by a supercritical regime in which the drag coefficient slowly recovers to a higher value before being rather constant again in the transcritical regime (Fig. 3.2). The Reynolds number at which the transition from one flow regime to another occurs cannot be strictly given, because boundary conditions like background turbulence level, blockage and surface roughness strongly affect the transition process [Achenbach, 1972]. Wieselsbergers experiments helped deduce the effect of turbulence on the drag coefficient and he
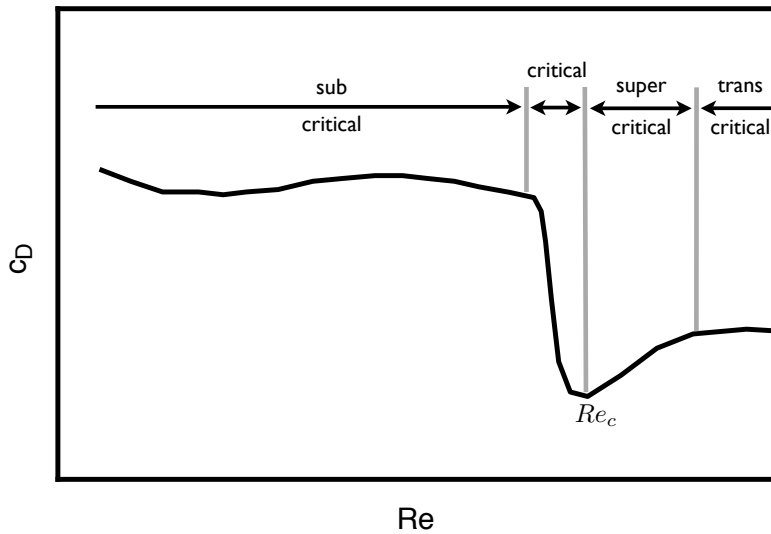
Figure 3.2: Definition of the flow regimes for the drag coefficient depending on Reynolds number according to Achenbach [1972]. The range of subcritical flow exhibits a rather constant drag coefficient of about 0.45–0.5, while a sudden drop in c_D happens in the critical regime. In the supercritical regime beyond the critical Reynolds number Re_c the drag coefficient rises again, before it saturates in the transcritical regime.

concluded, referring to Ludwig Prandtl, that the presence of background turbulence in the flow and the impact of surface roughness like dimples yields the same effect of premature drag reduction, shifting the critical region towards lower Reynolds numbers. It is apparent for smooth and rough spheres in laminar and turbulent flows either way but varies in strength and critical Reynolds number. Investigations by Achenbach [1972, 1974a] have been conducted for smooth and rough spheres, while Bearman and Harvey [1976] contributed results for what is called a "British golf ball". Achenbach [1974a] glued spherical glass particles of different diameter k on the surface of the test body to achieve different roughness parameters k/D – the ratio of pattern diameter k and sphere diameter D. He additionally used as sphere surface roughened with sand paper to deduce the effect of surface roughness on the drag coefficient. Achenbach observed a reduction of the critical Reynolds number Re_c with increasing roughness parameter k/D followed by a quick recovery to a value of $c_D \approx 0.4$. The amount of drag reduction in the critical regime was reduced for larger k/D, while the recovery was enhanced in these cases yielding a smaller region of reduced drag.

In contrast to Achenbach [1974a]'s findings, Bearman and Harvey [1976] and later Choi et al. [2006] used dimples to roughen the sphere surface instead of adding 'positive' roughness elements. For these golf ball type of spheres, a larger supercritical region of constantly reduced drag coefficient was observed beyond the critical regime in both experiments, giving rise to the conclusion that dimples serve as more efficient patterns for drag reduction. Bearman and Harvey and Choi et al. attribute this to an efficient tripping of the boundary layer at a fixed transition location, while the
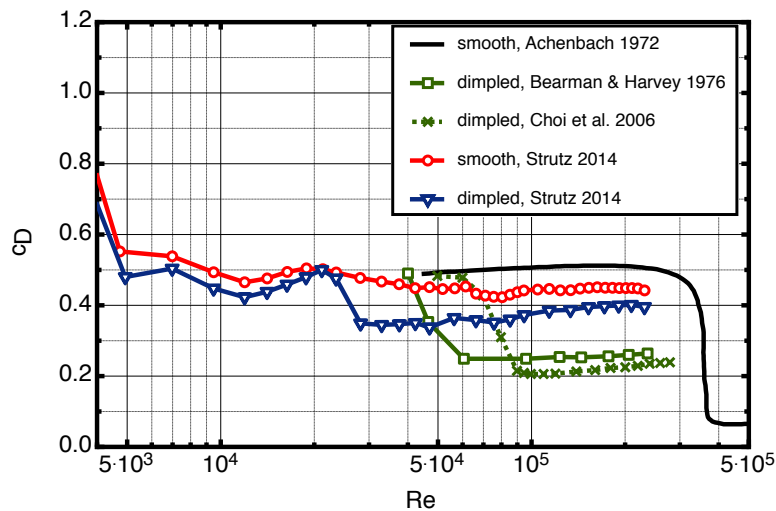
Figure 3.3: Drag coefficient c_D for spheres with different surface properties plotted against Reynolds number Re. The baseline case of a smooth sphere taken from Achenbach [1972] exhibits the drag crisis at $Re \approx 4.5 \cdot 10^5$ while the investigations by Bearman and Harvey [1976] and Choi et al. [2006] show a premature onset of the drag crisis for dimpled surface patterns. The same early drag crisis can be seen in the data from Strutz [2014] of an experiment using a smooth and a dimpled sphere of same dimensions.

added surface roughness elements used by Achenbach generate a thickened boundary layer, which still separates at fluctuating locations. After Bearman and Harvey suggested this mechanism in 1976, Choi et al. [2006] performed flow visualizations and explained the drag reduction by a dimpled surface pattern.

In general, the drag coefficient of an object like a sphere or a cylinder depends not only on the Reynolds number but also on properties of the objects surface. This becomes evident if one compares the drag coefficient of a smooth sphere exposed to laminar flow and turbulent flows. Figure 3.3 shows the drag coefficient of different smooth and dimpled spheres. However, the drag reduction is not per se a wanted feature for a sphere anemometer. Instead, it is aimed for a simple and analytic calibration function, and it is consequently desirable to operate the sphere anemometer in the range of almost constant drag coefficient. As Schlichting [2000] pointed out based on measurements by Wieselsberger, the drag coefficient of a circular cylinder with smooth surface also varies only little over a broad range of subcritical Reynolds numbers, $10,000 \leq Re \leq 200,000$. A similar case can thus be made for the impact of the drag coefficient of a cylinder on the calibration of a drag-based anemometer.

3.3 Measuring Method of the Sphere Deflection

The principle of measuring the resulting displacements of a mechanical system as described in Section 3.1 can be carried out in various ways, as was already indicated in Section 2.4. Up to now, the approaches to drag-based anemometry relied on the

use of mechanically deforming elements, like strain gauges [e.g. Norwood et al., 1966; Kirwan et al., 1975; Green et al., 1991] or inductive proximity sensors [Smith, 1980]. In contrast to these approaches, the sphere anemometer developed in Oldenburg aims to combine the principle of drag-based deflection with the benefits of the contact-less light pointer technique. This measurement technique was first employed in atomic force microscopes (AFM) by Martin et al. [1987] and has since been refined. It is used for the detection of minimal displacements of a cantilever beam at very high sampling rates well beyond $f_s = 10$ kHz.

In general, a light pointer is used as an optical amplifier of small mechanical deformations. As an example, consider a flexible beam which is supported on one side and free on the other side. A laser beam is aimed from the tip along the beam orientation on a screen or detector, as sketched in Figure 3.4. Once the beam is bending due to the applied forcing, the tip of the beam will be displaced by an amount s'. The position of the laser spot on the screen or detector is, however, displaced by a larger length s. Thus, the light pointer can be considered an optical amplifier, which translates very small mechanical displacements into a measurable displacement of the laser spot. The displacement s of the laser can be measured by means of a a two-
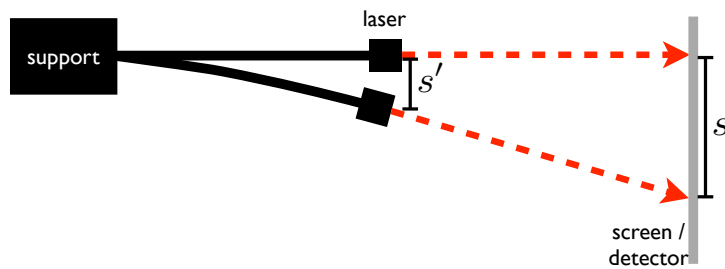
Figure 3.4: Optical amplification of a displacement s' by means of a light pointer aimed on a screen or detector. The larger displacement s on the detector can be measured with higher accuracy and resolution.

dimensional position sensitive detector (2D-PSD) either with the laser directly aimed on the detector or by capturing a reflection. Its incident spot induces photo currents I_n, $n \in 1 \dots 4$, at the corners of the detector and the magnitudes of the currents depend on the position of the center of gravity of the light spot. It can be calculated in Cartesian coordinates (x, y) according to the detector data sheet [Hamamatsu, 2007]

$$
\begin{aligned}
x &= \frac{(I_2 + I_3) - (I_1 + I_4)}{\sum_{n=1}^{4} I_n} \\
y &= \frac{(I_2 + I_4) - (I_1 + I_3)}{\sum_{n=1}^{4} I_n},
\end{aligned}
\tag{3.9}
$$

where I_n are defined as depicted in Figure 3.5. These non-dimensional coordinates have to be linked to wind speeds and directions via a calibration in order to measure the flow.
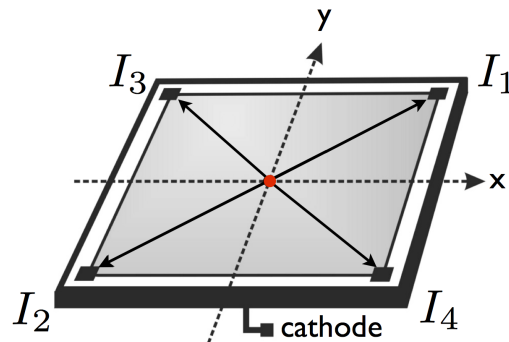
Figure 3.5: Sketch of the linear 2D position sensitive detector. The laser spot (red dot) incident at the center of the active area induces photo currents $I_1 \ldots I_4$, which are depending on the position of the spot and can be converted to (x, y)-coordinates.

The most common types of semiconductor position sensitive detectors are linear detectors and 4-quadrant detectors as depicted in Figure 3.6. While the linear detectors feature one single active surface, the quadrant detectors consist of four equally sized areas, which are separated by a small gap. Quadrant detectors provide high spatial resolution, but all four quadrants need to be hit by the incident laser spot in order to operate properly. This allows for the measurement of very small deflections, but at the same time demands a better quality (shape, intensity distribution) of the incident laser spot. Consequently, lasers and lenses have to be of higher quality, which increases the costs and size of the system. Therefore, the linear type of 2D-PSD was preferred for the sphere anemometer application described hereafter.
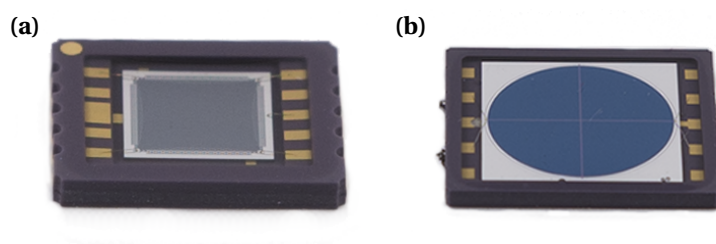
Figure 3.6: Photo of two different types of two-dimensional position sensitive detectors (2D-PSDs). (a) Hamamatsu linear PSD S5990-01 [Hamamatsu, 2007] and (b) Silicon Sensors 4-quadrant PSD QP100-6 [Silcon Sensors, Inc., 2010].

3.4 Previous Investigations in Oldenburg

The first implementations of a spherical drag force sensor at the University of Oldenburg started with two conceptual studies by Henning and Mehmet [2004] and by

Schulte [2007]. Both attempts can be considered proof-of-concept studies, which will be only briefly described before the first 2D sphere anemometer setup by Heißelmann [2008] will be introduced as the starting point of the developments presented in this thesis.

In 2004, Henning and Mehmet set up a first open, one-dimensional setup on a $50 \times 40\,\text{cm}^2$ grid board. It consisted of a ping-pong ball with about 40 mm diameter, which was attached to the tip of a thin metallic rod with squared cross-section. A mirror glued to the side of the rod, was used to reflect a laser beam onto an one-dimensional position detector. Their work was followed up by the realization of a first closed setup by Schulte [2007], who used a 12 cm long transparent acrylic glass[4] tube and mounted a polystyrene sphere with about 69 mm diameter on top of it. The final setup employed a polystyrene sphere with 49 more or less equally distributed dimples of 11 mm diameter. The bottom of the support tube with the sphere atop was fixed to a drill chuck on top of a rectangular aluminum box as displayed in Figure 3.7 (left). A Flexpoint® laser module with a size of $70 \times 11.7\,\text{mm}^2$ (length × diameter) was fitted through a hole in the anemometer box, and although the housing was not lightproof, this setup can be considered the first integrated sphere anemometer setup realized in Oldenburg. Inside the housing, the laser was aimed on a beam splitter, which redirected the beam onto a mirror attached to the top of the acrylic glass tube. The reflected beam passed the beam splitter again and hit the two-dimensional position sensitive detector (2D-PSD) at the bottom of the aluminum box as sketched in Figure 3.7 (right). Despite the use of a two-dimensional sensor, which generally permits 2D measurements, only 1D calibrations and experiments in main flow direction were performed and analyzed by Schulte [2007].

Using this setup, Heißelmann [2008] found, that it was suffering from some major problems jeopardizing the performance and reliability of the sphere anemometer. Minor issues were related to the mechanical stability and handling of the used beam splitter, which caused reflections on the 2D-PSD and required a higher laser intensity. To improve the handling and adjustment of the anemometer, an integrated setup was built without beam splitter. This was achieved using a laser diode atop the tube, which was directly focused on the 2D-PSD (Fig. 3.8, right). The most severe problems were related to the used acrylic glass tube, though. Like many thermoplastics, the used acrylic glass was prone to strong creeping when it was exposed to the drag force. Response times until reaching an equilibrium state of the tip deflection were in the order of ten minutes and more, depending on initial state of the deflection and the strength of the applied drag force. The tip displacement of the bending tube was also subject to severe hysteresis. In addition, another problem was found to be critical for the usability of the anemometer. The creeping of the tube material initially caused the two-dimensional calibration function of the anemometer to be smooth, yet it only masked the drag force variations for different inflow angles caused by the

---

[4]The historic name "acrylic glass" is used instead of the chemical name of the thermoplastic Polymethylmetacrylate (PMMA) to improve the readability.

coarse dimple structure of the sphere. These problems related to the tube and sphere were critical impediments making the setup inapplicable for any reliable measurement and lead to the substitution of the acrylic glass tube with one made of glass-fiber reinforced plastics (GFP).

In the assessment of this re-designed setup, the coarse surface pattern of the polystyrene sphere was found to cause an asymmetric and ambiguous two-dimensional calibration function, which exhibits significant scattering between consecutive inflow angles [Heißelmann et al., 2008]. This effect was reduced for a calibration recorded with a smooth polystyrene sphere, although still deviations could be seen for certain angles. Since the setups were similar in all other features, the scattering of the calibration has been attributed to the dimple structure.

An additional radiation experiment carried out in order to investigate the sphere anemometer behavior in direct exposure to sun light revealed, that the dome-shaped housing made of 10 mm thick plastics was not completely impermeable to light and thus the diffuse light inside the housing caused the 2D-PSD to overload. An attempt to avoid this by coating the housing with several layers of paint failed since it only reduced the effect, but could not completely avoid it. However, the impermeability to ambient light is of relevance for the development of a sensor, which is exposed to constantly varying light conditions in the atmosphere. Therefore, any spoiling influence on the optical measuring technique needs to be ruled out and a re-design of the anemometer housing is required.
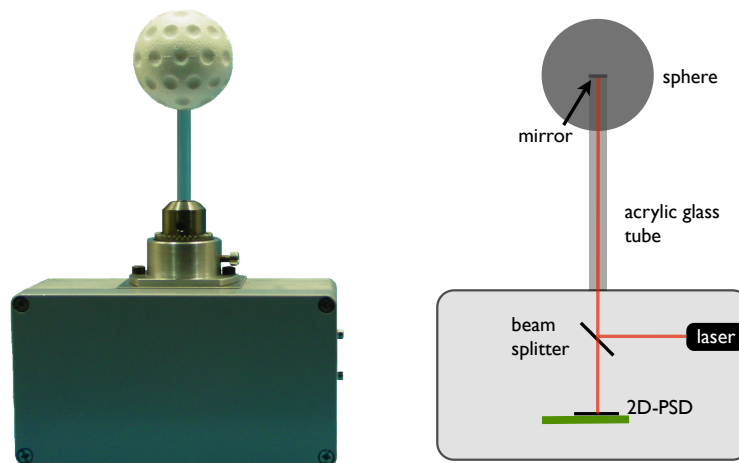
Figure 3.7: Photo and schematic setup of the first integrated sphere anemometer realized by Schulte [2007]. The coarsely dimpled polystyrene sphere atop an acrylic glass tube was mounted to the aluminum box containing the laser module, beam splitter and position detection circuit board.
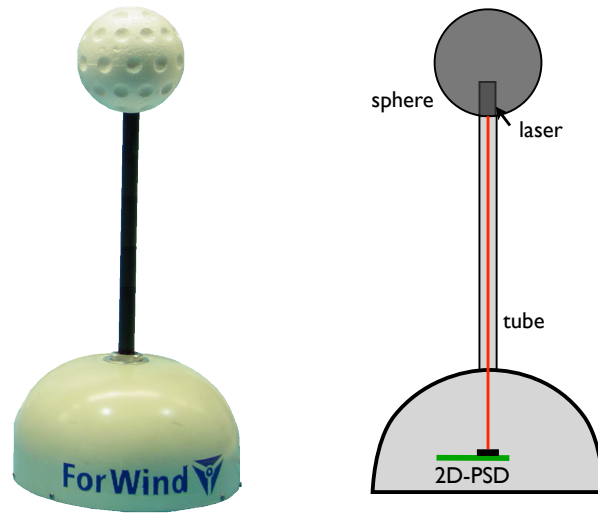
Figure 3.8: Photo and sketch of the modified sphere anemometer setup with directly aimed laser diode atop the tube by Heißelmann [2008].

3.5   Summary & Discussion

The general principle of a sphere anemometer based on the drag-dependent deflection of a flexible tube has been presented in this chapter as well as the drag coefficient in general and its dependence on the surface roughness. With the light pointer principle, a highly resolving optical measuring technique for the deflection detection has been introduced. Investigations on the first realizations of this principle at the University of Oldenburg were briefly summarized. The comparison of the 2D calibrations for a sphere anemometer with coarsely dimpled and smooth sphere revealed severe clustering and ambiguities of the calibrations for the dimpled case. While the tube material has already been changed from acrylic glass in previous setups to glass-fiber reinforced plastics in order to enhance the reproducibility of the calibrations, the coarse sphere surface of the setup needs to be addressed as well as the issue of the light permeability of the housing. Both issues lead to the conclusion, that changes of the setup of Heißelmann [2008] are inevitable to make the sphere anemometer applicable for outdoor measurements.

Chapter 4

Anemometer Design Criteria

The sphere anemometer based on the principle described in Chapter 3 has several parameters, which can be adjusted to match specific design criteria such as its operational range or spatial and temporal resolution. These criteria cannot be fulfilled by tuning isolated setup parameters, but are usually affected by a combination of several parameters. An overview of the most relevant anemometer properties and the determining parameters will be given in this chapter.

4.1 Wind Speed Range of Operation

The range of operation, i.e. the measurable minimum and maximum wind speeds, and the survival wind speed are important features of any anemometer, since it determines the suitability for a measurement application. The survival wind speed is simply given by the strength of the used materials and connections. Although wind speeds up to 50 m/s were successfully tested in the wind tunnel, a detailed treatment of the survival wind speed is not part of this work. Higher survival wind speeds can be expected, though, due to the absence of mechanically vulnerable parts of the anemometer, such as bearings or precisely aligned transducers.

The range of operation for the sphere anemometer is determined by the minimum resolvable displacement of the laser spot on the detector surface s_{min}– giving the minimum wind speed – and by the maximal displacement s_{max} of the laser spot before partially leaving the active area of the 2D-PSD. Both values can be obtained from the data sheet of the detector. While the minimal detector resolution of 7 μm is no practical limitation to the lower wind speed bound, the maximal detectable displacement for the used Hamamatsu 2D-PSD of 2.25 mm from the center needs to be considered for the upper bound of measurable wind speeds [Hamamatsu, 2007]. The wind speeds u_{min} and u_{max} corresponding to these two laser spot displacements are given by the respective tip displacements s'_{min} and s'_{max} of the sphere according to Equation (3.2). Considering this, the displacement s of the laser spot can be obtained from the distance L of laser and detector and the tilt angle of laser diode by simple geometrical considerations. Note that L is the sum of the tube length l from the tube

fixation to the position of the laser diode and the height l' of the anemometer housing from the 2D-PSD to the tube fixation, $L = l + l'$.

The tip displacement s', and consequently the spot displacement s, are functions of the tube's elasticity E and the geometry of sphere and tube. This dependence allows for a fine tuning of the range of operation by variation of the tube material and most notably the dimensions, i.e. tube length l, inner and outer radii R_i and R_o and sphere diameter D. This approach is very useful for the design process, since it enables the selection of tubes with desired properties and also allows for an estimation of the required geometric parameters of the tube, sphere and housing. Moreover, adjustment of the sphere anemometer design can be based on this consideration in order to adapt the setup to different applications, e.g. measurements in low wind speeds or exceptionally high wind speed environments such as Typhoons. This approach comprises some uncertainties, mainly in the estimation of the drag forces F_s and F_t. Section 4.2 addresses these uncertainties and gives a brief overview of the impact of the drag coefficient on the anemometer properties.

4.2 Calibration Function

The drag forces acting on the sphere and the tube are the base of the sphere anemometer approach to wind speed and direction measurements. The properties of the anemometer, in particular the calibration function, are therefore influenced by the aerodynamic characteristics of the two bluff bodies. The drag forces F_s and F_t depend on the physical dimensions of the sphere and tube, respectively, and also on the squared wind speed u. The drag coefficients of the respective body may also vary for different wind speeds and dimension, i.e. for different Reynolds numbers Re, as was introduced in Section 3.2. These parameters are included in the design of the setup, but may pose some challenges as well. While effects like the varying drag coefficients c_{D_s} and c_{D_t} due to the surface structure of sphere and tube may be utilized during the design process, they are much harder to control due to the uncertainty of the drag reduction mechanism (Sec. 3.2). This is also a limiting factor to the precision of the adjustments presented in Section 4.1 and in turn means, that the design based on the mentioned material and geometry parameters can only be an estimation.

The sphere diameter is selected in order to yield sufficiently large drag forces to ensure measurable tip deflections for a wide range of wind speeds. Both, the sphere and tube diameters are kept constant for all anemometer setups. Emphasis lays on a simple and analytic calibration function as a design criterion, and it is consequently desirable to operate the sphere anemometer in the range of almost constant drag coefficients c_{D_s} and c_{D_t}. In this case, the relation for the tip deflection s' from Equation (3.6) transforms to the simpler

$$s' \propto u^2, \tag{4.1}$$

resulting in a square root calibration function for the laser spot displacement s

$$u = m \cdot s^{0.5} \tag{4.2}$$

with slope m. m decreases for spheres with larger drag coefficients c_{D_s} while it increases for reduced c_{D_s}. Although the slope accounts for different drag coefficients, i.e. different sphere surface properties, this idealized form of the calibration function still relies on the condition of a constant c_D. The subcritical Reynolds number range of approximately 10,000 to 350,000 for a smooth sphere exhibits an almost constant drag coefficient. Schlichting [2000] showed similar behavior for the drag coefficient of a circular cylinder with smooth surface over a broad range of subcritical Reynolds numbers of $10,000 \leq Re \leq 200,000$. However, some variations of c_D can be seen in the double-logarithmic plot in Figure 3.3 for the data from Achenbach [1972] or Strutz [2014]. These will result in deviations of the sphere anemometer calibration function from the idealized shape. It can be phrased slightly more general to handle the inevitable variations of c_D with the Reynolds number. Two additional parameters s_0 and n are therefor included in a power law for the calibration function

$$u = m \cdot (s - s_0)^n \tag{4.3}$$

to allow for better fitting to actual measurement data. The difference of n from the case of $n = 0.5$ can be used as a measure for the deviation of the calibration function from its ideal square-root shape and s_0 accounts for possible offset displacements of the laser spot on the 2D-PSD.

While even smooth spheres exhibit variations of the drag coefficient with Reynolds number, dimpled surface patterns pose a challenge of its own due to the premature occurrence of the drag crisis. However, when the roughness parameter k/D is carefully chosen, spheres with dimpled patterns, may also exhibit a wide range of relatively constant drag coefficient as can be seen in the measurements by Strutz [2014] (Fig. 3.3, blue). The drag reduction by means of dimpled surface patterns is not per se a wanted feature for a sphere anemometer as a drag-based sensor, but effects like reduced vortex shedding from the sphere may be beneficial due to reduced oscillations of the sphere-tube combination. Possibly larger variations of c_D might cause further deviations from the idealized shape of the calibration function, but will by no means harm the uniqueness of the calibration. Consequently, smooth and dimpled spheres can be considered for the sphere anemometer without jeopardizing its functionality.

4.3   Spatial and Temporal Resolution

Another design criterion of an anemometer is the provided resolution, which may be divided in temporal and spatial resolution, although both are linked via Taylor's hypothesis of frozen turbulence [Taylor, 1938].

The spatial resolution of an anemometer is either given by its dimensions or, as in the case of cup anemometers, by the characteristic length scale until its rotation

reached an equilibrium state. Regarding the sphere anemometer, the two main parameters to adjust the spatial resolution are the sphere diameter D and the size of the tube l. Considering a turbulent fluid column passing the sensor with a certain mean wind speed $\overline{u}$, it is easy to understand, that no turbulent structures smaller than these dimensions will be resolved, since the sensor integrates them.

The temporal resolution marks one of the key features of any sensor. While electronic properties of the entire measuring system, such as sampling rate of analog-digital (AD) converters and response times of electronic amplifiers, may be limiting the temporal resolution of very fast sensors, the critical property of a mechanical sensor like the sphere anemometer is the natural frequency of the system. Any excitation of the anemometer by mechanical oscillations, e.g. from the anemometer boom or other support structures, causes the anemometer to oscillate with its natural frequency f_0. Furthermore, these oscillations can also be wind induced vibrations, which are caused by vortex shedding from the sphere and the supporting tube. The vortex shedding from these structures results in a Kármán[5] vortex street and the frequency of the shedding vortices depends on the wind speed. The relation of both, the wind speed u and vortex shedding frequency f_u, is given by the non-dimensional Strouhal[6] number

$$St = \frac{f_u \cdot D}{u}, \qquad (4.4)$$

where D denotes the characteristic dimension of the object – in this case the sphere diameter [Tritton, 1988]. The Strouhal number cannot generally be considered constant for the flow around a sphere, and for low Reynolds numbers even two co-existing values for the Strouhal number are found [Sakamoto and Haniu, 1990]. However, Achenbach [1974b] showed, that a rather constant value of $St = 0.19 \sim 0.195$ can be assumed for a smooth sphere in the treated Reynolds number range of $Re = 2 \cdot 10^4 \dots 3.7 \cdot 10^5$. The vortex shedding frequency f_u thus varies with the flow velocity u in this range and can be calculated according to Equation (4.4).

Each shedding vortex transports some energy and thus excites the mechanical oscillation of the structure with the frequency f_u. Attempts to reduce the energy content of the shed vortices include the use of patterned sphere surfaces, which is challenging for various reasons as pointed out in Section 4.2.
Once the vortex shedding frequency f_u is close to the natural frequency f_0 of the system, resonance effects may occur. Excitation frequencies close to the natural frequency of a system can lock-in and amplify the oscillation of the structure even to the point of breakage [7]. In order to avoid or at least reduce the lock-in related amplification of oscillations, it is important to estimate the natural frequency of the anemometer and possibly adapt it to the desired range of operation. Several parameters can be used to tune the natural frequency accordingly, like the elasticity modulus E, the

---

[5]Theodore von Kármán, 1881–1963

[6]Vincenc Strouhal, 1850–1922

[7]A prominent examples of these resonance phenomena is the collapse of the Tacoma Narrows bridge in 1940 due to wind induced vibrations locking in with one natural oscillation mode of the structure.

second moment of the area J, the length of the tube material l and also the mass M of the sphere and laser diode on top of it. Moreover, measures can be taken to reduce vortex shedding, e.g. shifting the range of vortex shedding frequencies f_u in order to separate it from the natural frequency f_0.

A first analytic approach based on the work by Rubin [2004] was used to estimate the natural frequency of a bending beam with constant mass distribution $\varrho_m S$, where ϱ_m is the density of the material and $S = \pi \cdot (R_o^2 - R_i^2)$ is the area of the tube's cross-section. Disregarding the tip mass M of the sphere and the laser diode in this analytical approach results in an over-estimation of the theoretical natural frequency compared to the real natural frequency of the sphere anemometer, though [Heißelmann, 2008]. In a more accurate estimation of the natural frequency for a setup with tip mass M, the eigenvalue κ is obtained by numerically solving the characteristic equation

$$1 + cos(\kappa\, l)\, cosh(\kappa\, l) + \frac{M}{M_t} \kappa\, l\, (cos(\kappa\, l)\, sinh(\kappa\, l) - sin(\kappa\, l)\, cosh(\kappa\, l)) \;=\; 0 \quad (4.5)$$

proposed by Wandinger [2007, Sec. 3.2.4]. In this equation, M_t is the mass of the tube with length l and $\kappa^4 = \omega^2 \frac{\varrho_m S}{EJ}$ is the first eigenvalue of the characteristic equation. The natural frequency $f_0 = \omega/2\pi$ can than be calculated from

$$\omega = \sqrt{\kappa^4 \frac{EJ}{\varrho_m S}}$$

$$\Rightarrow f_0 = \frac{1}{2\pi} \sqrt{\kappa^4 \frac{EJ}{\varrho_m S}} \qquad (4.6)$$

for a given combination of geometry and material parameters. Since larger tip masses M result in lower natural frequencies f_0, the mass of sphere and laser should be kept as small as possible to achieve a high temporal resolution of the sphere anemometer. However, the tip mass is not the only determining parameter, and while it can be adjusted without affecting the other design criteria of the anemometer, other parameters like tube length and material have to be also considered in the context of all desired sphere anemometer properties.

4.4   Summary & Discussion

A wide set of parameters can be used to adapt the sphere anemometer to meet desired design criteria, particularly the operational wind speed range and temporal resolution. As has been pointed out in this chapter, the sphere and tube parameters which impact these anemometer properties cannot be tuned independently. Figure 4.1 gives an overview of the most relevant parameters and their contribution to the design criteria. Considering the mutual dependency of the tip deflection s' and the natural frequency f_0 on the sphere and tube geometry, it is immediately evident that some trade-offs have to be made in the design process of the sphere anemometer.
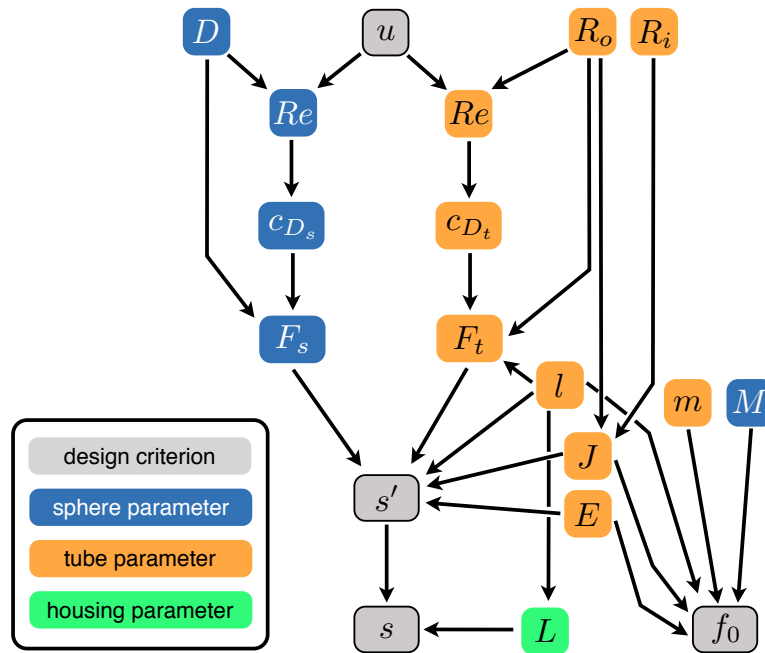
Figure 4.1: Entanglement of the sphere (blue) and tube (orange) parameters and their link to key sphere anemometer properties, such as wind speed u, laser displacement s and natural frequency f_0.

The above consideration constitute the basis for the design of the sphere anemometer setups presented in the following Chapters 5–7. All of these setups are designed to operate in a wind speed range of about $0.3\,\text{m/s}$ to $45\,\text{m/s}$ and the sphere diameter $D = 70$ mm and outer tube radius $R_o = 4$ mm are not varied for the different anemometers. Consequently, the tube length l and inner radius R_i are the main parameters used to adjust the expected laser spot displacement s for a selected tube material. Given the size of the active area of the 2D-PSD, the maximal acceptable laser displacement $s_{\max} = 1.85$ mm was fixed and the tube length was chosen accordingly. Calculations of the anemometer's natural frequency have been considered in order to rule out combinations of tube material and geometry leading to lower values than $f_0 \approx 20$ Hz, to ensure competitiveness to sonic anemometry. During the design process no emphasis was given to the expected theoretical accuracy and its variation for different wind speeds due ot the proportionality $s \propto u^2$, which it has already been treated by Heißelmann [2008]. An experimental assessment of the measurement precision and accuracy is performed for the final stage of the anemometer development presented in Section 7.3.

Chapter 5

The First Generation Sphere Anemometer

This chapter describes the sphere anemometer hardware setup based on the measuring principle introduced in Chapter 3. Persisting issues of the earlier realizations are accounted for in this 1st generation sphere anemometer by modifications made to key components. The design criteria and methodology of Chapter 4 have therefor been employed. These crucial sensor characteristics are analyzed experimentally, as the one- and two-dimensional calibration functions are treated as well as the impact of different sphere surface patterns on it. The natural frequencies are also investigated as a limitation to the temporal resolution.

5.1 Sphere Anemometer Setup

The 1st generation sphere anemometer setup is based on the principle of a drag-force anemometer as described in Section 3.1 and realized by Heißelmann [2008]. Its housing consists of a dome-shaped cover mounted to a robust base plate. As a consequence of the radiation experiment mentioned in Section 3.4 both the cover and the base plate are made from milled aluminum in order to avoid permeability to light and torsion of the housing. The aluminum cover is split off-center in two parts and can be opened to access the sensor parts by removing the smaller piece of the cover. A threaded aluminum ring fitted to the center of the dome cover allows for the fast and easy substitution of the mounted sphere-tube combination, which has the counterpart fixed to the lower end of the tube as sketched in Figure 5.1.

The tube made of glass fiber reinforced plastics (GFP, "fiber glass") consists of several layers of glass fibers with different orientations, which are embedded in a matrix of resin or polyamide. No exact fiber orientation is known for the used tubes, since no information on the production process was available from the retailer. A strain test resulted in an estimate of the tube's elasticity modulus $E \approx 36$ GPa[8]. The information

---

[8]The strain experiment was operated by Roland Kruse of the Acoustics Research Group, University of Oldenburg, using the *Gabo Eplexor 500 N*.
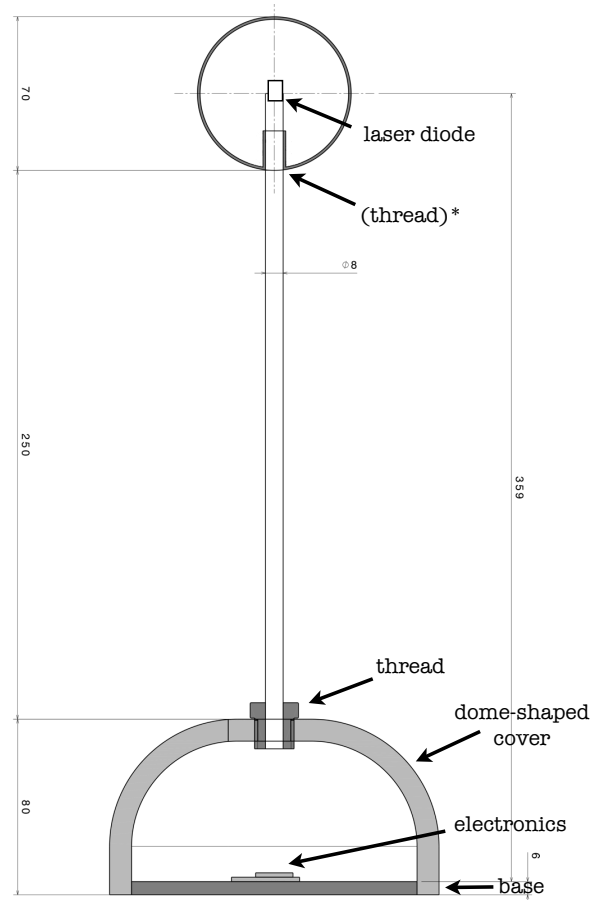
*Not used for regularly dimpled sphere.

Figure 5.1: Drawing of the 1st generation sphere anemometer setup. A sphere is mounted on top of a GFP tube, which is fixed to the dome-shaped aluminum housing be means of a thread. The laser diode atop is directly focused on the 2D-PSD and sensor electronics located at the bottom inside the housing.

about the elasticity modulus is utilized during the design process for the calculation of the expected tip deflections s' and thus the required tube length l as described in Section 4.1. It is also be used for the estimation of the approximate natural frequency of the anemometer as described in Section 4.3. Both calculations cannot be exact due to uncertainties in the manufacturing processes of the materials and the assembly of the anemometer, so no exact match of calculated and practically determined quantities can be expected. Thus, an uncertainty of some GPa in the measurement of E is not considered critical for the design process. The used GFP tube with inner radius $R_i = 3.5 \pm 0.05$ mm and outer radius $R_o = 4.0 \pm 0.05$ mm is cut to a length $l = 285 \pm 0.5$ mm between the top of the aluminum thread and the top of the tube. Its upper end is milled to slightly increase the inner radius on a length of approximately 5 mm in order to ensure a rigid fitting of the laser diode's lens mount, as this was found to be a weakness during the anemometer assembly. The sphere is glued
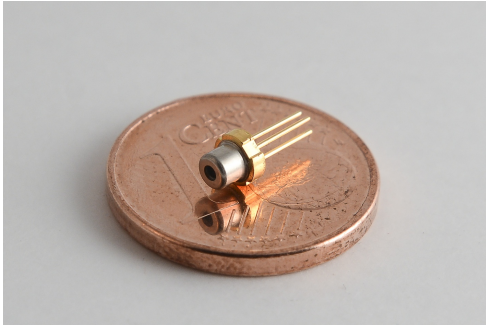
Figure 5.2: 5 mW laser diode in 3.3mm packaging with integrated laser driver. A 1 cent coin is depicted for comparison.

Figure 5.3: Photo of the CAW100 collimator lens inside the custom made lens holder (silver) and custom made laser diode mount (black) with precision thread to adjust the focus.

to the tip of the tube with its lower edge being in a distance of 40 mm from the top of the tube and consequently the lens of the laser is located in the center of the sphere once the anemometer is assembled. A drawing of the sphere anemometer setup with all relevant components is depicted in Figure 5.1.

The tip displacement is measured exploiting the light pointer principle described in Section 3.1. A laser beam is therefor aimed on the $4.5 \times 4.5 \, \text{mm}^2$ large sensitive area of a two-dimensional position sensitive detector (2D-PSD) S5990-01 by Hamamatsu [2007]. The laser spot induces four photo currents in the semiconductor sensor, which depend on the position of the incident laser spot on the active area of the detector. The induced photo currents can be converted to Cartesian coordinates of the spot location according to Equation (3.9).

Instead of using the bulky Flexpoint® laser module used in the setup of Schulte, a low-cost laser diode is used in the sphere anemometer. The main benefit of the used laser diode is its very lightweight construction with a small packaging of $d_l = 3.3 \, \text{mm}$ diameter and only $l_l = 8 \, \text{mm}$ overall length (Fig. 5.2). The laser diode of type ADL-65055SA2 by *Arima Lasers* has a typical wavelength $\lambda = 655 \, \text{nm}$ and provides a rated power of $P_0 = 5 \, \text{mW}$. The laser power is regulated by an external resistor R_{VR}, which is directly soldered to the diode's ground and VR pins. A laser driver is integrated in order to ensure the power of the laser to be constant even with slightly varying supply voltage [Laser Components, 2007]. The laser diode is fixed to a custom made holding piece with a precision thread on its outside as seen in Figure 5.3. It allows for the precise positioning of the lens mount holding the aspheric collimating lens CAW100 with a diameter $d_{\text{lens}} = 5.2 \, \text{mm}$ [Laser Components, 2008], such that the laser beam is focused on the active area of the 2D-PSD. The total weight of the laser diode including lens and mount is 2.2 g.

The incident light on the position sensitive detector causes a photo current as described in Section 3.3. In order to comply with the voltage input channels of most AD converters used, the induced current signals of the 2D-PSD are converted to voltage

signals and amplified before further data handling using a trans-impedance circuit as depicted in Appendix B. Taking the amplification into account, a metallic resistor of R_{VR} =180 kΩ (± 1%) is used to adjust the laser power to be about 250 μW in order to achieve a maximal signal output of 5 V for spot positions close to the 2D-PSD's corners. The specifications and dimensions of laser diode and lens mount are summarized in Tables 5.1 and 5.2.

Table 5.1: Specifications of the ADL-65055SA2 laser diode. The output power P_{set} was adjusted with the variable resistance R_{VR} for a supply voltage V_{S}.

λ	V_{S}	P_{set}	R_{VR}	M_l	dimensions ($d_l \times l_l$)
655 nm	5 V	250 μW	180 kΩ±1%	0.1 g	3×8 mm^2

Table 5.2: Specifications of the used lens and lens mount.

lens	d_{lens}	M_m	dimensions ($d_m \times l_m$)
CAW100	5.2 mm	2.1 g	8×17 mm^2

The trans-impedance amplifier is supplied with ±6 V DC from a voltage regulation circuit powered by two 9 V block batteries while the laser diode is supplied with 5 V DC provided by the USB port of the used measurement computer. Both supply voltages could also be obtained from a standard laboratory power supply, but the simpler battery and USB connection is preferred, since it is less prone to electronic noise and permits more mobility. The supply cables for the laser diode are attached at the outside of the tube. Two-wired ribbon cables with cross-section ∅ = 0.9 ± 0.05 mm are chosen over the previously used speaker cables (∅ = 1.25 ± 0.05 mm). The cables are only fixed at the top and bottom of the tube and are covered by a shrinking hose. This has similarly been employed in the previous anemometer setup for the benefit of reducing the induced oscillations of the sphere-tube-combination.

As a consequence of the highly scattered calibration function obtained for the previous anemometer setup with coarsely dimpled polystyrene sphere [Heißelmann et al., 2008], a re-design of the sphere was considered essential for the sphere anemometer improvement. While the diameter of the sphere is fixed at D = 70 mm, a different surface with reduced dimple diameter and depth is designed. Instead of the previously hand-made polystyrene spheres, the more accurate rapid prototyping method is used to produce a hollow sphere made of ABS plastics.
This sphere is patterned with 306 regularly ordered dimples of d = 4.9 ± 0.1 mm diameter and depth k = 1.3 ± 0.1 mm, resulting in a roughness parameter of k/D = 0.0186. The alignment of the dimples along lateral circles is chosen to be equidistant in circumferential direction as shown in the top view of the sphere in Figure 5.4 (a). A single dimple is located right at the top pole of the sphere and circles of equally spaced

(a) (b)
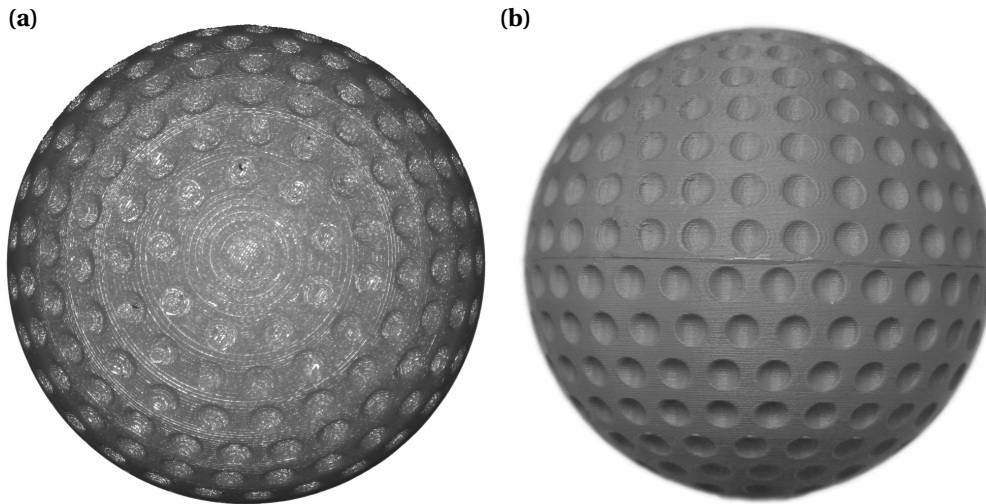
Figure 5.4: (a) Top view and (b) side view of the sphere with 306 regularly aligned dimples on its surface. The dimples are located along lateral circles with uniform distance in circumferential direction.

dimples align below for larger radii. The sphere consists of two hemispheres which are later bonded to one sphere along its equator (Fig 5.4, b). While the top half of the sphere is patterned with dimples as seen in Figure 5.4 (a), the bottom half has an 8 mm diameter hole with tubular joint at its pole for the fixation of the support tube. Besides this difference, the hemispheres are similarly patterned.

The weight of the complete sphere is $M_s = 38$ g, which results in a total tip mass $M \approx 40.2$ g for this sphere anemometer setup. Once it is attached to the tip of the tube, it is not possible to unmount or change the sphere non-destructively.

5.2 Sensor Calibration

The sphere anemometer as a drag-based measuring device is not based on first principles and thus needs to be calibrated with a flow of known velocity in order to enable the wind speed and direction measurements. All calibration functions of the sphere anemometer and the reference sensors discussed during the course of this work are measured in the acoustic wind tunnel of the University of Oldenburg, which is described in brief before introducing the actual sphere anemometer calibration. The characterization methodology of the sphere anemometer calibration introduced for the 1st generation setup will be carried forward for both later anemometer stages described in Chapters 6 & 7.

5.2.1 Acoustic Wind Tunnel in Oldenburg

The acoustic wind tunnel of the University of Oldenburg is a return-type facility (Göttingen type) with an outlet cross-section of $1 \times 0.8 \, \mathrm{m}^2$. The 88 kW motor generates wind speeds up to 50 m/s at a background turbulence level of about 0.3 %. The wind

tunnel can be operated either with a closed test section of 2.6 m length or as an open jet with 1.8 m length as depicted in Figure 5.5. The air flow temperature can be kept constant by means of a heat exchanger downstream the motor, and an additional water-cooler system for the motor can be used in high velocity operation. The contraction cone of the wind tunnel is equipped with eight connected Pitot tubes for the detection of the total pressure p_t and eight connected pressure holes in the nozzle are used for the detection of the static pressure p_s.

The calibration measurements presented within this work are performed using the open jet configuration as depicted in the sketch in Figure 5.5.
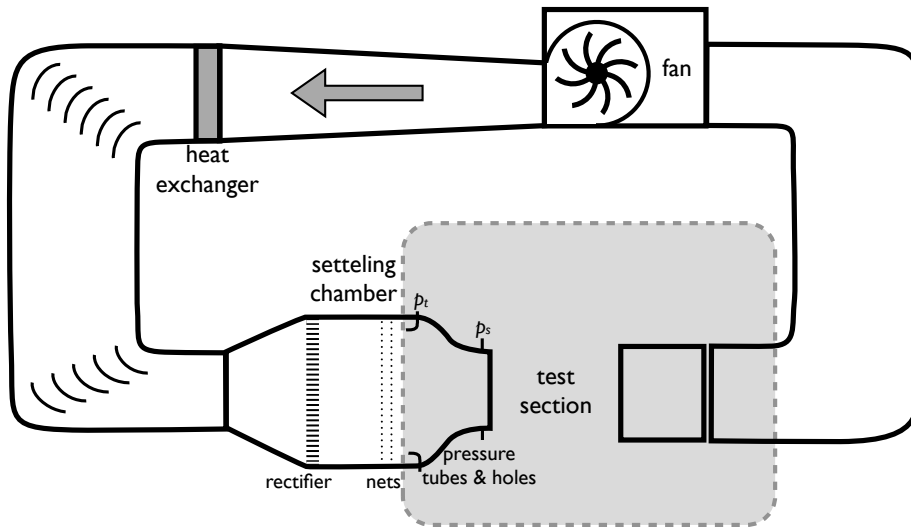
Figure 5.5: Sketch of the closed-loop acoustic wind tunnel of the University of Oldenburg with open configuration (side view, not to scale). The anemometers were calibrated and characterized in the open test section in measurement chamber (gray dashed). Wind speed readings can be obtained from the differential pressure $p_d = p_t - p_s$.

Calibration functions, which are used for qualitative comparison and development purpose only, rely on the wind tunnel speed display as reference. The reference wind speeds for the comparison with other anemometers presented in later chapters are measured with the built-in Pitot tubes and pressure holes (Fig. 5.5) in combination with an analogue Betz type 2500 micro-manometer providing a range of 2500 Pa at 0.1 Pa resolution [acin instrumenten bv, 2013] or a Setra C239 pressure transducer [Setra Systems Inc., 2013].

5.2.2 Setup for 1D & 2D Calibration

The sphere anemometer is placed on top of a motor-driven turntable in the wind tunnel to perform the anemometer calibration. The table top at a height of 1.15 m ensures, that the sphere-tube element is located in the central region of the nozzle. The anemometer is positioned in the center of the turntable at a downstream distance of 35 cm from the wind tunnel outlet to the center of the sphere anemometer. The x-axis

of the 2D-PSD's coordinate system is aligned parallel to the main flow direction (at 0°
inflow direction) and the y-axis was oriented cross-flow.

The first qualitative tests rely on the reference wind speed u, read from the wind tun-
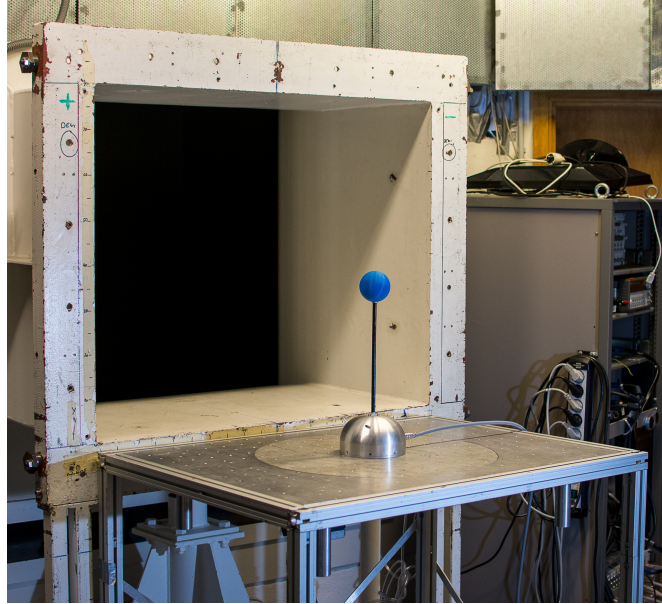
Figure 5.6: Photo of the 1st generation sphere anemometer mounted on the turntable in the
wind tunnel for the two-dimensional calibration.

nel control panel. This is sufficient for the evaluation of the principle shape and re-
producibility of the anemometer's calibration function since the ambient conditions
can be considered constant during the respective experiments.

The sphere anemometer is connected to its supply box. The power supply for the
laser is provided from the measuring PC via USB and the trans-impedance ampli-
fier of the 2D-PSD was supplied with ±6 V from a battery powered voltage regulator
circuit. The four output signals $U_1 \ldots U_4$ are connected with coaxial cables to a 16 Bit
AD-converter DT9816-A from Data Translation in the single ended mode [Data Trans-
lation, Inc., 2013] and simultaneously acquired with a sampling rate of $f_s = 1\,\text{kHz}$. It
is operated in the measurement range $\pm 5\text{V}$ resulting in a resolution of $\delta U \approx 0.153\,\text{mV}$.
The entire equipment including the sphere anemometer is granted a warm-up time
of at least 30 minutes prior to the first measurement in order to eliminate electronic
signal drift. The data acquisition is controlled by a customized LabVIEW program.
While the anemometer position is fixed for the measurement of a one-dimensional
calibration function, it is rotated along its vertical axis on the turntable to obtain a
two-dimensional calibration function. For this case a stepper motor is used for the
turntable rotation and controlled by the measuring PC with LabVIEW software via se-
rial connection. The two-dimensional calibration procedure is basically carried out
in a loop of three steps:

1. Set reference wind speed

2. Rotate anemometer counter-clockwise along its vertical axis to next inflow angle.

3. Acquire 2D-PSD signals for each set inflow angle

The convergence of the mean values is tested in order to ensure the validity of the calibration data. In this test specified in Appendix A, the average of the 2D-PSD signal is calculated for different windows of increasing time intervals up to ten seconds. An averaging time of about one second is found to be sufficiently long to reach the correct mean value of the laser position signal within ±0.5%. Consequently, the acquisition of the signals for ten seconds at $f_s = 1$ kHz sampling for each wind speed and inflow angle can be considered absolutely reliable and the settings are therefore used for all 1D and 2D calibration functions presented in this thesis.

5.2.3   1D Calibration Function

A one-dimensional calibration function for the 1st generation sphere anemometer with regularly dimpled sphere is measured in a range of reference wind speeds between 0 and 20 m/s. The raw voltage signals are acquired at each reference wind speed u and the (x, y)-coordinates of the laser spot on the 2D-PSD are computed according to Equation (3.9). The x- and y-offset signals, i.e. the mean of the resulting signals for $u = 0$ m/s, are subtracted from all x- and y-signals to obtain the 1D calibration of the anemometer.

The reference wind speed u plotted against the calculated x- and y-components of the voltage signals is displayed in Figure 5.7 for an inflow angle of $\Phi = 0°$. Although the values for the displacement s are mirrored due to the alignment of the 2D-PSD's coordinate system, it can be clearly seen that the shape of the x-component of the signal follows the expected power law function of Equation (4.3). Due to the alignment of the main flow direction with the x-axis of the 2D-PSD, y exhibits only minimal variations, which stem from a slight misalignment of the detector. The right plot in Figure 5.7 (b) displays the squared wind speed u^2 plotted against the sphere anemometer signal, fitted by a linear function. The coefficient of determination $R^2 = 0.9997$ of the linear fit to the data gives evidence of the well-matching proportionality $u^2 \propto s$. Although both plots in Figure 5.7 are based on data for the main wind direction of the calibration coinciding with the x-axis of the 2D-PSD, the general behavior of the calibration can be seen. Different inflow angles with respect to the 2D-PSD coordinate system will however yield different slopes for the linear fit in Figure 5.7 (b).

For a 2D calibration, the data of all inflow angles will inevitably have x- and y-components of either sign, which makes fitting a power law function to the data of all inflow angles Φ impossible. A solution to the problem of fitting the power law function to these data can be found by calibrating the magnitude

$$|s|(u, \Phi) = \sqrt{x^2 + y^2} \tag{5.1}$$

(a)

(b)
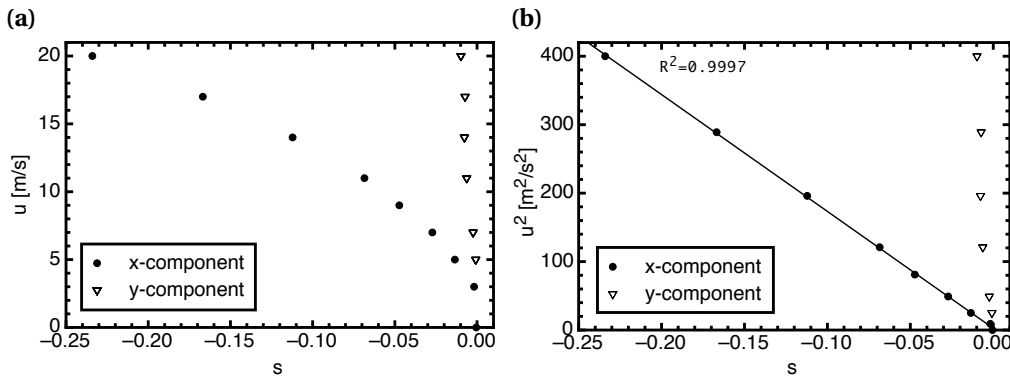
Figure 5.7: One-dimensional calibration function of the sphere anemometer recorded for 0°
inflow angle. (a) The x-component (solid bullets) follows a negative power-law function
while the y-component (open triangles) remains almost unchanged with increasing refer-
ence wind speed u. (b) Square of reference wind speed, u^2, plotted against the anemome-
ter's x- and y-signals. A linear regression line is fitted to the data for the x-component with
coefficient of determination $R^2 = 0.9997$.

of the anemometer signal rather than the two Cartesian components (x, y). Practically
this can be achieved quite conveniently by interpreting the (x, y)-components as real
and imaginary parts of a complex laser spot displacement $s = x + i\,y$. The magnitude
$|s|$ and phase angle Φ of the complex variable can than be determined to be modulus
and argument of the complex displacement

$$|s| = Mod(s)$$
$$\Phi = Arg(s). \tag{5.2}$$

One constraint of using the complex variable s is the requirement of the laser spot
position for $u = 0$ m/s to be at $(x = 0, y = 0)$ coordinates. Only for this case, the values
of the displacement magnitude and angle according to Equation (5.2) will be correct.
Although focusing the laser spot exactly in the center of the 2D-PSD area can be con-
sidered practically impossible, the constraint can be fulfilled by measuring the offset
for both coordinates and subtracting them from the signal prior to the conversion to
a complex coordinate s. The wind speed u plotted against the complex magnitude
of the displacement $|s| = |x + i\,y|$ may then be fitted with the power law function as
shown in the graph of the 1D calibration in Figure 5.8. The fit function according to
Equation (4.3) obeys almost a square-root shape with only a slightly deviating expo-
nent $n = 0.505$ and a slope $m = 40.33$.

5.2.4 2D Calibration Function

For the application of wind speed and simultaneous direction measurements, it is
necessary to perform a two-dimensional calibration of the sphere anemometer. There-
fore, the anemometer is rotated on the turntable along its vertical axis in angle incre-
ments of $\Delta\Phi = 5°$ and the corresponding signals $U_1 \dots U_4$ are recorded for the ref-
erence wind speeds u. The computed (x, y)-components of the 2D calibration are
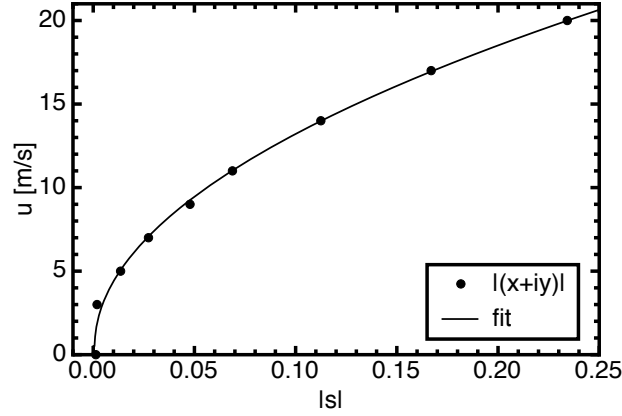
Figure 5.8: One-dimensional calibration function of the wind speed u plotted against the complex magnitude $|s|$ of the displacement signal (points). The data is fitted with a square-root-function (line).

plotted along with the reference wind speed u in the three-dimensional plot in Figure 5.9. As expected, the rotation of the one-dimensional power law function obtained in the previous section resembles a potential well. Although the three-dimensional plot gives an impression on the general shape of the 2D calibration function, it is difficult to assess even qualitative features like the uniqueness and isotropy of the calibration from this representation.

While the one-dimensional calibration function of Section 5.2.3 and the three-dimensional plot of the calibration in Figure 5.9 appear to be quite smooth and well-defined, the two-dimensional projection of the measured data in Figure 5.10 (a), corresponding to a top view on the active area of the 2D-PSD, reveals major deviations from the idealized expectations. In contrast to the expected axis-symmetric 2D calibration function – ideally a system of concentric circles – a significant variation of the radial displacement with changing inflow angle Φ can be identified from Figure 5.10. Additional clustering of the data for subsequent inflow angles Φ is apparent for wind speeds around 9 m/s (Fig. 5.10, b).

In a method to quantify the deviations from the rotational symmetry of the 2D calibration, the magnitude $|s|$ of the laser spot displacement from the 2D-PSD's center is considered. The single displacements $|s|(u, \Phi)$ for each combination of inflow angle and reference speed are compared to the ensemble average over all inflow angles Φ for one reference wind speed

$$\overline{|s_\Phi|(u)} = \frac{1}{N} \sum_\Phi |s|(u, \Phi) \qquad \text{with} \quad N = \frac{\Phi_{\text{max}}}{\Delta \Phi} \tag{5.3}$$

The angular bias of the displacement magnitude $|s|$ can be expressed in terms of normalized deviation from the angular mean

$$\chi = \frac{|s|(u, \Phi)}{\overline{|s_\Phi|(u)}} - 1, \tag{5.4}$$
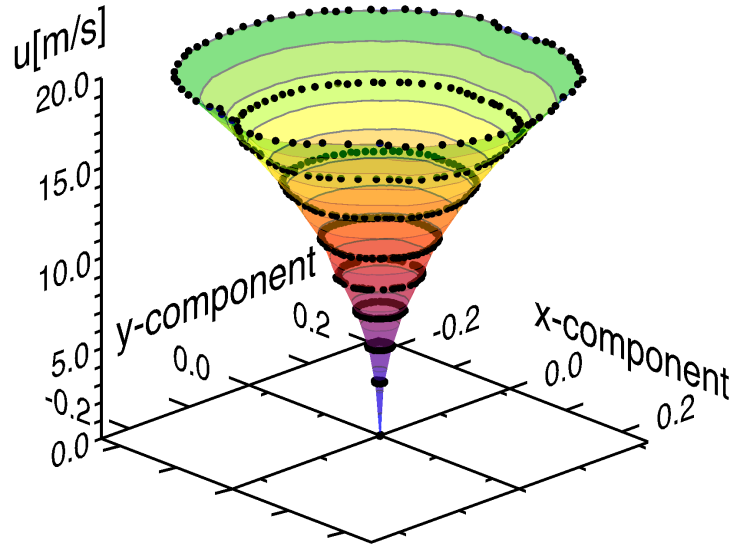
Figure 5.9: 3D plot of the two-dimensional calibration function of the sphere anemometer.

with values of $\chi < 0$ referred to as under-shooting while values $\chi > 0$ are called over-shooting. While this metric allows for the identifications of inflow angles with particularly strong deviations of the expected displacement magnitude $|s|$, it cannot cover the appearance of angular clustering found for medium wind speeds. The deviation of the measured and the set inflow angle, $\Phi_{\text{measured}} - \Phi_{\text{set}}$, can be used instead to identify these angular clusters and gaps. Both representations will be used for the characterization of this anemometer setup and the modified setups presented in the following.

Figure 5.11 shows the laser displacement magnitude $|s|$ as a function of the set inflow angle Φ for the measured reference wind speeds between 0 m/s and 20 m/s. The ensemble mean according to Equation (5.3) is also plotted for all wind speeds. The constant values $\overline{|s_\Phi|}(u)$ for each wind speed correspond to a circular shape of the 2D calibration. An increased laser displacement, i.e. values above average, is found in the inflow angle region of 20° to 60°. The plot of the angular dependence of the displacement magnitude $|s|$ in Figure 5.11 indicates large regions of significantly fluctuating values. Exemplary quantification of the deviations for 20 m/s reference wind speed show the largest over-shooting of up to 7% occurring between $\Phi \approx 20° \ldots 60°$. The region of $\Phi \approx 280° \ldots 340°$ is characterized by even stronger under-shooting of the displacement magnitude for this wind speed. Generally, the relative deviations are more severe for lower wind speeds as shown in the comparison of the maximal over- and under-estimation for each reference wind speed between 5 m/s and 20 m/s

(a)

(b)
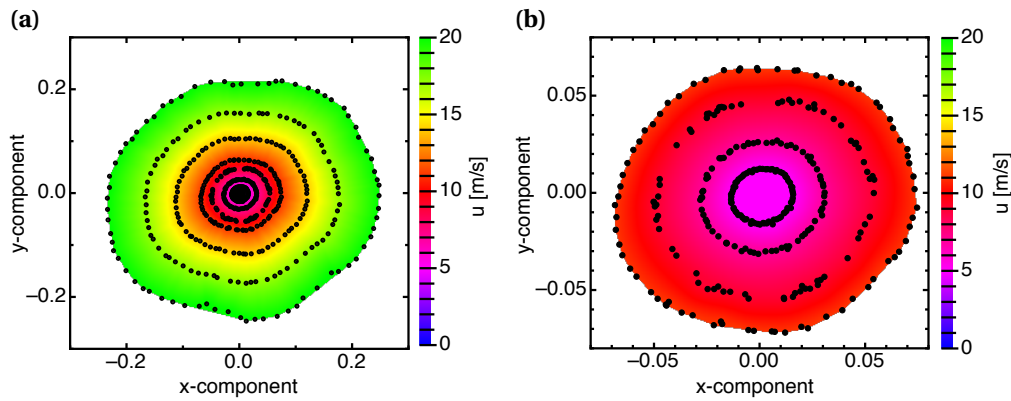
Figure 5.10: Projected two-dimensional calibration function of the sphere anemometer for (a) the full wind speed range and (b) wind speeds of 5–11 m/s. The reference wind speeds u are color-coded.

in Table 5.3.
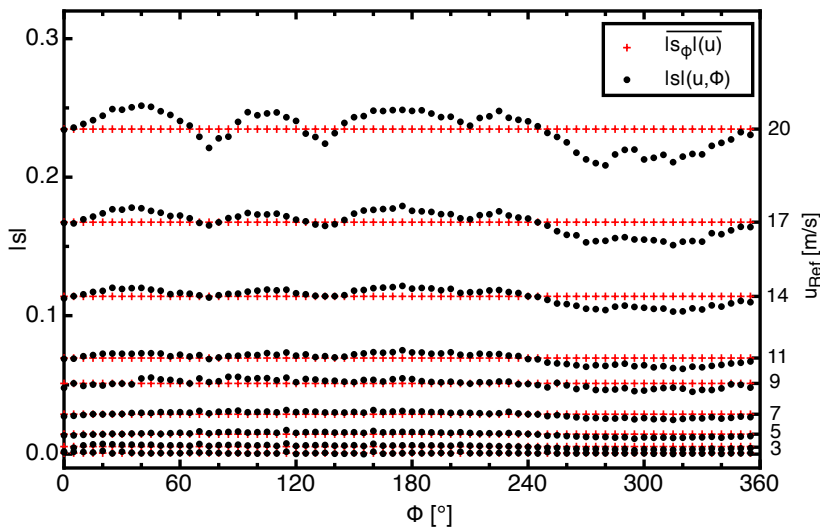
Figure 5.11: Dependency of the deflection magnitude $|s|$ on the inflow angle Φ for the 1$^{\text{st}}$ generation sphere anemometer. The largest relative deviations of around 20 % are found for low reference wind speeds, gradually decreasing to higher speeds. At the highest reference wind speed $u = 20$ m/s, the complex magnitude (black) is over-shooting the mean (red) by up to 7% for $\Phi < 240°$ and under-shooting the mean by about 11% for larger angles.

The difference of measured and set inflow angles $\Phi_{\text{measured}} - \Phi_{\text{set}}$ is plotted against the measured inflow angle Φ_{measured} for the wind speed range of 5 m/s to 11 m/s in Figure 5.12. Pronounced deviations exceeding $\pm 20°$ are found for $u = 9$ m/s reference wind speed. Some measured inflow angles exhibit particularly strong clustering, e.g. around 60° or 90°, while gaps are present at other measured angles, e.g. around 80° or 260°. Both, clusters and gaps, are not present for all displayed wind speeds, but the clustering for 9 m/s has already been seen in the pink and red areas of the 2D calibration function (Fig. 5.10). It is similar to the clustering seen in the 2D calibration of the

Table 5.3: Deviations χ of the displacement magnitude from the angular averaged displacement for a given reference wind speed u according to Eq. (5.4).

1st generation sphere anemometer							
u [m/s]	5	7	9	11	14	17	20
χ_{max} [%]	+20.2	+10.4	+9.3	+8.0	+6.6	+7.0	+7.2
χ_{min} [%]	-22.6	-14.1	-11.8	-11.3	-9.7	-9.9	-11.2
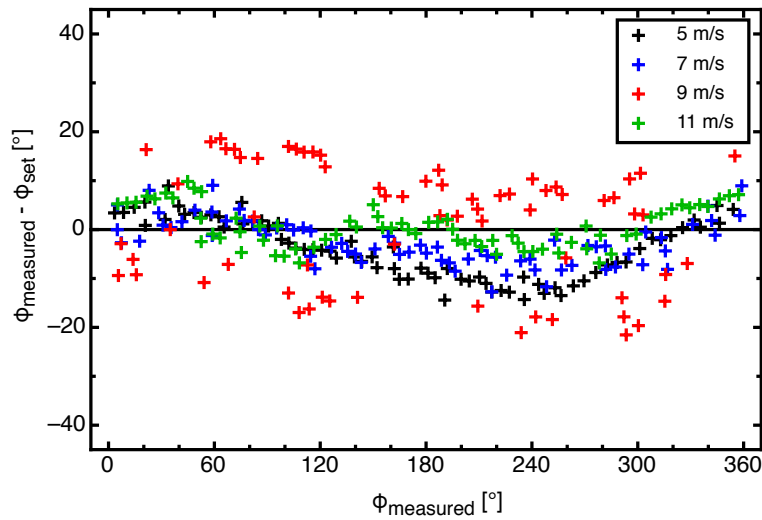
Figure 5.12: Deviation of the measured inflow angle from the set inflow angle as function of measured angle for the 1st generation sphere anemometer setup with GFP tube and regularly dimpled sphere.

previous sphere anemometer setups [Heißelmann et al., 2008]. Although the clustering itself can be identified, the cause cannot be isolated from the measurement data with regularly dimpled sphere, since it is fixed to the GFP tube and cannot be substituted. It can thus be either an anisotropy of the tube material or an influence of the regularly dimpled sphere surface. A more detailed investigation of the impact of the sphere surface pattern on the sphere anemometer calibration is necessary and requires some changes to the sphere anemometer setup, which are addressed in Section 5.3.

5.3 Impact of Sphere Patterns and Tube Material on the Calibration

The results of the previous section give rise to the question whether the sphere surface pattern or the tube material is the root cause for the angular deviations and clustering of the anemometer's 2D calibration. While the overall design of the anemometer is unaltered with regard to its housing and the position sensing electronics, some minor

setup modifications of the 1$^{\text{st}}$ generation sphere anemometer are required.

A GFP tube with the same length l and radii R_i and R_o as described in Section 5.1 is used, and as the sole change an aluminum jacket with thread is added to its tip, in order to allow for the substitution of the sphere while keeping the exact same tube. Three hollow spheres with 70 mm diameter are designed and produced from ABS plastics by means of rapid prototyping. Their lower pole features a thread in order to mount and unmount it to the tube. All spheres have the same dimensions as before to maintain the same Reynolds number range of operation for the sphere anemometer. They differ in their surface patterns, though.

Irregular, surface-filling dimples   To improve the surface pattern of the dimpled sphere, two spheres with irregularly placed dimples are produced. The focus for this surface pattern is to obtain an equally distanced distribution of the dimple centers across the sphere surface.

A completely covered surface with equally sized patterns can be easily achieved for the alignment of the pattern centers in one flat plane. Once the same constraint has to be fulfilled on a spherical surface, the task turns out to be non-trivial and resembles the "Thomson problem", which arises from the model of the atom proposed by J. J. Thomson in 1904 – the so-called "Plum Pudding Model". Wales and Ulker [2006] used Monte Carlo Simulations to solve the problem for several numbers of ions N, where each ion corresponds to one pattern center. Although the distribution of these centers on a sphere surface will inevitably result in some defects, it can be considered a close enough match to the stated goal of equally distributed dimples for the sphere anemometer application. The coordinates for N=812 ions shared in the Cambridge Cluster Database[9] are used for the placement of the dimple centers on the sphere surface during the design of the two spheres with surface-filling dimple patterns.

The coarsely dimpled version of this sphere shown in Figure 5.13 (a) has 812 dimples of similar diameter d and depth k as the regularly dimpled sphere ($d = 4.9 \pm 0.1$ mm, $k = 1.3 \pm 0.1$ mm) of the previous setup. Thus, the roughness parameter k/D introduced in Section 3.2 is also similar for these two spheres.

The fine dimpled sphere depicted in Figure 5.13 (b) has also 812 dimples, which are centered in the same positions but differ in diameter and depth from its coarse sibling as listed in Table 5.4. Hence, the surface is not filled with dimples but still the irregular alignment is maintained. This also yields a small difference of the weights of both spheres, due to a deviation in wall thicknesses.

Both irregularly patterned spheres have a hole with a tubular joint at their bottom poles. Unlike the regularly dimpled sphere, they are made as one piece and feature an aluminum thread, which permits the substitution of the spheres while still using the same tube and laser diode on the sphere anemometer. Consequently, it may be discriminated between effects stemming from tube material and sphere surface during

---

[9]http://www-wales.ch.cam.ac.uk/CCD.html
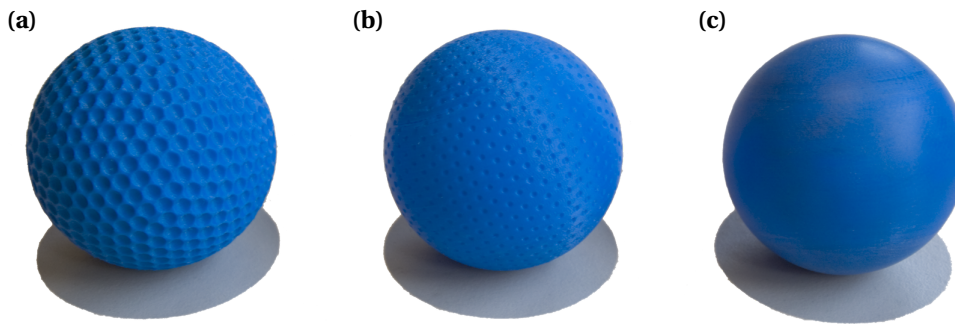
Figure 5.13: Photo of the re-designed spheres with coarse (a) and fine (b) surface-filling dimple patterns as well as smoothly sanded surface (c).

the anemometer characterization.

Smooth sphere In order to be able to compare the obtained data using the different dimpled sphere patterns, investigations are also performed with a smooth sphere of the same size (Fig. 5.13, c). This sphere is produced as one piece in the same fashion as the two surface-filled spheres and also features a tubular joint with aluminum thread at the bottom pole. The production process via rapid prototyping causes some imperfections of the sphere surface, which are mainly apparent at the poles of the sphere. The roughened surface at the poles is due to the minimal step size of the plastic layers produced by the 3D printer. In order to avoid roughness effects on the boundary layer of the sphere, the surface is sanded in several steps and afterwards polished. Although the surface roughness was not measured for the smooth sphere, a mean roughness $\sim 0.8\mu$m can be assumed based on the described surface treatment [Labisch and Weber, 2013, p. 119]. It is therefore given instead of the dimple depth for the smooth sphere.

An overview of the specifications of the different patterned spheres and the smooth sphere is given in Table 5.4. Despite the addition of an aluminum thread at the bottom pole of the re-designed spheres, the total weight of the irregularly dimpled and smooth spheres is reduced by more than a factor of two due to thinner walls, which are enabled by the production as one piece. The weight between the three different spheres varies by a couple of grams because of the different surface patterns.
Figure 5.14 shows a photo of the assembled 1$^{\text{st}}$ generation sphere anemometer with aluminum housing and coarse surface-filling dimpled sphere.

5.3.1   1D Calibration Function with Different Spheres

One-dimensional calibration functions are measured for the sphere anemometer with each of the three different spheres in the same procedure as described in Section 5.2.3. Aerodynamic characteristics like the flow separation point or the drag are quite sensitive to the surface properties and may be prone to hysteresis. In order to rule out

Figure 5.14: Improved sphere anemometer with impermeable, dome-shaped aluminum housing. The coarsely dimpled sphere with surface filling pattern is attached to the GFP tube. The supply cables for the laser are fixed to the downstream side of the tube and covered with a shrinking hose to reduce oscillations.

Table 5.4: List of sphere properties. Dimple number N, dimple diameter d, dimple depth k and roughness parameter k/D are given for the patterned spheres only, while sphere diameter D and mass M_s are given for all spheres.

pattern	N	d [mm]	k [mm]	k/D	M_s [g]
smooth	–	–	0.0008	$1.14 \cdot 10^{-5}$	$13.6 \pm 0.1^*$
regular dimples	306	4.93	1.3 ± 0.2	0.0186	38 ± 0.1
irregular, fine	812	2.08	$0.2 \pm$	0.0014	$16 \pm 0.1^*$
irregular, coarse	812	4.3	1.3 ± 0.2	0.0186	$15.7 \pm 0.1^*$

* weight incl. thread

effects of hysteresis in the assessment of the 1D calibration function of the anemometer with dimpled spheres, the calibrations are performed three times with alternating order of reference wind speeds u. The first and third calibration start at a reference wind speed $u = 0$ m/s, which is then stepwise increased to 25 m/s, while the second calibration is carried out in reversed order starting at $u = 25$ m/s. This procedure is employed for the 1D calibration with both dimpled spheres and the output results are compared to the baseline case of the anemometer with smooth sphere surface.

Figure 5.15 (a) shows the three recorded 1D calibrations for the fine dimpled sphere while the 1D calibration for the coarsely dimpled sphere is shown in Figure 5.15 (b). Both plots also include the 1D calibration of the anemometer with smooth sphere for comparison, and all calibrations were fitted using a power law function according to Equation (4.3). The fit parameters obtained for each calibration function are given in Table 5.5 along with the mean values for the respective sphere pattern.

The three measured instances of 1D calibration functions with fine sphere pattern exhibit only little variation and it can therefore be concluded, that hysteresis effects do not affect the resulting calibrations. The three calibrations are not differing among each other, but the 1D calibration with smooth sphere in Figure 5.15 (a) shows a clearly different shape. This manifests in the obtained fit parameters summarized in Table 5.5. While the calibration with smooth sphere is characterized by an almost perfect square-root dependence with exponent $n = 0.505$ and slope $m = 39.22$, the average fit exponent and slope, $n = 0.535$ and $m = 43.91$, are larger for the fine dimpled sphere. The same behavior is found for the comparison of the three 1D calibrations measured with the coarsely patterned sphere with irregular dimples (Fig. 5.15, b). While the overall variation between the three calibrations is small and any effects of hysteresis can be ruled out, a pronounced difference from the smooth baseline case is observed. Again, the averaged fit parameters $n = 0.54$ and $m = 43.5$ are larger than for the smooth sphere.

The increased exponent n and slope m of the 1D calibration function with both patterned spheres implies, that the same reference wind speed u causes smaller laser displacements $|s|$. It indicates a reduction of the drag coefficient for these spheres

(a)

(b)
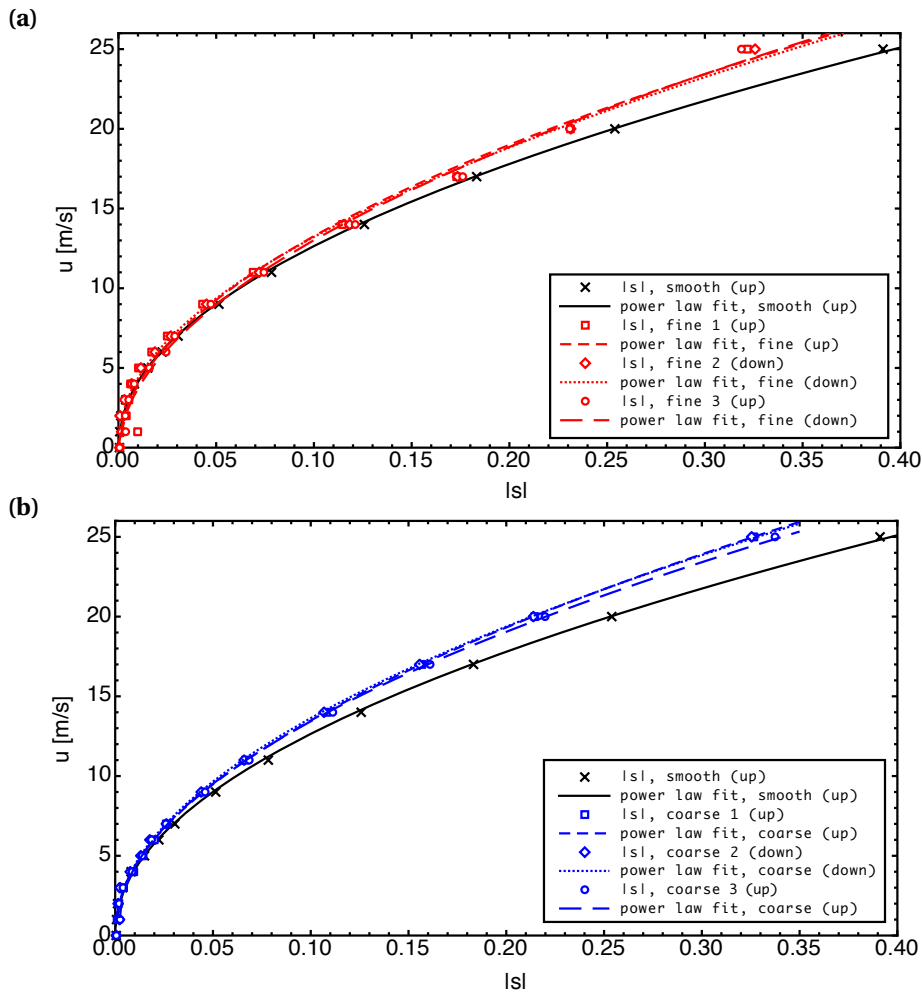
Figure 5.15: One-dimensional calibration data and power law fit functions of the sphere ane-
mometer for (a) fine dimpled and (b) coarsely dimpled sphere. The calibration for each
sphere is measured three times and compared to the calibration function with smooth
sphere (black).

compared to the smooth sphere, which is matching with the expected effects of the
surface patterns stated in Section 3.2.

A comparison of both dimpled spheres is based on the first of the three obtained 1D
calibrations, since the differences within one triplet are negligible. The 1D calibra-
tions for both dimpled spheres are shown in Figure 5.16 along with the 1D calibration
of the smooth sphere. While both patterned spheres deviate from the smooth case as
already observed in Figure 5.15, only minimal differences between the fine and coarse
dimple patterns are apparent. This is confirmed by the rather small differences in the
average exponent n and slope m for the power law fits of the 1D calibrations with
both spheres (Tab. 5.5). It is a strong indication of a similar drag coefficient c_D for
both considered dimpled spheres. As a consequence, all further investigations are
focusing on the coarsely dimpled sphere and the smooth sphere only.

Table 5.5: Comparison of fit parameters for one-dimensional calibrations for both irregularly dimpled spheres.

	irregular fine dimples			irregular coarse dimples		
	m	s_0	n	m	s_0	n
$0 \rightarrow 25$ m/s	43.59	$0.729 \cdot 10^{-3}$	0.518	44.45	$1.0394 \cdot 10^{-3}$	0.549
$25 \rightarrow 0$ m/s	42.66	$1.74 \cdot 10^{-3}$	0.55	43.59	$1.678 \cdot 10^{-3}$	0.537
$0 \rightarrow 25$ m/s	44.47	$1.23 \cdot 10^{-3}$	0.54	42.46	$2.598 \cdot 10^{-3}$	0.533
average	43.91	$1.234 \cdot 10^{-3}$	0.535	43.5	$1.771 \cdot 10^{-3}$	0.54
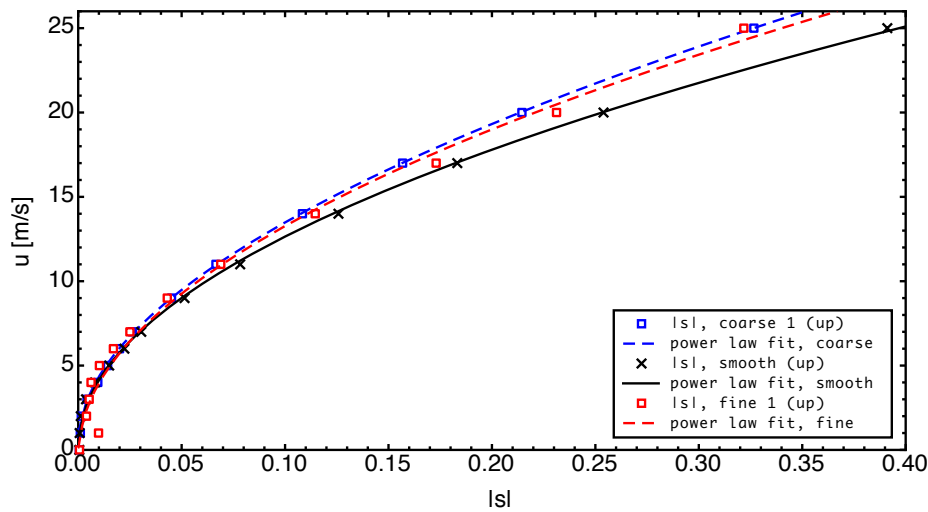
Figure 5.16: One-dimensional calibration and power law fit of the 1st generation sphere anemometer with fine dimpled (red), coarsely dimpled sphere (blue) and smooth sphere (black).

5.3.2 2D Calibration Function with Different Spheres

The angular effects of the sphere surface pattern are assessed in the two-dimensional calibration. Results from the anemometer with mounted regularly dimpled sphere presented in Section 5.2.4 give rise to the question whether the tube material or the sphere pattern is the cause for the deviations from the circular shape. The observed clusters and gaps were particularly pronounced in the wind speed range of 5–11 m/s of this 2D calibrations, and this range is therefore investigated for one distinct GFP tube with the replaceable smooth and coarsely dimpled spheres. A set of 2D calibrations is measured for the sphere anemometer with both spheres using the procedure described in Section 5.2.2. Figure 5.17 shows the projected 2D calibrations of both cases using the same color scale for the wind speed range as previously used (Fig. 5.10).

Larger displacements of the measured data from the center are observed for the
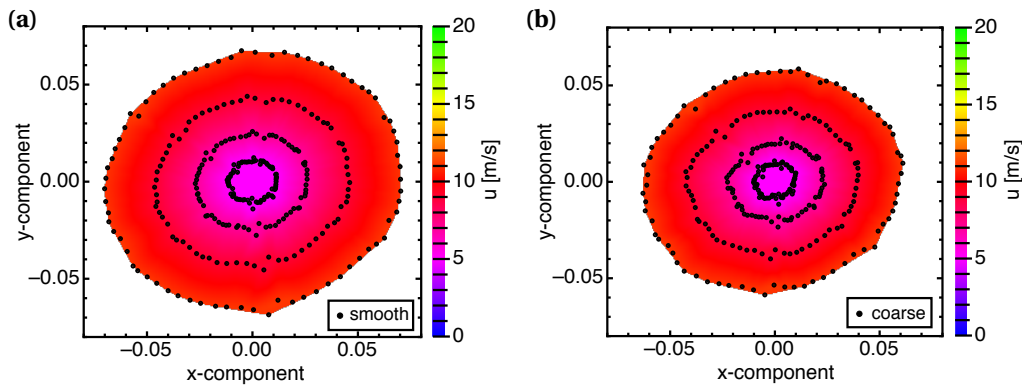
Figure 5.17: Projected plot of the two-dimensional calibration functions of the sphere ane-
mometer with (a) smooth and (b) irregularly coarsely dimpled sphere. The reference wind
speed u in the range of 5–11 m/s is color-coded. Sudden jumps attributed to the tube struc-
ture are present across all wind speeds with a periodicity of about 60°.
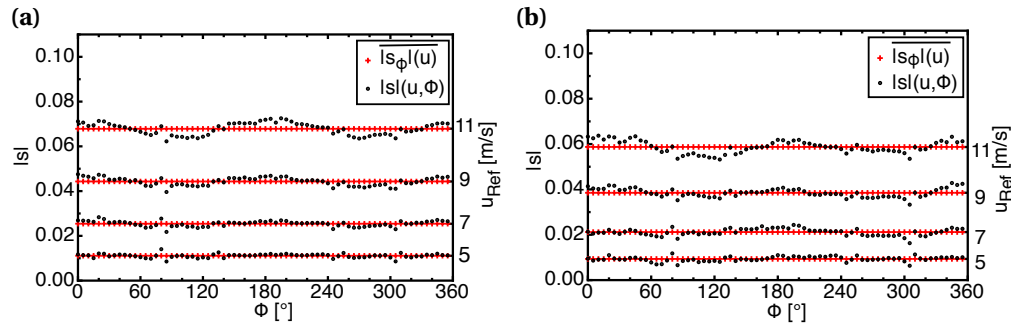
Figure 5.18: Dependency of the deflection magnitude $|s|$ on the inflow angle Φ for the 1ˢᵗ
generation sphere anemometer setup with GFP tube and (a) smooth and (b) irregularly,
coarsely dimpled sphere.

2D calibration with smooth sphere (Fig. 5.17, a) in comparison to the calibration with
coarsely dimpled sphere (Fig. 5.17, b). This is consistent with the results of the 1D cal-
ibrations in the previous section, since the lower drag coefficient of the coarse sphere
yields smaller forces and consequently smaller laser displacements for the same ref-
erence wind speed. Moreover, both 2D calibrations exhibit regions with high scatter
and even sudden jumps.

These six pronounced jumps appear in both calibrations in a rather regular pat-
tern with a periodicity of about 60°. The considerations of Section 5.2.4 are analo-
gously followed, as the deviation of the measured displacement magnitude $|s|(u, \Phi)$ is
compared to the angular mean displacement $\overline{|s_\Phi|(u)}$ for each reference wind speed u,
to grasp this effect in more detail. Both quantities are plotted in Figure 5.18 against the
set inflow angle Φ for the smooth and coarsely dimpled sphere. An angular deviation
is present for both investigated spheres. Additionally, the jumps in the displacement
magnitude are found in both plots for similar inflow angles Φ at approximately 20°,
80°, 140°, 190°, 250° and 310°.

A closer look at the deviation of the measured inflow angle Φ_{measured} from the set
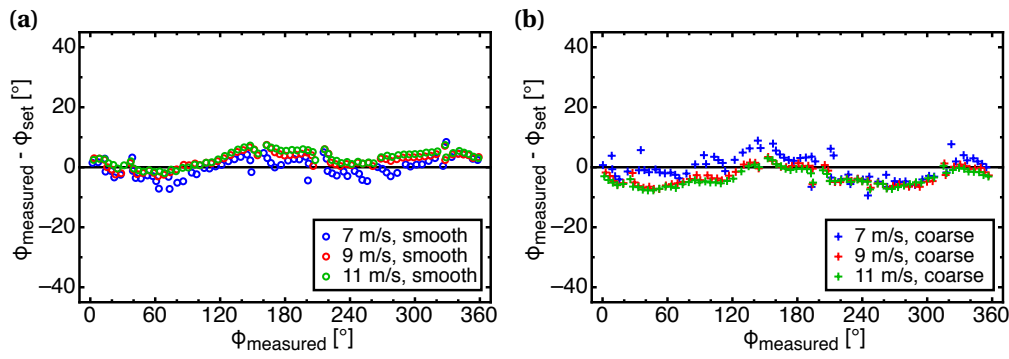
Figure 5.19: Deviation of the measured inflow angle from the set inflow angle as function of measured angle for the 1st generation sphere anemometer setup with GFP tube and (a) smooth and (b) irregularly, coarsely dimpled sphere.

inflow angle Φ_{set} is presented in Figure 5.19 for both examined sphere surfaces. The deviation $\Phi_{measured} - \Phi_{set}$ is plotted against the measured angle $\Phi_{measured}$ for reference wind speeds between 7 and 11 m/s in order to identify systematic errors and to quantify the impact of the jumps seen in Figure 5.17. Both plots show some systematic deviations from the set angles across all measured angles. The magnitude of these deviations has been greatly reduced from more than $\pm20°$ for the regularly dimpled sphere to about $\pm10°$ for the re-designed spheres. The more striking feature of both plots is however the appearance of gaps at distinct measured inflow angles for each reference wind speed. They are more pronounced for 7 m/s and 9 m/s reference wind speed, which has also been observed in the 2D calibration function with the regularly dimpled sphere in Section 5.2.4. These gaps occur at about 30°, 150°, 220° and 320° measured inflow angle for both spheres, which strongly indicates the independence of the angular gaps from the sphere surface.

Consequently, the structures identified in the 2D calibration functions of smooth and coarsely dimpled sphere can be attributed to the properties of the tube instead of the sphere surface. It can also be concluded from the rather constant positions of the jumps in Figure 5.18, that the tube material exhibits a kind of angle-dependent resistance to strain with a periodicity of about 60°. The root cause for this effect is suspected to originate from the fiber alignment within the glass-fiber matrix of the tube. As mentioned in Section 5.1, the fiber orientation is not known and it is also not possible to assure isotropy in this regard. The GFP material of the tube can thus be considered a crucial issue for the quality of the angular calibration of the sphere anemometer, which needs to be addressed for further improvement of the sensor.

5.4   Temporal Resolution & Natural Frequency

The temporal resolution of the sphere anemometer is related to its natural frequency, as described in Section 4.3. It constitutes an upper boundary to the detectable temporal variations in the flow and any flow pattern of similar or higher frequency than

the natural frequency will be masked by the resonant oscillation of the sensor itself.

The dynamics of the sphere anemometer can be assessed by mechanical excitation of the sensor, which can be achieved by exposing the sphere anemometer to wind flow. As pointed out in Section 4.3, the sphere is subject to vortex shedding like any bluff body, and the induced vibrations will appear in the spectral analysis. It is characterized by the non-dimensional Strouhal number St (Eq. (4.4)), which can be considered a constant of $St \approx 0.19$ in the treated Reynolds number range. For the investigated spheres with diameter $D = 70$ mm, the vortex shedding frequency

$$f_u = \frac{u \cdot St}{D} \qquad\qquad (5.5)$$

thus varies with the flow velocity u. Exploiting this relation, the velocity-dependence of f_u can be utilized to distinguish the vortex shedding frequencies from the material- and geometry-dependent natural frequencies f_0 of the anemometer, which will not be altered with changing wind excitation. The experimental characterization is therefore performed for a set of three different wind speeds u for each sphere-tube-combination and the power spectra of the displacements $|s|$ are computed.

The dynamic response behavior of the 1st generation sphere anemometer is assessed for the initial setup with GFP tube and fixed, regularly dimpled sphere (Sec. 5.1) as well as for the modified setup using the spheres with smooth and irregular, coarse dimple pattern supported by the same GFP tube. The characterization is performed in an experimental setup similar to the calibration setup of Section 5.2 with the anemometer placed on top of the turntable in front of the acoustic wind tunnel nozzle. Its x-component is aligned in 0° position of the 2D-calibration function, i.e with the main flow direction, and the four signals of the 2D-PSD are simultaneously acquired at a sampling rate of 1 kHz for 10 seconds per wind speed u. (x, y)-components and the complex spot displacement s are calculated during post-processing.

The sphere anemometer with regularly dimpled sphere is exposed to three different reference wind speeds $u = 9$ m/s, $u = 14$ m/s and $u = 17$ m/s. Theoretically expected vortex shedding frequencies corresponding to the reference wind speeds are $f_{u=9} = 24$ Hz, $f_{u=14} = 38$ Hz and $f_{u=17} = 46$ Hz, while the theoretical natural frequency of the setup is $f_0 \approx 15$ Hz, according to Equation (4.6).
The power spectral density of the complex signals for each wind speed is plotted against the frequency f in Figure 5.20. Each power spectrum contains three prominent peaks at approximately 8 Hz, 19 Hz and 39 Hz, while other peaks with less intensity are present at higher frequencies. The highest peak at 19 Hz is not coinciding with the expected Strouhal frequency $f_{u=9}$ for 9 m/s inflow and it is also present for the two higher wind speeds. Both other peaks cannot be linked to the vortex shedding frequencies either and since none of them is shifting towards higher frequencies with increasing wind speeds, they are presumably related to the sphere anemometer's natural frequency. Given the uncertainties in the estimation of the elasticity modulus E of the GFP tube, the highest peak at $f_0 = 19$ Hz close to the expected value of 15 Hz
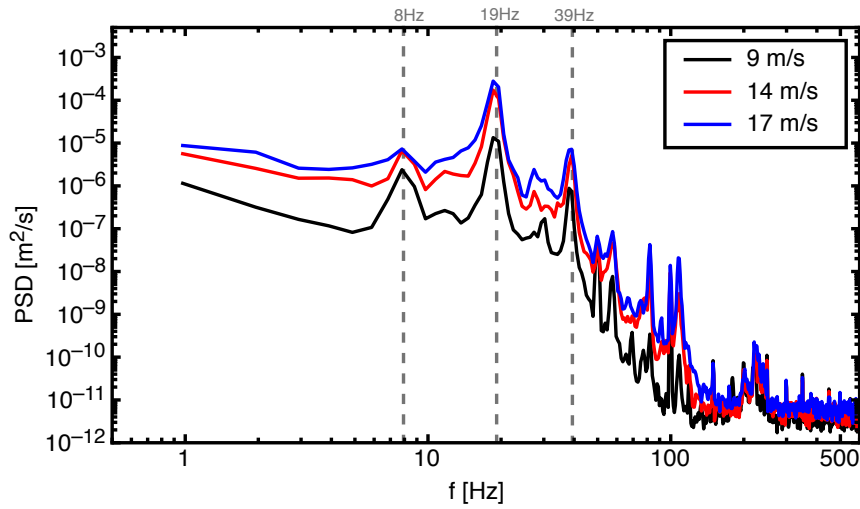
Figure 5.20: Power spectrum of the complex displacement magnitude of the 1$^{\text{st}}$ generation sphere anemometer with regularly dimpled sphere for 9 m/s (black), 14 m/s (red) and 17 m/s (blue) inflow velocity. The dashed lines mark the natural frequency $f_0 \approx 19$ Hz and its first harmonic and sub-harmonic frequency.

can be considered the anemometer's natural frequency. Its first harmonic is found at $f_0' \approx 39$ Hz and the 8 Hz peak might be a sub-harmonic oscillation frequency.

The re-design of the sphere, employing different surface patterns, was triggered by the flaws of the 2D calibration and not by the aim for an improved frequency response. However, the re-designed spheres feature significantly reduced masses, as listed in Table 5.4. This yields a reduction of the tip mass and thereby affect the anemometer's natural frequency. Consequently, the theoretically expected natural frequencies are increased to $f_0 = 23$ Hz and $f_0 = 25$ Hz for the sphere anemometer with coarsely dimpled and smooth sphere, respectively. The expectations for both cases are compared to experimentally determined natural frequencies. A similar experiment as presented above is therefore carried out, where the sphere anemometer with both spheres is exposed to reference wind speeds $u = 9$ m/s, $u = 14$ m/s and $u = 25$ m/s. Corresponding Strouhal frequencies are $f_{u=9} = 24$ Hz, $f_{u=14} = 38$ Hz and $f_{u=25} = 67$ Hz, respectively.

The calculated power spectra of the measurements with both spheres are depicted in Figure 5.21. Two pronounced peaks are present in the power spectral density for the three different reference wind speeds measured with the smooth sphere surface in Figure 5.21 (a). The peaks coincide in frequencies of $f_0 \approx 30 \pm 1$ Hz and $f_0' \approx 60 \pm 1$ Hz and are of similar magnitude for all wind speeds. They do not match the expected Strouhal frequencies f_u, though, and they can thus be identified as the natural frequency of the sphere anemometer and its first harmonic.

The plot of the power spectral density for the sphere anemometer with coarsely dimpled sphere is almost identical to the case with smooth sphere. However, the determined natural frequency of $f_0 \approx 28 \pm 1$ Hz and its harmonic $f_0' \approx 57 \pm 1$ Hz are reduced,
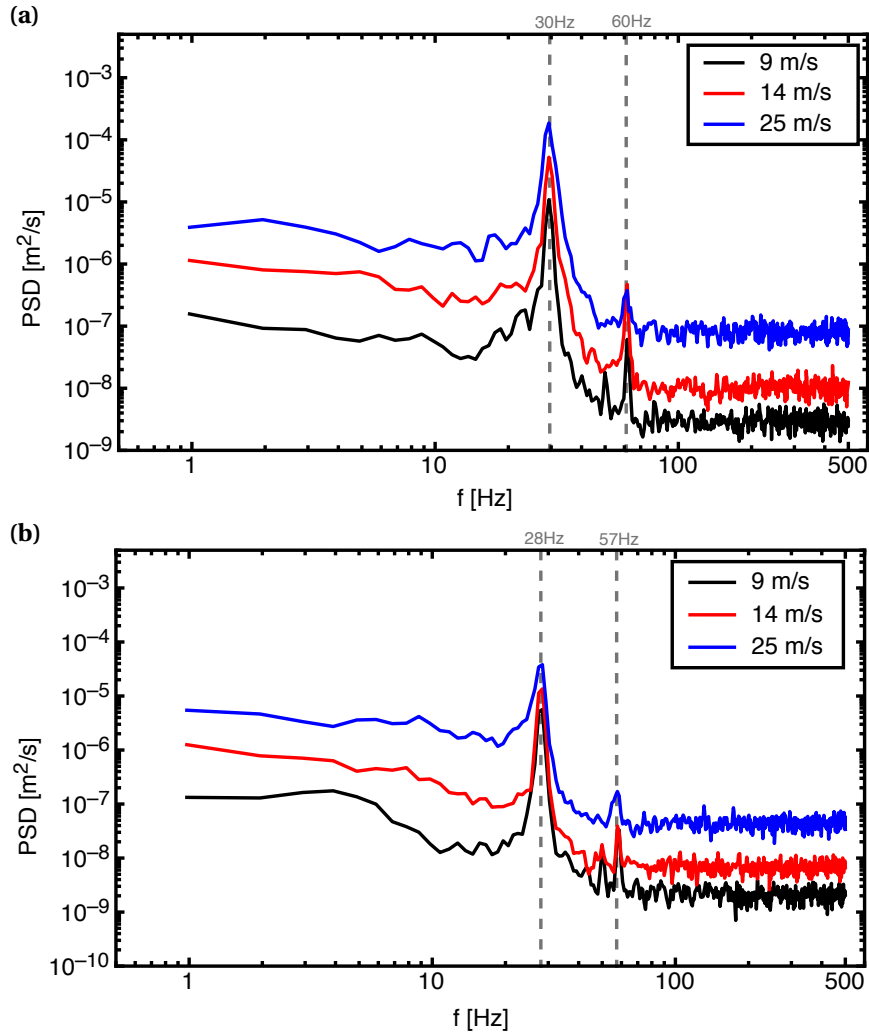
Figure 5.21: Power spectrum of the complex displacement magnitude of the 1$^{\text{st}}$ generation sphere anemometer with (a) smooth sphere and (b) coarsely dimpled sphere for different reference wind speeds. Two peaks at the natural frequency $f_0 \approx 30$ Hz and its first harmonic $f_0' \approx 60$ Hz are observed.

as is the magnitude of the frequency peaks. The reduction of the natural frequency is expected due to the slightly heavier coarsely dimpled sphere. Although the values of the natural frequencies for either sphere are not exactly predicted due to uncertainties in the measured elasticity modulus of the tube, the predicted difference between the to spheres matches the experimentally determined difference well. The reduced magnitude of the spectral peaks – albeit it is not very pronounced – is an indicator for minimally reduced vortex shedding by the patterned sphere surface and it thus consistent with theoretical expectations.

Considering these findings, the limit of the temporal resolution of the 1st generation sphere anemometer with re-designed sphere, given by the natural frequency, is beyond 20 Hz. In this regard, it enables the sphere anemometer to compete with commercial sonic anemometers, which are typically operated at 10–20 Hz. Despite this encouraging result of the anemometer assessment, improvements towards higher natural frequencies exceeding 35 Hz are desirable to challenge the fast operational mode of the high-end Gill WindMaster Pro 3D sonic anemometer, which is used as a reference sensor within this work.

5.5   Summary & Discussion

The 1st generation sphere anemometer was set up based on the anemometer principle introduced in Chapter 3. The polystyrene sphere of previous setups was replaced with a more robust ABS sphere with regularly dimpled surface. The calibration procedure for the sphere anemometer was introduced and calibration functions of the one-dimensional and two-dimensional signals were analyzed. The characterization revealed an angular dependence of the sphere anemometer signal, which also showed pronounced clustering and gaps for some wind speeds. The angular response has been quantified by means of the deviation from a perfectly circular 2D calibration function and by means of difference between set and measured inflow angles. Modifications to the sphere and support were made to enable the discrimination of the impact of the sphere and the support tube on the calibration. Measurements were performed for one tube combined with three spheres with different surface patterns – a smooth sphere and two spheres with irregularly aligned dimples of different size. 1D calibrations for both dimpled spheres were steeper than for the smooth sphere, which confirmed the expectation of a drag reduction by means of the surface roughness. However, no significant difference between the two dimpled spheres was found and the fine dimpled sphere was therefore discarded for further tests. 2D calibrations for the sphere anemometer with smooth and coarsely dimpled sphere were compared for the wind speed range with the most severe angular effects. Both calibrations functions exhibited a similar pattern of periodic jumps of the displacement magnitude, which indicates an angle-dependent strain behavior of the GFP tube. The fiber alignment of the material seems to be the root cause for this effect and strongly demands

for a better suited tube material in order to improve the anemometer setup.

The temporal resolution of the anemometer setup has been assessed theoretically based on the considerations in Section 4.3 and experimentally based on the anemometer's frequency response to wind flows of different velocities. Power spectra of the anemometer with regularly dimpled sphere have therefore been analyzed as well as for the re-designed spheres with smooth and coarsely dimpled pattern. Several frequency peaks were found in the power spectra for the regularly dimpled sphere, and as none of them coincided with the expected vortex shedding frequencies, they were attributed to be the anemometer's natural frequency of 19 Hz and its harmonics. The power spectral analysis of the sphere anemometer with the much lighter re-designed spheres included two pronounced peaks of the natural frequency and its harmonic. They varied only slightly between the two spheres due to their different mass. The natural frequency was increased to 30 Hz and 28 Hz for the smooth and dimpled sphere, respectively, and they agree reasonably well with the theoretical expectations. The sphere anemometer with re-designed spheres consequently provides a temporal resolution in the range of commercial sonic anemometers.

Chapter 6

The Second Generation Sphere Anemometer

This Chapter introduces the improvements made to the sphere anemometer design based on the findings of Chapter 5 and presents the resulting 2nd generation sphere anemometer. Particular emphasis is given to the choice of a more favorable tube material and the required re-design of the anemometer. The one- and two-dimensional calibrations of the anemometer are treated analogously to the analysis of the previous anemometer setup.

6.1   Sphere Anemometer Setup

Investigations in Chapter 5 identified the fiber structure of the glass-fiber reinforced plastics (GFP) tube to spoil the isotropy of the 2D calibration function of the 1st generation sphere anemometer. A different tube material is therefore used in the 2nd generation sphere anemometer to improve the calibration and make the anemometer more reliable. Since thermoplastics are prone to creeping and fiber materials are excluded for their anisotropic strain behavior, stainless steel is chosen as a tube material instead.

Although stainless steel is not prone to creeping, isotropy is identified as an issue in first feasibility experiments with commonly rolled and welded tubes. The welding seam causes a sudden change in strain behavior of the tube for a narrow range of inflow directions. This is avoided by the choice of a tube which has been cold-drawn to its final dimensions instead of the usual rolling and welding process. These seamless tubes are slightly more expensive than regular tubes, but the cold-drawing eliminates the anisotropies otherwise caused by the weld seam and enhances the precision of their diameter and wall thickness along its span [Kötter, 2009]. Hence, a cold-drawn tube made of stainless steel (1.4301) is selected for the 2nd generation sphere anemometer setup presented in the following.

The elasticity modulus of the stainless steel material is measured in a strain exper-

iment[10] as an input for the anemometer design process. The determined elasticity of $E \approx 100$ GPa makes the stainless steel tube about three times stiffer than a comparable glass-fiber tube of similar dimensions. Considering Equation (3.2) for the tip displacement of the tube, one way of handling the higher stiffness EJ would be to simply increase the tube length to $l = 330 \pm 0.05$ mm, so that the displacement of the laser spot for a given wind speed would be similar to the previous anemometer with GFP tube ($l = 285 \pm 0.05$ mm). A consequence of this approach would inevitably be a reduction of the anemometer's natural frequency and thus also its temporal resolution. This is – to some extent – avoided by the choice of a stainless steel tube with reduced wall thickness. While the outer radius of the tube $R_o = 4.0 \pm 0.05$ mm is unaltered from the previous anemometer generation, the inner radius has been increased to $R_i = 0.38 \pm 0.05$ mm, i.e. the wall thickness has been reduced from 0.5 mm to only 0.2 mm.

Additional considerations for the anemometer optimization take the desired dynamic response of the sensor into account. Hence, the tube length is chosen on the condition of pushing the natural frequency of the sphere-tube-combination to approximately $f_0 \approx 35$ Hz in order to obtain a temporal resolution comparable to sonic anemometers (~ 32 Hz). This is achieved with a stainless steel tube of $l = 215 \pm 0.05$ mm length from the housing to the center of the sphere, which coincides with the lens of the mounted laser diode. Despite the reduced wall thickness, the shorter tube yields a reduction of the tip deflection of the sphere, which consequently affects the measuring range and sensitivity of the anemometer. This is compensated by tuning the optical amplification of the signal, i.e. increasing the distance L between the laser diode and the two-dimensional position sensitive detector (2D-PSD) as sketched in Section 3.3. In order to achieve the necessary amplification and increased optical path, a larger housing is constructed for the 2nd generation sphere anemometer. It consists of a tubular housing with rounded top cover, which is fitted with a thread at its center to fix the substitutable sphere-tube-element, as sketched in the drawing in Figure 6.1 (a). A large cover plate at the back of the anemometer housing provides access to the sensor interior with the amplifier electronics and the 2D-PSD (Fig. 6.1, b).

A threaded sphere mount, similar to the type used in the previous sphere anemometer, is bonded to the top part of the steel tube. A second thread at the bottom end is fitted with two cable channels to allow for the connection of the laser diode to the power supply without causing a gap in the anemometer housing. Two filigree plastic coated single copper wires of $\varnothing = 0.37 \pm 0.01$ mm diameter are used for the laser connection. Both wires are helically wound around the outside of the tube and covered with a shrinking hose in order to reduce the directional dependency of the cross-section. The helical alignment can also reduce vortex induced vibrations since the wires serve as helical strakes, as they are often used to stabilize large chimneys from wind induced vibrations [Scruton and Eugene, 1963]. Larger diameter speaker

---

[10]The value was measured in a strain experiment operated by Andreas Häussler of the Acoustics Research Group, University of Oldenburg.

cables are used inside the anemometer housing to improve the robustness of the connection to the plug of the anemometer's data cable.

The sphere mount at the top of the tube allows for the use of different spheres. However, only the 2nd generation sphere anemometer with attached smoothly sanded sphere is treated in the following. This is on the one hand motivated by the results from Chapter 5 regarding the regularly dimpled and irregularly, finely dimpled sphere. On the other hand, the coarsely dimpled sphere can be expected to be prone to dirt accretion in field applications and it is therefore excluded. The specifications of the smooth sphere are listed in Table 5.4 in Section 5.3.

The tip displacement of the sphere-tube-element is measured based on the light pointer principle, as employed in the previous anemometer setup, also using a ADL-65055SA2 laser diode with 5 mW maximum output power and 3.3 mm package. The lens holder carrying a 5.2 mm plastic collimator lens CAW100 has been slightly adapted to the larger inner radius of the stainless steel tube to provide a rigid fit, but is otherwise similar to the description in Section 5.1. The proven combination of Hamamatsu S5990-01 2D-PSD and trans-impedance amplification circuit is used for the laser spot detection in the re-designed sphere anemometer (Appendix B). Consequently, the laser output power is adjusted to a similar value of about 250 μW by means of a metallic resistor (R_{VR} =180 kΩ ($\pm$ 1%)) directly soldered to the pins of the laser diode.

6.2   Sensor Calibration

The 2nd generation sphere anemometer is calibrated in the acoustic wind tunnel of the University of Oldenburg (Sec. 5.2.1). It was therefor mounted in the center of a motor driven turntable with its centerline being in a downstream distance of 35 cm from the wind tunnel nozzle. The height of the motor-driven turntable has been reduced by 20 cm due to the increased size of the sphere anemometer housing. This ensures the active part of the sensor, i.e. the bending tube-sphere-element, to be placed in the center region of the wind tunnel cross-section as displayed in Figure 6.2. The sphere anemometer data is recorded by means of a 16 Bit Data Translation DT9816-A analog-digital (AD) converter, which is connected to a measurement computer via USB. Ten seconds of the four sphere anemometer channels are simultaneously acquired at a sampling rate f_s = 1kHz for each wind speed and converted to (x, y)-coordinates of the laser displacement according to Equation (3.9) during post-processing.

6.2.1   1D Calibration Function

A one-dimensional calibration function for the 2nd generation sphere anemometer is measured for reference wind speeds between 1 m/s and 20 m/s. All reference wind speeds are read from the wind tunnel display, since the calibration is intended for qualitative assessment only. The main flow direction coincides with the x-axis of the 2D-PSD in this setup.
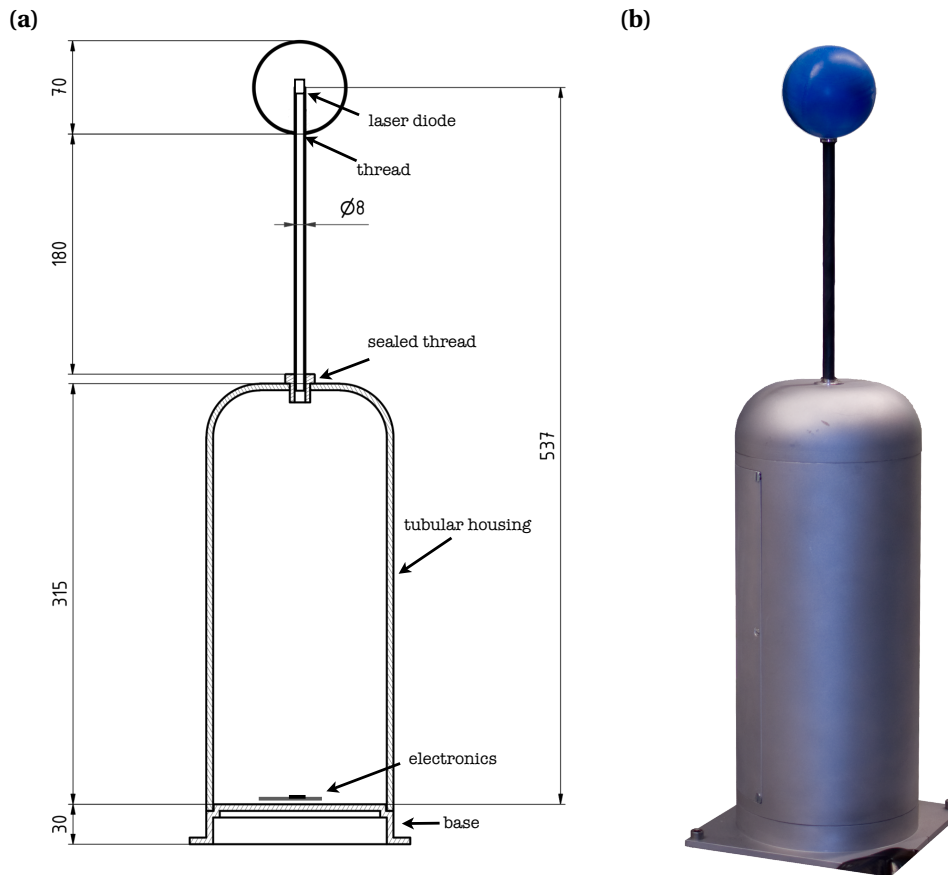
Figure 6.1: (a) Drawing and (b) photo of the 2nd generation sphere anemometer with stain-
less steel tube and smooth sphere. The helically wound supply cables are covered with a
shrinking hose.

The measured signals $U_1 \ldots U_4$ of the 2D-PSD are converted to (x, y)-coordinates. The
reference wind speed u is plotted against both components in Figure 6.3 (a), where
the "inverted power law" behavior of the x-component can be seen. Figure 6.3 (b)
shows u^2 plotted against both signal components. A linear dependence is observed
for the x-component, which is fitted with a linear regression function, while the y-
component remains almost constant. This is expected due to the alignment of the
2D-PSD's x-axis in main flow direction. As a result of one outlier at 2 m/s, the coef-
ficient of determination of the linear regression for the x-component is $R^2 = 0.9988$,
which slightly reduced compared to the value for the 1st generation sphere anemo-
meter (Fig. 5.7, p. 42). Masking the value for 3 m/s in the linear regression improves
the quality of the fit to a value of $R^2 = 0.9997$. However, R^2 must not be taken as the
only indicator for the quality of the calibration function, since it only quantifies the
deviation from the perfect square-root shape.

The complex one-dimensional calibration function for the sphere anemometer
at $\Phi = 0°$ is shown in Figure 6.4. The previously mentioned outlier at 2 m/s is still
present in this representation and has hence been masked for the calculation of the
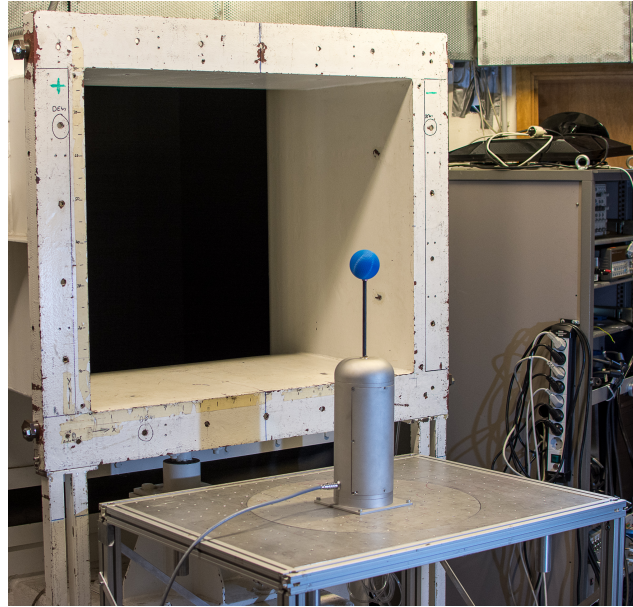
Figure 6.2: Photo of the 2$^{\text{nd}}$ generation sphere anemometer mounted on the motor-driven turntable in the wind tunnel for the two-dimensional calibration.

fit parameters. The fitted power-law function (Eq. (4.3)) in Figure 6.4 matches all non-masked data points quite well. As expected from the value of R^2 for the linear fit of the x-component, the fit exponent $n = 0.48$ of the power law deviates marginally from the theory ($n = 0.5$).

6.2.2 2D Calibration Function

The two-dimensional calibration of the sphere anemometer is performed analogously to the procedure described in Section 5.2.4 for the previous anemometer setup. Reference wind speeds are varied in the range of 0 to 17 m/s for inflow angles Φ between 0° and 350°. For angle increments of $\Delta\Phi = 10°$, ten seconds of the four sensor channels are recorded at $f_s = 1$ kHz for each combination of reference wind u speed and inflow angle Φ. A three-dimensional plot of reference wind speed u against the x- and y-component of the laser displacement on the active area of the 2D-PSD is shown in Figure 6.5 (a). The 3D plot exhibits the expected shape of a potential well with a smooth alignment of the data points without any kinks or gaps. This is more obvious in the plotted projection of the wind speed on the detector area shown in Figure 6.5 (b). The same color-coding is used for the reference wind speed in both representations of the 2D calibration.

While the 2D calibration function of the 1$^{\text{st}}$ generation sphere anemometer, presented in Section 5.2.4, was affected by the structural anisotropies of the used tube material resulting in varying displacement magnitudes, the 2$^{\text{nd}}$ generation of the anemometer exhibits a 2D calibration with a fair degree of isotropy. This is particularly evident in Figure 6.5 (b), where the data points for one given reference wind speed u

(a)

(b)
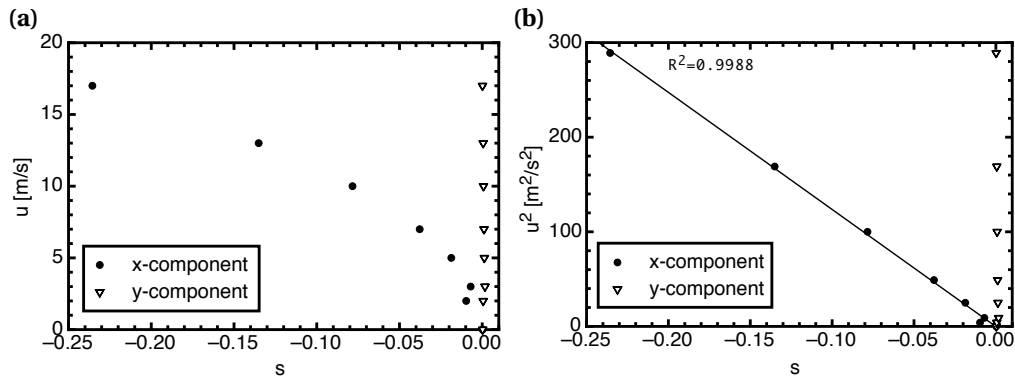
Figure 6.3: One-dimensional calibration function of the 2$^{\text{nd}}$ generation sphere anemometer recorded for 0° inflow angle. (a) The x-component (solid bullets) follows a negative power law function while the y-component (open triangles) remains unchanged with increasing reference wind speed u. (b) Square of reference wind speed, u^2, plotted against the anemometer's x- and y-signals. A linear regression line is fitted to the data for the x-component with a coefficient of determination $R^2 = 0.9988$.
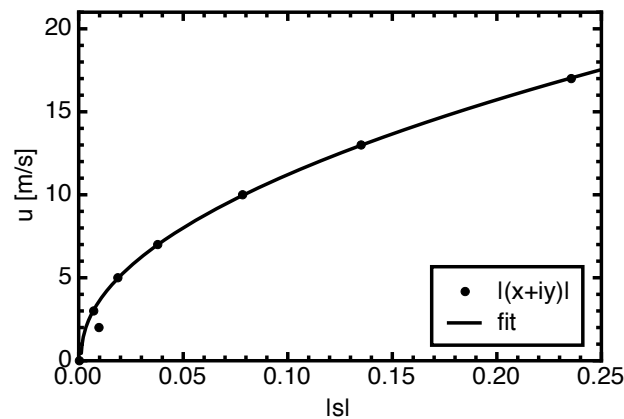
Figure 6.4: Complex one-dimensional calibration function of the 2$^{\text{nd}}$ generation sphere anemometer. The wind speed u is plotted against the complex magnitude $|s|$ of the displacement signal (points) for 0° inflow angle and is fitted with a power law function (line)

are aligned on an almost perfect circle throughout the entire range of measured wind speeds. The wind speed range of 5–10 m/s represented by the red and pink areas of Figure 6.5 (b) is particularly noteworthy, since this wind speed range was strongly affected by the structural anisotropies in the previous anemometer setup. The redesigned 2$^{\text{nd}}$ generation sphere anemometer is clearly improved in this range as no significant deviations from the circular shape of the 2D calibration are found.

A further analysis is based on the characterization of the previous setup in Section 5.2.3. The angular variation of the displacement magnitude $|s|(u, \Phi)$ for each given reference wind speed u and inflow angle Φ is compared to the angular average of the respective displacements $\overline{|s_\Phi|(u)}$. The plotted angular deviations in Figure 6.6 pinpoint the improvement of the 2D calibration of the anemometer setup.

(a)

(b)
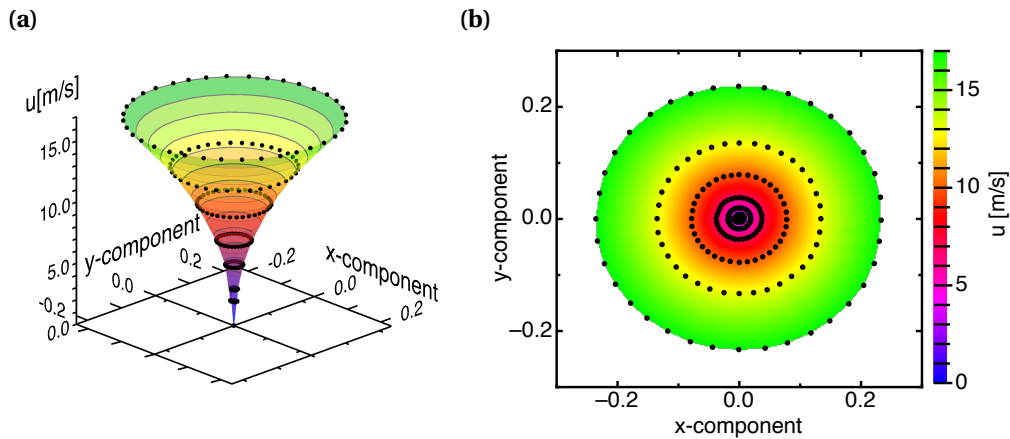
Figure 6.5: Two-dimensional calibration function of the 2nd generation sphere anemometer. The reference wind speed u is plotted against the $x-$ and y-components of the laser displacement on the 2D-PSD in (a) a 3D plot and (b) the projection on the detector area. Both plots use the same color-coding.

Table 6.1: Deviations χ of the displacement magnitude from the angular averaged displacement for a given reference wind speed u according to Eq. (5.4).

<div align="center">

2nd generation sphere anemometer

u [m/s]	5	7	10	13	17
χ_{max} [%]	+6.4	+2.8	+1.5	+1.1	+0.9
χ_{min} [%]	-6.4	-2.9	-1.6	-1.4	-1.5

</div>

The maximum of the relative angular deviation χ, defined in Equation (5.4), is listed in Table 6.1 for each wind speed beyond 3 m/s. The largest deviations from the ideal shape are found for 5 m/s reference wind speed as the displacements vary by ±6.4%. However, this is a significant improvement over the ∼ 20% deviations observed in the previous anemometer setup for this reference wind speed. In fact, the deviations at 5 m/s are smaller than the observed deviations for any wind speed in the previous anemometer setup with GFP tube. As expected, χ decreases for higher wind speeds to values below ±3% for all other considered wind speeds measured with the 2nd generation sphere anemometer setup. This improvement of the anemometer's 2D calibration and the transition towards the more isotropic stainless steel tube thus constitutes a significant optimization of the sphere anemometer setup.

Furthermore, the set and measured inflow angles, Φ_{set} and Φ_{measured}, are compared for all considered reference wind speeds. The difference $\Phi_{\text{measured}} - \Phi_{\text{set}}$ is therefore plotted against the measured angle Φ_{measured} in Figure 6.7. Maximal deviations of the inflow angle measurements are below 5° for all wind speeds with the highest deviations occurring at 5 m/s. The measured data shows no clusters and gaps as found in the previous setups, but the points are rather evenly spaced. Both findings
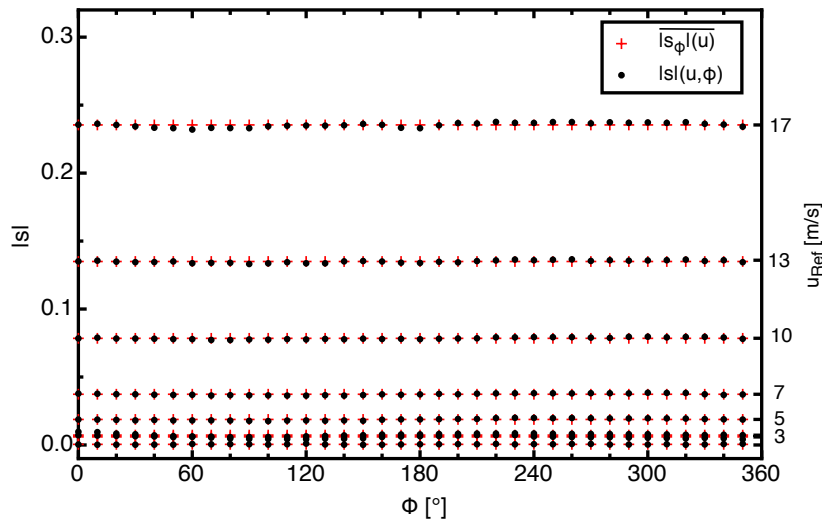
Figure 6.6: Dependency of the deflection magnitude $|s|$ on the inflow angle Φ for the 2$^{\text{nd}}$ generation sphere anemometer. The complex magnitude $|s|(u,\Phi)$ (black) deviates from the angular mean $\overline{|s_\Phi|(u)}$ (red) by less than 3% for wind speeds above 5 m/s.

match well with the expectations of an isotropic displacement of the laser spot. This is further evidence for the greatly improved symmetry of the 2D calibration function obtained for the 2$^{\text{nd}}$ generation sphere anemometer.

6.3   Temporal Resolution & Natural Frequency

A similar approach as presented in Section 5.4 is used to characterize the temporal resolution of the 2$^{\text{nd}}$ generation sphere anemometer by means of its natural frequency as the upper boundary. The anemometer is therefor placed in the wind tunnel and is subsequently exposed to three different reference wind speeds $u = 7$ m/s, $u = 13$ m/s and $u = 17$ m/s. A power spectrum is computed from each time series of laser displacement magnitudes and the resulting power spectral density is plotted against the frequency f in Figure 6.8. The expected Strouhal frequencies for those cases are $f_{u=7} = 19$ Hz, $f_{u=13} = 35$ Hz and $f_{u=17} = 46$ Hz. Only an observed peak at $f = 36$ Hz matches one of those frequencies, but it is present in all power spectra. The absence of a velocity-dependency indicates it to be a natural frequency rather than a Strouhal frequency peak according to Equation (4.4). The three peaks at $f_0 \approx 36 \pm 1$ Hz, $f_1 \approx 52 \pm 1$ Hz and $f_1' \approx 104 \pm 1$ Hz, which are found in all wind speed data sets, are the first and second natural frequency, f_0 and f_1, of the anemometer and the first harmonic $f_1' \approx 104$ Hz of the second natural frequency. The first natural frequency is marginally below the theoretically expected value of 40 Hz. This is a result of the uncertainty in the estimation of the elasticity modulus E of the stainless steel tube, Consequently, the goal of reaching a temporal resolution of about 36 Hz, which is in the order of the resolution of sonic anemometers, is achieved with the 2$^{\text{nd}}$ generation sphere anemometer.
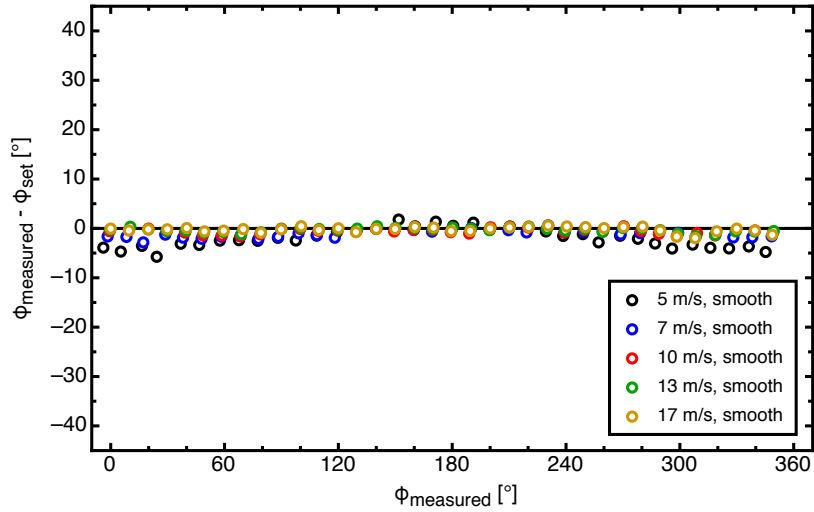
Figure 6.7: Deviation of the measured inflow angle Φ_{measured} from the set inflow angle Φ_{set} as function of measured angle for the 2$^{\mathrm{nd}}$ generation sphere anemometer setup with stainless steel tube and smooth sphere.
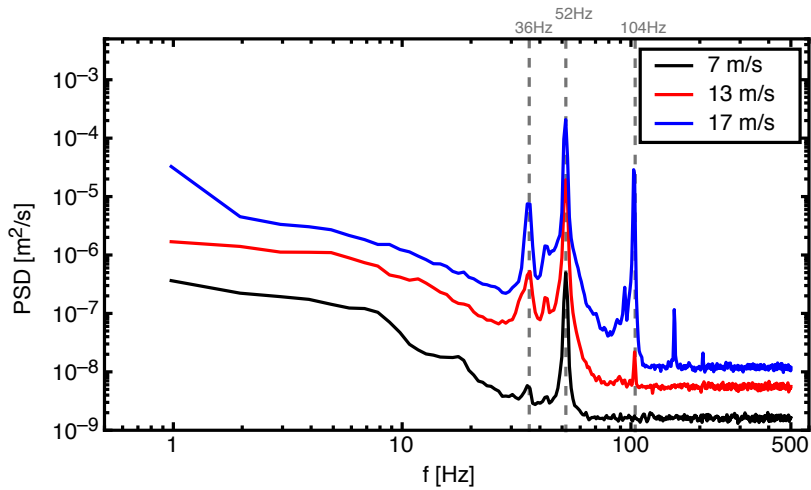
Figure 6.8: Power spectrum of the laser displacement magnitude of the 2nd generation sphere anemometer with smooth sphere for different reference wind speeds. Three peaks at the natural frequencies $f_0 \approx 36$ Hz, $f_1 \approx 52$ Hz and its first harmonic $f_1' \approx 104$ Hz are present.

6.4   Summary & Discussion

A re-design of the sphere anemometer setup was undertaken as a further step to optimize the anemometer's calibration. The problematic properties of the GFP tube were addressed by using a stainless steel tube instead. This helped solving the concerns about isotropic deflections, but in turn also implied a re-modeling of the anemometer housing in order to make up for the increased bending stiffness. A higher housing was thus constructed and equipped with a smaller tube of significantly reduced wall thickness, in order to maintain the desired measuring range. This also allowed for an improved natural frequency $f_0 = 36$ Hz of the 2nd generation sphere anemometer and makes it competitive to sonic anemometers regarding the temporal resolution. Furthermore, the improvements to the setup greatly reduced the angular dependence of the 2D calibration yielding an almost perfectly circular shape.

The optimized geometry and material parameters of the 2nd generation sphere anemometer can therefore serve as a foundation for the improvement of the anemometer towards field applications in the next development stage.

Chapter 7

The Third Generation Sphere Anemometer

Systematic investigations of the sphere anemometer properties in the previous chapters were performed to identify and resolve crucial issues related to the used sphere anemometer components. This chapter introduces the changes made to the anemometer design in order to improve its robustness and usability. The construction is enhanced towards field application, with changes made to the anemometer housing, sealing and the sensor electronics. The calibration function of the new setup is measured and its accuracy and resolution is characterized in wind tunnel experiments as well as its response to vertical wind components.

7.1 Sphere Anemometer Setup

The 3rd generation of the sphere anemometer is based on the experience from the previous version and the general choice of dimensions and materials – e.g. tube length and material, sphere diameter – is widely unaltered. However, some further optimization steps are necessary to enhance the performance under field conditions and to make the anemometer setup more refined.

Although the 2nd generation sphere anemometer exhibits many desirable features, some further optimization steps were necessary to for field applications and to improve its handling and applicability. First and foremost, the installation on met mast or wind turbines – in particular at off-shore sites – demands a higher level of watertightness, which was not accounted for so far. A reduction of the wind loading is also beneficial and consequently efforts to design a new slender housing, that can sustain the environmental condition of on- and offshore installations, is required. Besides these mechanical aspects, an effort to overhaul the sensor electronics needs to be considered. The combination of USB-powered laser and battery powered amplifier circuit is not feasible for field installations and needs to be replaced by an integrated circuit to cover both. This new sensor electronic should also output current signals of 4-20 mA to comply with signals in industrial automation as they are often required

for stand-alone data loggers.

The 3rd generation sphere anemometer features a slender aluminum housing with a dome-shaped bottom part and a tubular top part (Fig. 7.1). Its design is meant to minimize the wind load on the anemometer by reducing its diameter where the space inside the housing is not needed. Thus, the top shaft, which holds only the laser supply cables and needs to provide only space for the laser beam to pass, can be thinned, while more space is needed in the bottom part for the electronics compartment. This is realized by the larger dome-shaped cover at the bottom of the anemometer, which is wide enough to contain the sensor electronics with 2D-PSD and the laser supply circuit. Moreover, this part of the anemometer can be opened for maintenance and adjustments without the need for a disassembly of the anemometer. The blocked cross-sectional area of 308 cm^2 is reduced by 44% from 550 cm^2 of the 2nd generation sphere anemometer (Sec. 6.1). However, the overall height of the housing measured from the base of the dome-shaped electronics compartment to the top of the tubular part given in Figure 7.1 is similar to its predecessor. This is meant to maintain the desired tube size and to keep the optical amplification, i.e. the laser path, constant from the previous setup.

A thread at the top of the tubular housing allows for the fixation of the sphere-tube combination. This active part of the sphere anemometer remains almost unchanged from the previous version: A stainless steel (1.4301) tube with outer radius $R_o = 4.0$ mm and inner radius $R_i = 3.8$ mm is fitted with two threads at the top and bottom. Only the length of the support tube is slightly reduced to $l = 195 \pm 0.05$ mm, in order to increase the natural frequency of the anemometer and extend its measuring range. The top thread supports the smooth sphere of the previous setups with 70 mm diameter.

Additional sealing is included to make the anemometer withstand the challenges of heavy rain and ocean spray at near-shore and off-shore sites. A pair of rubber sealing rings is located at the transitions of the dome-cover to the tubular shaft and the base plate of the electronics compartment. Two additional rubber rings are used to seal the connection of the top thread of the shaft with the sphere-tube-combination as well as the connection of the sphere mount on the support tube (Fig. 7.1). In combination with the watertight IP67 socket at the anemometer bottom, the 3rd generation sphere anemometer setup is waterproof to the level of submergence. A mounting plate at the anemometer base allows for the fixation of the sensor on flat surfaces – it can be omitted for the installation on tubular supports. All aluminum parts of the housing are anodized to improve the surface robustness and prevent corrosion under outdoor conditions, particularly in salty offshore environments.

The tip displacement of the sphere is measured with a light pointer, as it was done in the previous setups. However, the sensor electronics is completely re-designed in order to match the demand for standardized output signals of 4–20 mA currents instead of the voltage output used so far. This aims at the use of the sphere anemometer in combination with industrial data loggers, which typically require this input range commonly used in industrial automation and control. Each anemometer channel has its own amplifier and the amplification rate can be individually adjusted via a vari-
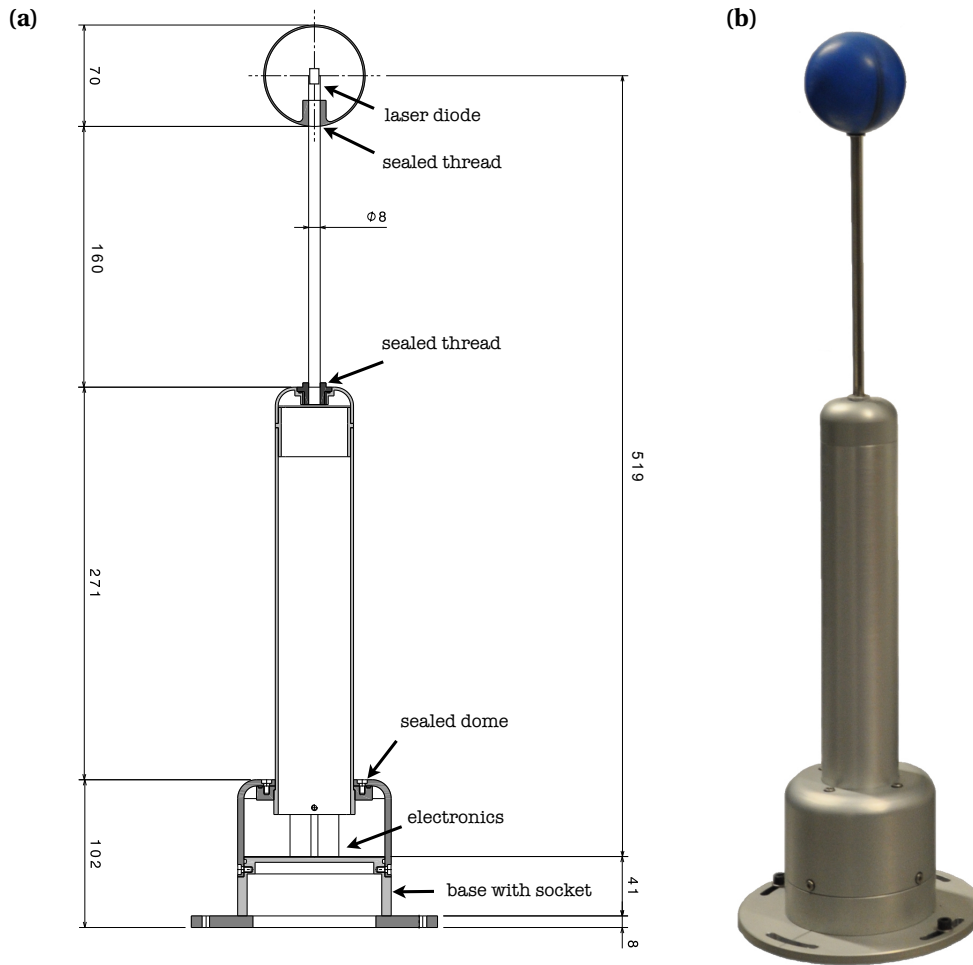
Figure 7.1: (a) Drawing and (b) photo of the 3rd generation sphere anemometer. The slender tubular housing reduces the wind loading while the optical path remains unchanged compared to the previous version. The sealed dome at the bottom holds the sensor electronics and is connected with a water-tight socket at the bottom of the base.

able resistor. The output currents I_i are linearly proportional to the induced photo currents $\hat{I}_i$

$$I_i = G_i \cdot \hat{I}_i \qquad \forall i \in [1,4] \tag{7.1}$$

with the gain factor G_i being specific for each amplifier.

As an additional improvement, the laser supply circuit with voltage regulator is integrated in the new electronics layout. A description of the plan and layout of the sphere anemometer electronics can be found in Appendix C. In all previously described anemometer setups, two power supplies were required – one for the amplification circuit and a second one for the laser supply. The new integrated design allows for the use of only one combined power supply for the sphere anemometer operation, which is connected to the mains and operated at ±12V DC output voltage.

The ADL-65055SA2 laser diode with integrated laser driver is adopted for the 3rd generation sphere anemometer as are the lens and lens holder with precision thread. As a result of the modified sensor electronics, some adjustments have to be made to the laser, though. The laser supply voltage is reduced to 3 V, which yields a reduction of the laser output power. In addition, the new amplification circuit is designed for a target laser power of 1 mW, which is about four times larger than the laser power of the previous setups. As a consequence, the resistor for the laser output regulation, which is directly soldered to the pins of the laser diode, is reduced to $R_{VR} = 6.8 \ k\Omega$ in order to compensate for this. This is well in the specified range of resistance for the laser diode, while the previous configuration was significantly off of the specified values for R_{VR}.

To adjust the gain factors G_i for the single channel amplifications, the laser diode is focused on the sensitive area of the 2D-PSD using the precision thread of the lens holder. The incident spot is subsequently aimed at each corner of the sensitive area using a micro-translation stage and the amplification of the corresponding signal channel is adjusted to match the 20 mA current by means of a variably trimmed resistor.

A further reduction of the diameter of the laser supply cables compared to the coated copper wires of the last setup is achieved by using silicon-coated single wires with a cross-section of 0.07 mm^2. These wires are not wound around the outside of the tube, but instead led through the inside of the tube. Any angular dependent effects of the cables on the exposed cross-section of the anemometer can be ruled out in this way. The added cover of the tube with a shrinking hose is also dispensable, which eliminates the risk of introducing angular dependencies of the strain behavior during the shrinking process.

To enable the usage of the sphere anemometer with common AD converters with voltage inputs, a signal conversion circuit was built. It features a precision shunt resistor with $R_S = 1.38 \ \Omega$ and a voltage amplifier with a fixed amplification rate of 200 for each of the four sphere anemometer signals. The signal conversion box is supplied by the same power supply used for the sphere anemometer.

Modifications to the Sphere Construction

The spheres used for the 3rd generation sphere anemometer are based on the 70 mm diameter hollow plastic spheres of the previous setup. However, the intent of this new anemometer generation is the operation in field conditions and different constraints regarding weathering and humidity have to be considered. Generally, the ABS plastic material which is used for the spheres is not water-tight. It has to be sealed by a covering layer of water-resistant coating. An additional impact of the environment can be safely assumed, since plastics tend to wear noticeably under exposure to ultra-violet radiation in field application. To handle both issues, the spheres are covered with several layers of spray paint, including a cover layer of UV-resistant paint. The slightly increased weight of the spheres has to be accepted as a trade-off for its indispensable

water-tightness. The combination of the coated spheres with an added rubber seal-
ing ring at the top thread of the tube makes the anemometer completely water-tight,
even when it is slightly submerged[11].

An additional environmental impact has already been foreseen regarding the dimpled
surface patterns. It is expected to be prone to dirt accretion inside the dimples, which
causes a changing drag coefficient due to the altered surface roughness. This effect is
unwanted and may lead to changes in the sphere anemometer's calibration function,
as has been pointed out in Section 5.3.1. The dimpled sphere has therefore also been
discarded for the 3rd generation sphere anemometer in order to avoid uncertainties
in the results caused by changing sphere surface properties.

First tests of the sphere-tube-connection shown in Figure 7.2 (a) revealed a weak
connection of the rather thin hollow body of the sphere and the support joint at its
bottom. A higher stiffness is required since the joint holds the aluminum thread and
is responsible for the transmission of the drag force on the tube tip. The pointy edge
connecting both parts tends to break when exposed to large forces and thus expose
the laser to the environment as seen in Figure 7.2 (b). Although these large forces
are not expected to occur during regular operation in the wind flow, the anemometer
may experience extreme forces during transport, field installation or in cases of ice
shedding from wind turbine blades. The pointy sphere joint depicted in Figure 7.2 (c)
was therefore modified with a rounded transition region to increase the stiffness and
distribute the force inlet (Fig. 7.2, d).
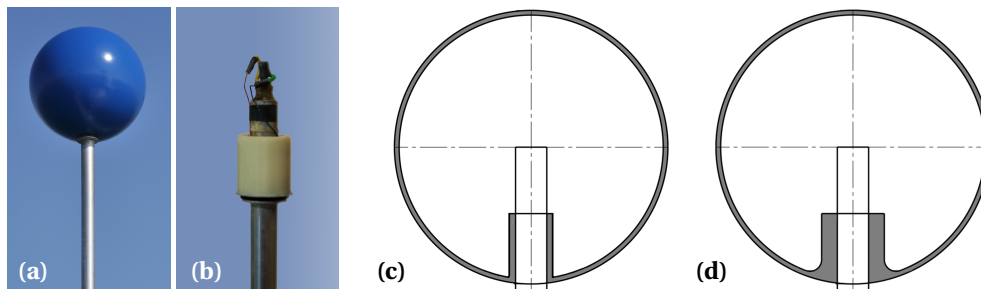
Figure 7.2: Close-up of the sphere (a) before installation and (b) the tube with remainders of
the joint after the hollow sphere broke. Drawings of (c) the old sphere with pointy joint and
(d) new sphere with rounded and stiffened joint.

7.2   Sensor Calibration

The 3nd generation sphere anemometer is calibrated in the acoustic wind tunnel of
the University of Oldenburg (Sec. 5.2.1). The calibration setup is similar to the setup
used for the 2nd generation anemometer, where the anemometer is mounted in the
center of a motor-driven turntable with its centerline being in a downstream distance

---

[11]In a simple test, the assembled anemometer with coated sphere was submerged over night without
any signs of water intrusion into the sphere or the anemometer housing.

of 0.35 m from the wind tunnel nozzle. The turntable is used in its lower configuration in order to ensure the active part of the sensor, i.e. the bending tube-sphere-element, to be placed in the center region of the wind tunnel cross-section. A photo of the setup for the calibration is shown in Figure 7.3.
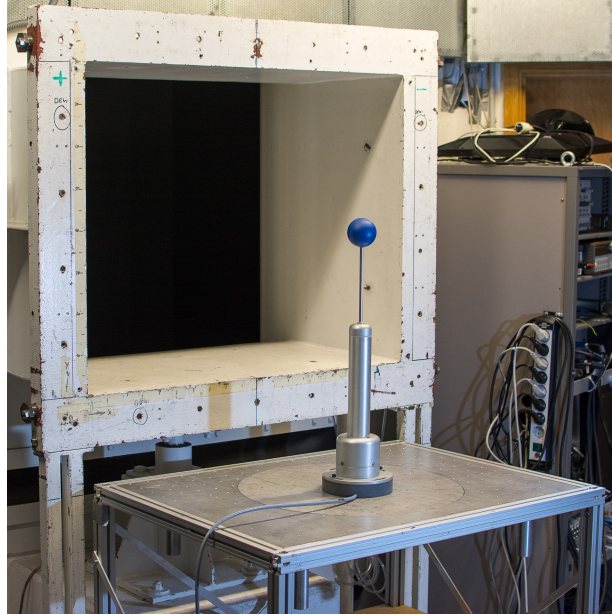
Figure 7.3: Setup for the calibration of the 3rd generation sphere anemometer.

The sphere anemometer data is recorded by means of a 16 Bit DataTranslation DT9816-A analog-digital (AD) converter with ±5V measurement range, which is connected to a computer via USB. Ten seconds of the four sphere anemometer channels are simultaneously acquired at a sampling rate of $f_s = 1$kHz and converted to (x, y)-coordinates of the laser displacement according to Equation (3.9) during post-processing. In case of the 3rd generation sphere anemometer, the calibration is not only performed for the assessment of the anemometer itself, but a later comparison to sonic and cup anemometers is also intended. It is necessary for such a comparison to base the calibration of all anemometers on the same wind speed reference. While the calibration procedure of the previous anemometers referred to the displayed wind speed of the wind tunnel panel, the one- and two-dimensional calibration of the sphere anemometer presented hereafter are based on reference wind speed measurements in the wind tunnel contraction. u_Ref is therefor measured using the eight Pitot tubes and eight static pressure taps of the wind tunnel contraction and nozzle (cf. Sec. 5.2.1). Each set of pressure probes is integrated via common tubings and connected to a calibrated Setra C239 differential pressure gauge [Setra Systems Inc., 2013]. Differential pressures p_d are converted to wind speeds during post-processing using Equation (2.3). The air density ϱ is therefor calculated from the ambient pressure and temperature readings of a combined meteorological sensor in the wind tunnel according to Equations (2.5) and (2.6) as described in Section 2.1.1.
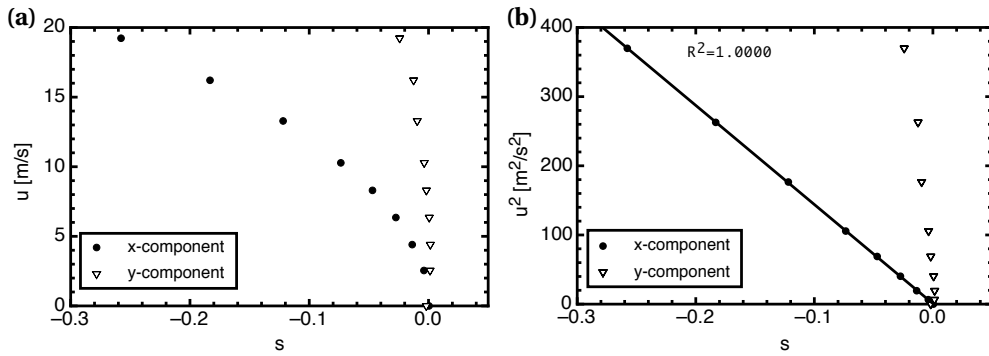
Figure 7.4: One-dimensional calibration function of the sphere anemometer recorded for 0°
inflow angle. (a) The x-component (solid bullets) follows an negative square root function
while the y-component (open triangles) remains almost unchanged with increasing refer-
ence wind speed u. (b) Square of reference wind speed, u^2, plotted against the anemome-
ter's x- and y-signals. A linear regression line is fitted to the data for the x-component with
coefficient of determination $R^2 = 1.000$.

7.2.1 1D Calibration Function

A one-dimensional calibration function of the sphere anemometer is recorded with
the setup described above. The anemometer is therefore aligned in 0° position with
the x-coordinate of the 2D-PSD corresponding to the main flow direction. The ref-
erence wind speed is varied between 0 m/s and about 20 m/s and the exact value is
determined from the dynamic pressure reading. The reference wind speed is plotted
against the calculated (x, y)-coordinates of the laser spot position on the active area of
the 2D-PSD in Figure 7.4 (a). The "inversed square-root" shape of the x-component
is similar to the findings for the previous anemometers, but a visible inclination of
the y-component is also found. This is a result of a slight misalignment between the
main flow direction and the 0° position of the anemometer, which is determined by
the orientation of the 2D-PSD inside the anemometer housing. It indicates a minor
inaccuracy during soldering of the electronics or anemometer assembly, which may
result in a constant angle offset for the direction measurements without jeopardizing
the functionality of the anemometer.

The squared reference wind speeds is plotted against the components of the laser
spot displacement in Figure 7.4 (b). A linear regression function fitted to the data of
the x-component is illustrated by the straight line. No significant deviation from the
linear relation of u^2 and x is present, which results in the perfect value of the coeffi-
cient of determination $R^2 = 1.000$. The slight negative bending of the y-component in
Figure 7.4 (a) translates to a steep negative slope in the plot of the squared wind speed
(b). No variation of the y-component with wind speed is expected for the supposed
perpendicular component, but as aforementioned it indicates an angle offset. How-
ever, it constitutes no issue for the sphere anemometer calibration, since it can be
included in the 2D-calibration. An impression of the complex one-dimensional cal-
ibration can be gained from Figure 7.5. The reference wind speed is plotted against

the complex displacement magnitude $|s| = |x + i\,y|$ for the 0° orientation of the sphere anemometer. The data is fitted with a power-law function according to Equation (4.3). The exponent $n = 0.469$ varies slightly from the square-root form of $n = 0.5$, caused by the above mentioned angle offset between the 2D-PSD's y-axis and the main flow direction.
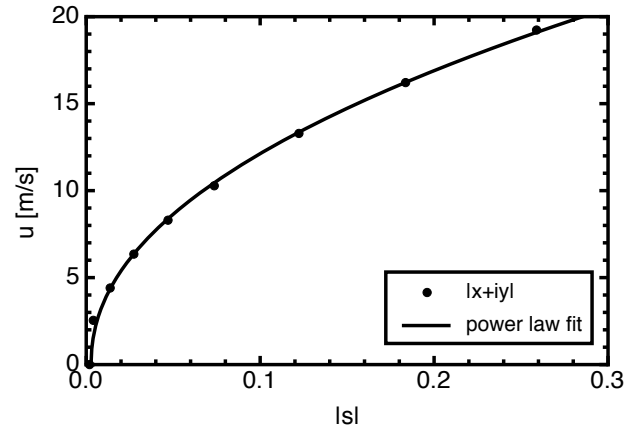
Figure 7.5: 1D calibration function of the displacement magnitude $|s|$ for the 3rd generation sphere anemometer. The data is fitted with a power law according to Eq. (4.3).

7.2.2   2D Calibration Function

The two-dimensional calibration function of the 3rd generation sphere anemometer was recorded, making use of the same setup described in the beginning of Section 7.2. The anemometer is rotated along its vertical axis on the motor-driven turntable shown in Figure 7.3. The wind speed was kept constant for each rotation of the anemometer, which comprised 36 measured inflow angles between 0° and 350° ($\Delta\Phi = 10°$). An offset measurement at $u = 0$ m/s was initially performed and the wind speed was subsequently increased up to approximately 20 m/s. The 3D plot in Figure 7.6 (a) shows the reference wind speed from the Setra C239 pressure gauge plotted against the (x, y)-coordinates of the laser spot on the active area of the 2D-PSD. The varying reference wind speeds are color coded. The 3D plot of the calibration function exhibits the shape of a potential well, which is consistent with the expectations and also found for the previous anemometers. Its projection on the detector plane is presented in Figure 7.6 (b) for a better judgment of the quality of the calibration function in terms of isotropy and uniqueness. The same color coding is therefor used in the projected display.

A unique behavior of the 2D calibration is found for the 3rd anemometer generation, as no crossings of neighboring inflow angle data can be seen. This is expected since the problems with the ambiguous anemometer behavior have been attributed to the tube material of the outdated anemometer setups, which were abandoned from the 2nd generation onwards.

(a)

(b)
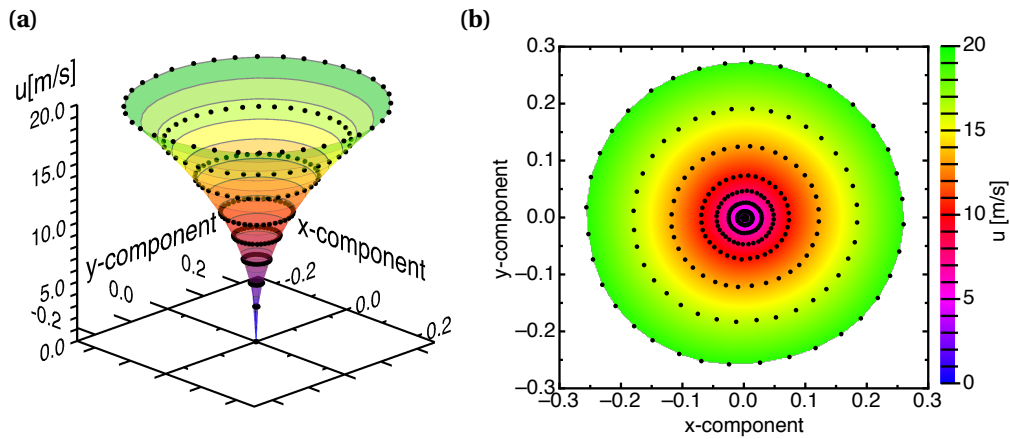
Figure 7.6: Two-dimensional calibration function of the 3rd generation sphere anemometer. The reference wind speed u is plotted against the $x-$ and y-components of the laser displacement on the 2D-PSD in (a) a 3D plot and (b) the projection on the detector area. Both plots use the same color-coding.

Table 7.1: Deviations χ of the displacement magnitude from the angular averaged displacement for a given reference wind speed u according to Eq. (5.4) for the 3rd generation sphere anemometer.

<div align="center">

3rd generation sphere anemometer

u [m/s]	5	7	9	11	14	17	20
χ_{max} [%]	+17.1	+9.3	+4.9	+2.6	+2.9	+3.4	4.0
χ_{min} [%]	-16.4	-8.3	-5.2	-4.2	-3.7	-2.9	3.0

</div>

The uniformity of the two-dimensional calibration is analyzed in terms of the relative deviation from a circular shape. As in the previous anemometer setups, the deviation χ is calculated to relate the displacement magnitude for each set inflow angle Φ and wind speed u to the angular average of it for each reference wind speed. Figure 7.7 shows the measured displacement magnitude $|s|(u, \Phi)$ plotted against the inflow angle Φ set with the turntable for wind speeds between 0 and 20 m/s. For comparison, the angular average of the displacement, $\overline{|s_\Phi|}(u)$, is also plotted as a representation of an ideal circle. Deviations from the ideal circle can be clearly observed, but the relative deviation χ is about 5% or below for wind speeds of 9 m/s or higher, as listed in Table 7.1. The positive deviations occur at the same inflow angles around $\Phi = 10°$ for all wind speeds, while the negative deviations are mainly present around $\Phi = 90°$.

The sphere anemometer data recorded during the 2D calibration procedure is used to assess the performance for direction measurements. The difference of the measured inflow angle and the inflow angle set by the turntable is therefore analyzed. Figure 7.8 shows the angle difference as a function of measured angle for all reference wind speeds, where a subscript was added to distinguish both angles $\Phi_{measured}$ and Φ_{set}. Only small differences are observed for wind speeds higher than 7 m/s, but a
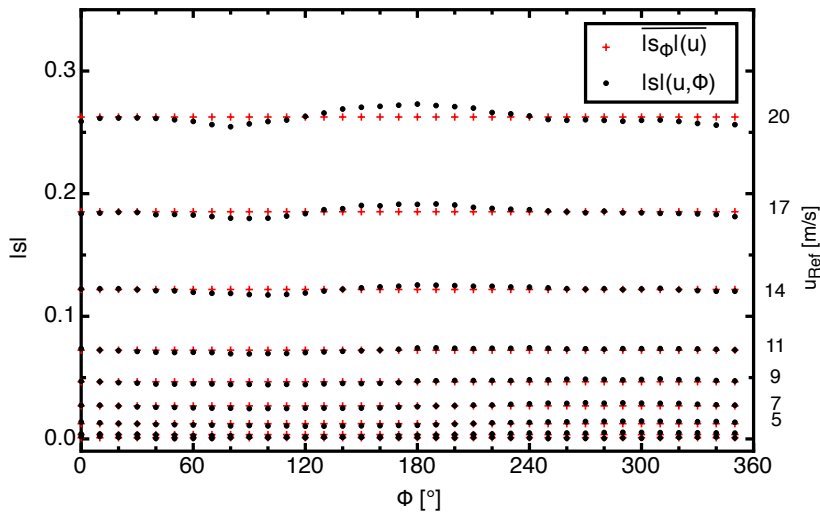
Figure 7.7: Dependency of the deflection magnitude $|s|$ on the inflow angle Φ. The complex magnitude (black) is slightly overshooting the angular mean (red) around $\Phi = 180°$ and undershooting the mean around $\Phi = 90°$.

pronounced systematic difference is obvious for 5 m/s and 7 m/s. These wind speeds are also subject to the larger deviations in terms of deviations from the circular calibration function, as listed in Table 7.1. This is only logical to manifest also in the wind direction, because the laser displacement s is used for both, the wind speed calibration and the direction calculation, in Equations (5.2). Unlike the scattering and clustering found for the 1$^{\text{st}}$ generation sphere anemometer (Sec. 5.2.4), the differences of the measured inflow angles from the set angles are continuously varying with Φ_{measured} and can therefore be fitted and corrected.
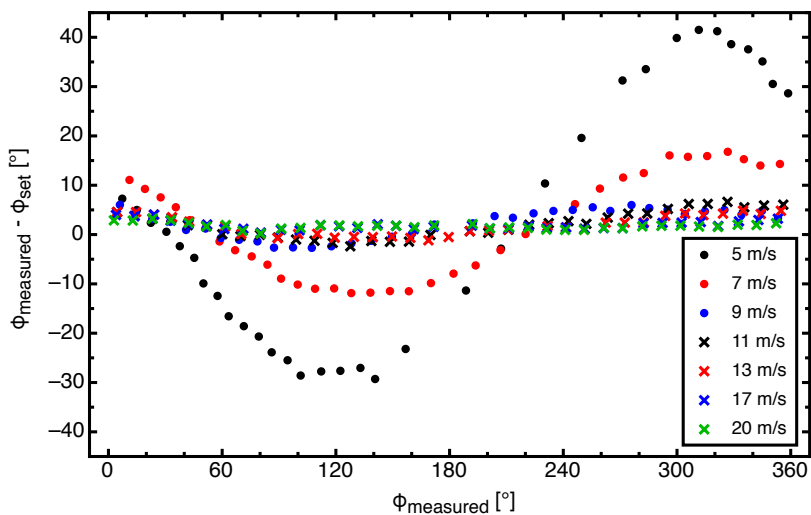
Figure 7.8: Deviation of the measured inflow angle Φ_{measured} from the set inflow Φ_{set} angle plotted against the measured inflow angle for the 3$^{\text{rd}}$ generation sphere anemometer.

A possible explanation of the slight but systematic deformation of the 2D calibration can be found in the use of individual amplification with gain factors G_i for each of the anemometer's four photo currents. The gain factors relate the actually induced photo currents $\hat{I}_1 \dots \hat{I}_4$ to the sensor outputs $I_1 \dots I_4$ linearly,

$$I_i = G_i \cdot \hat{I}_i \qquad \forall i \in [1,4]. \tag{7.2}$$

While exact identical amplification of the signals would, material effects aside, lead to a circular 2D calibration, different shapes of the 2D calibration can be achieved depending on the relation between the four gain factors $G_1 \dots G_4$. The impact of different signal amplifications is treated in more detail in the Section 7.2.3, where an exemplary calculation of a synthetic 2D calibration is presented.

7.2.3 Impact of Different Amplification Factors on the 2D Calibration

The concept of individual channel amplification is introduced for the 3rd generation sphere anemometer in order to allow for the adjustment of each signal channel to match the input range of industrial data loggers. The impact of different gain factors G_i for each of the four induced photo currents is investigated using an artificial calibration data set, which obeys a perfectly circular shape. The four channels of this data set are then distorted by multiplication with the four amplification factors $G_1 \dots G_4$ in order to mimic the individual amplification carried out in the sensor circuit of the 3rd generation sphere anemometer. Three different scenarios are therefor treated:

I. The amplification factors of each set of diagonal electrodes are different, but both factors in a diagonal are identical.

$$
\begin{aligned}
G_1 &= G_2 = 1 \\
G_3 &= G_4 \\
G_{1,2} &< G_{3,4}
\end{aligned}
\tag{7.3}
$$

II. The amplification factors of each side of electrodes are different, but both factors on a side are identical.

$$
\begin{aligned}
G_1 &= G_4 \\
G_2 &= G_3 \\
G_{1,4} &> G_{2,3}
\end{aligned}
\tag{7.4}
$$

III. The amplification factors of all electrodes are different and vary increasingly from $G_1 \dots G_4$.

$$G_1 < G_2 < G_3 < G_4 \tag{7.5}$$

The resulting calibration of case I. is deformed to become an ellipse with its semi-major axis aligned diagonally facing the electrodes with the higher amplification. The semi-minor axis is shortened, which flattens the ellipse compared to the equally amplified case of a circle, shown in Figure 7.9 (left). The different colored ellipses correspond to a 10% higher and 25% higher amplification of the original circular signal.

Case II. shows a deformation, which cannot be clearly identified with an elliptical shape anymore. An additional shift of the center of the 2D calibration is present due to the lopsided amplification, which becomes more severe for the larger difference in factors. However, this shift will be constant for a 2D calibration and not vary as long as the gain factors G_i, which are hardware settings, remain unchanged.

The individually varying case III. contains both effects as well, but they are less pronounced. The calibration may on first glance be considered elliptical, but due to the presence of different amplifications on the diagonals, a distorted ellipse is produced. The observed shift of the center is also present here. It is worth noting, that the de-
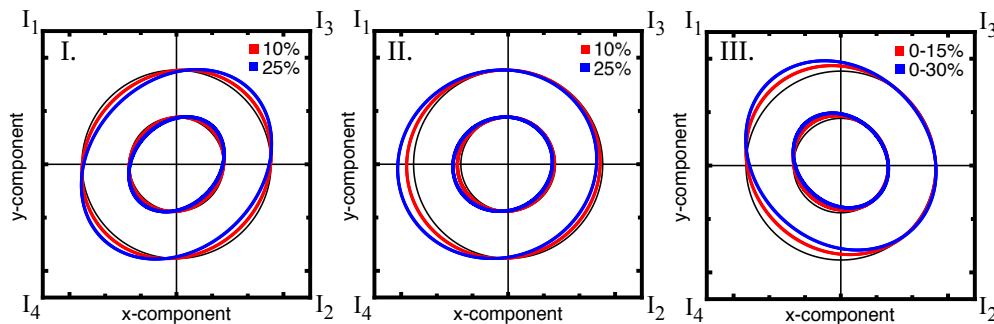
Figure 7.9: Impact of differing amplification factors of the sensor circuit demonstrated on artificial data of a perfectly circular 2D calibration (black). I. Identical amplification of the diagonal signals., II. Identical factors on each side. III. Four different factors.

scribed shift in the cases II. and III. is only observed with respect to the ideal, circular 2D calibration. By no means can be concluded, that the uniqueness of the calibration is in jeopardy due to this effect, because the shift does not change within a calibration with fixed hardware amplification factors. It is therefore automatically incorporated in a real calibration function recorded in the wind tunnel. Although these deformations found in the previous section are included in a full 2D calibration, it is desirable to achieve the highest degree of rotational symmetry in order to allow for a fast calibration procedure with only few required inflow angles. Considering the above findings, the concept of individual signal amplification should be abandoned in future anemometer setups in order not to complicate the sphere anemometer calibration. The benefit of a higher degree of rotational symmetry of the 2D calibration clearly outweighs the use of the entire measuring range of the connected AD converter or data logger. The individually adjustable amplification of the photo currents should thus be replaced by a choice of similar gain factors, i.e. similar gain resistors.

7.3   Precision and Accuracy of the Measurements

Two key features of every sensor are its precision and its accuracy, which can be defined as follows:

Precision: A measurement with a sensor is considered precise if repeated measurements of the same reference instance cause the sensor to output the same value within a certain error range. The existence of such a precise measurement, however, does not imply that the measured value is correct with respect to a "true" reference value.

Accuracy: A sensor is considered accurate if repeated measurements of the same reference instance yield sensor outputs scattered in the vicinity of the "true" reference value.

The arbitrary deviations from the reference value are attributed to the sensors precision, while the systematic deviation from the reference is considered in the accuracy. Figure 7.10 illustrates the above definitions using an ensemble of ten data points located on a target and the center of the target is considered to be the "true" reference value. Sketch (a) is an example of poor accuracy, due to the large offset of the scattered points from the center. At the same time, the large scatter between the data points shows the poor precision. An example with less scatter, i.e. good precision, but also an offset from the reference value is shown in picture (b), while the opposite case of a relatively accurate measurement with poor precision is shown in the scattered points around the center in (c). Figure 7.10 (d) show the desired case of a low amount of scatter around the "true" reference value, i.e. high precision and accuracy of the measurements.
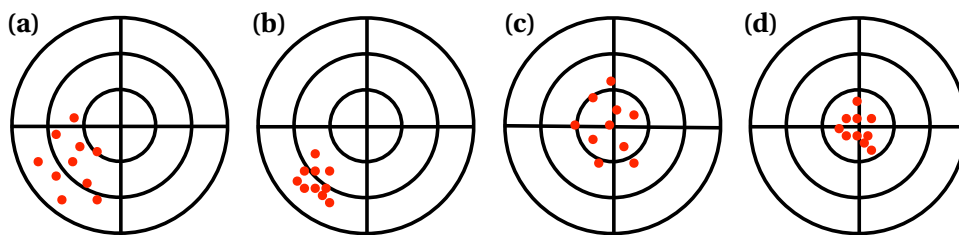
Figure 7.10: Schematic display of measurement precision and accuracy. The red data shows (a) no precision and no accuracy, (b) precision but no accuracy, (c) accuracy but no precision and (d) accuracy and precision.

These rather theoretical concept of measurement precision and accuracy translates into the question, whether the sphere anemometer measurements can be considered any of those. Two experiments were therefore carried out to assess the precision and accuracy of the sphere anemometer. Repetitive measurements of the same wind speed references u_{Ref} were performed for four different wind speeds in the range of 2.8 m/s to 11 m/s. Measurements with a reference anemometer performed at the position of the sphere anemometer provided an estimate for a confidence interval in

which the wind tunnel speed fluctuates during the regular operation.

Five instances of the anemometer reading were recorded for each reference wind speed with the anemometer being shielded from the flow in between each measurement. The wind tunnel was not switched off or set to 0 m/s between measurements to ensure the set reference wind speed to be the same for the five readings per wind speed. The precision of the sphere anemometer measurements was investigated by assessing the scatter between five subsequent readings of the same reference wind speed. The ensemble average $\langle u_{\text{Sphere}} \rangle$ of the five measured instances was therefore calculated as well as the fluctuations of the individual measurements

$$u'_{\text{Sphere}} = u_{\text{Sphere}} - \langle u_{\text{Sphere}} \rangle. \tag{7.6}$$

Figure 7.11 (a) shows the fluctuations plotted against the average value to visualize the amount of scattering of the individual measurements and the estimated wind tunnel confidence interval. The lowest velocity $\langle u_{\text{Sphere}} \rangle$ exhibits the largest fluctuations of up to 0.1 m/s while the fluctuations are significantly decreasing below 0.05 m/s with increasing reference wind speed. The confidence interval is in the same order as the fluctuations of the sphere anemometer measurements for wind speeds short below 5 m/s up to about 11 m/s. The increasing precision of the sphere anemometer readings can be easily explained by the increasing sensitivity of the anemometer setup due to the squared velocity dependence of the acting drag force. In the low wind speed range, small changes in the anemometer signal are associated with large changes in the measured wind speed due to the steep slope of the square-root calibration function, while similar changes in the higher wind speed range yield smaller differences in the measured speeds as the calibration has a lower slope. The precision for higher wind speeds can thus be expected to be similar or even better, although only wind speeds up to 11 m/s were investigated. A precision of 0.1 m/s for the investigated wind speed range is similar to the values claimed by the manufacturers of state-of-the-art anemometers, such as the Thies First Class Advanced cup anemometer [Thies Clima, 2009] or the Gill WindMaster Pro sonic anemometer [Gill Instruments Ltd., 2009].

The second key feature – the accuracy of the measurements – has been assessed in the same experiment. The reference wind speed u_{Ref} has therefore been calculated from dynamic pressure measurements with Prandtl tube connected to a calibrated Betz micro-manometer. The measured instances of the sphere anemometer wind speed u_{Sphere} were plotted against the wind speed reference in Figure 7.11 (b). Error bars indicate the standard deviation of each individual measurement of u_{Sphere}. The reference measurement is treated to be without error, besides the uncertainty considered as the wind tunnel confidence interval, which is plotted as error bars. Only minimal differences between the five data points for $u_{\text{Ref}} = 3$ m/s can be observed, while the measured values for each reference wind speed beyond that collapses. This finding is well in line with the result of the precision assessment.

In the ideal case of a perfect match of sphere anemometer and reference data, the plotted data points should be located on the line with slope 1. A slope of 1.021 is ob-
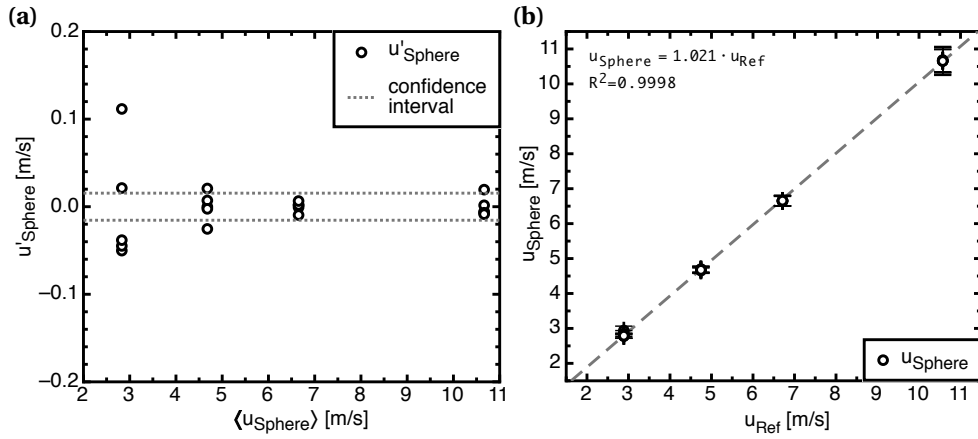
Figure 7.11: Repetitive measurements with the sphere anemometer at four different reference wind speeds. (a) The fluctuations u'_{Sphere} of the individual wind speed measurements plotted against the corresponding ensemble average $\langle u_{\text{Sphere}} \rangle$ of the sphere anemometer to assess the measurement precision. (b) Sphere anemometer wind speed u_{Sphere} plotted against reference wind speed from Prandtl tube u_{Ref} and linear fit to assess the measurement accuracy.

tained via linear regression with a coefficient of determination $R^2 = 0.9998$ as shown in the Figure 7.11 (b). This corresponds to a minimal over-prediction of the wind speed, but 2% deviation can still be considered a fair agreement with the reference and compares well to typical values of about 1% accuracy for high-end commercial anemometers.

7.4   Temporal Resolution & Natural Frequency

The frequency response of the 3rd generation sphere anemometer is assessed based on the power spectra of measured wind speed time series. The goal is the estimation of its natural frequency as an upper limit to the anemometer's temporal resolution in an analogous approach as used to characterize the previous anemometer setups.

A wind tunnel experiment is therefore performed in a setup similar to the calibration setup described in Section 7.2. The sphere anemometer with the coated smooth sphere is thereby exposed to flow with different reference wind speeds $u = 7$ m/s, $u = 13$ m/s and $u = 17$ m/s. The corresponding vortex shedding frequencies f_u according to the Strouhal number (Eq. (4.6)) are $f_{u=7} = 19$ Hz, $f_{u=13} = 35$ Hz and $f_{u=17} = 46$ Hz. Based on the theoretical considerations of Section 4.3, a natural frequency $f_0 \approx 45$ Hz is expected for the setup.

The first natural frequency of $f_0 = 45$ Hz is slightly higher than the prediction of 40 Hz, which was also observed for the 1st anemometer generation. It is close to the expected Strouhal frequency $f_{u=17} = 46$ Hz, yet it can be clearly identified as the natural frequency, because it is present in the power spectra for all wind speeds. However, the magnitude is increased for $u = 17$ m/s, possibly due to resonance with the shed-
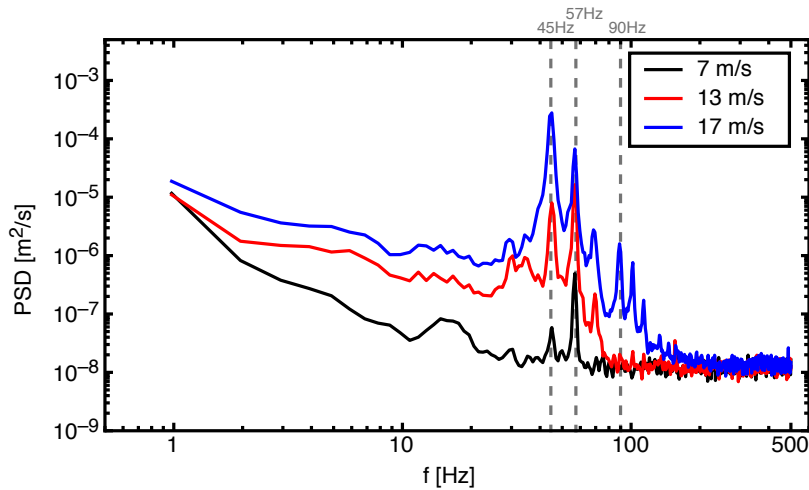
Figure 7.12: Power spectral density of the complex displacement magnitude of the 3$^{\text{rd}}$ generation sphere anemometer with smooth sphere for 7 m/s, 13 m/s and 17 m/s reference wind speeds. Two natural frequency peaks at $f_0 = 45$ Hz $f_1 = 57$ Hz are observed as well as the first harmonic $f_0' = 90$ Hz.

ding vortices. A second peak at $f_1 \approx 57$ Hz appears in all spectra, and it can thus be assumed to be a second natural frequency.

A broader peaks in the power spectra at single wind speeds are observed between 10—20 Hz for $u = 7$ m/s and around 30–35 Hz for $u = 13$ m/s. The magnitude of these peaks is small compared to the magnitude of the natural frequency peaks, and they can be attributed to vortex shedding due to their velocity dependence.

Overall, the natural frequency of about 45 Hz enables the latest sphere anemometer generation to not only compete with, but to provide a higher temporal resolution than the commercial Gill WindMaster Pro 3D sonic anemometer.

7.5   Response to Cross-Flow

Atmospheric wind conditions feature three components of the wind vector all the time, albeit the vertical wind component is usually an order of magnitude smaller than the two horizontal components. The sign of the vertical component depends on several boundary conditions like the atmospheric stability, obstacles in the vicinity and buoyancy. Although the sphere anemometer measures only the two horizontal flow components, these readings may be affected by the vertical wind component and the effect of this cross-flow is assessed in the following.

The response behavior of the sphere anemometer to cross-flow conditions is investigated using the 3$^{\text{rd}}$ generation anemometer with smooth sphere surface. For the experiments performed in the wind tunnel at the University of Oldenburg the sphere anemometer is placed on a tilting stage with the sphere located in the center of the wind tunnel cross-section in a distance of 0.35 m from the nozzle. The stage can be tilted manually between $\gamma = \pm 20°$ in steps of 2.5°. Negative tilt angles, i.e. a forward
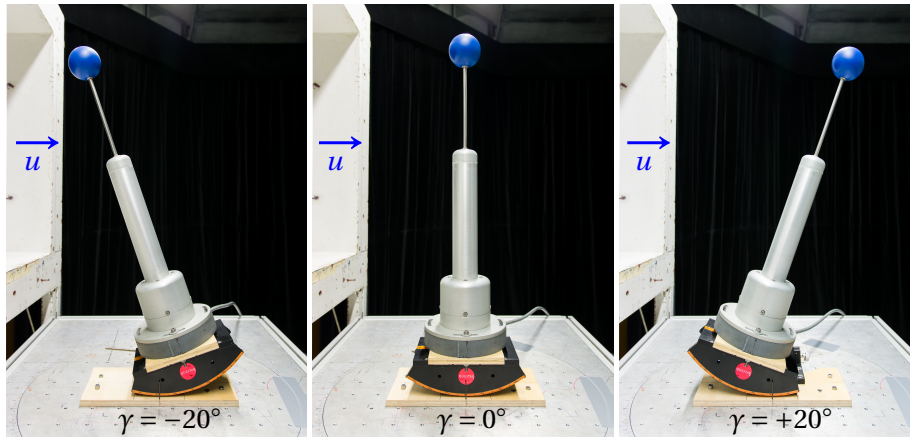
Figure 7.13: Setup for the measurement of the tilt response of the sphere anemometer. The tilt stage at the bottom of the anemometer is set to $\gamma = -20°$ (left), $\gamma = 0°$ (center) and $\gamma = +20°$ (right).

tilt, correspond to a down-wind scenario in a field measurement, while positive angles, i.e. backward tilt, correspond to an upwind scenario as can be seen in Figure 7.13. The accuracy of the set tilt angle γ is verified by means of image analysis and the deviations of less than 0.2° are considered acceptable to give a general impression of the anemometer's tilt response. The wind tunnel is set to constant horizontal reference wind speeds u_{Ref}, which is measured using the installed Pitot-tubes and pressure holes in the wind tunnel outlet connected to a calibrated Setra C239 differential pressure gauge. The sphere anemometer channels are acquired simultaneously with the same Data Translation DT9816-A AD converter used in the previous experiments, while the differential pressure, ambient temperature and atmospheric pressure are acquired with a multiplexing NI-6211 AD converter. Both AD converters sample with $f_s = 1$ kHz and cover their respective measuring range of ± 5 V and ± 10 V with 16 Bits resolution.

The experiment is intended to mimic flow situations with a vertical wind speed component as they occur in field measurements on met-masts or wind turbine nacelles. However, vertical wind components can only be achieved in the wind tunnel by tilting the anemometer, but a gravitational force component, which is not present in field installation, will inevitably be added. In order to account for this, the impact of the gravitational force F_g acting on the sphere and the tube is measured by tilting the anemometer without any wind flow. The resulting (x, y)-components and the displacement magnitude $|s| = |x + i\,y|$ of the 2D-PSD signal are calculated for each tilt angle γ. Although the main flow direction coincided with the y-component, $|s|$ is used for the assessment in order to account for slight misalignments of the detector. The displacement magnitude for the offset case is plotted in Figure 7.14 against the set tilt angle γ. A representation in terms of an equivalent wind speed u_{equiv} is given on the right ordinate in order to relate the gravitational effect on $|s|$ to a hypothetical wind

speed. Deviations from the upright anemometer position at $\gamma = 0°$ result in increased displacements $|s|$ of the laser spot due to gravitation. Only the projection of F_g on the plain perpendicular to the tube can be measured with the sphere anemometer and a sinusoidal dependence of $|s|$ is thus expected for an ideal system. The observed linear trend of the magnitude fulfills this expectation quite well as the sine function can be linearly approximated in the vicinity of 0°, and the pronounced tilt angle dependency is a clear proof of the high sensitivity of the sphere anemometer even to such small gravitational forces in the range of $F_g \approx 0\ldots0.08$ N.
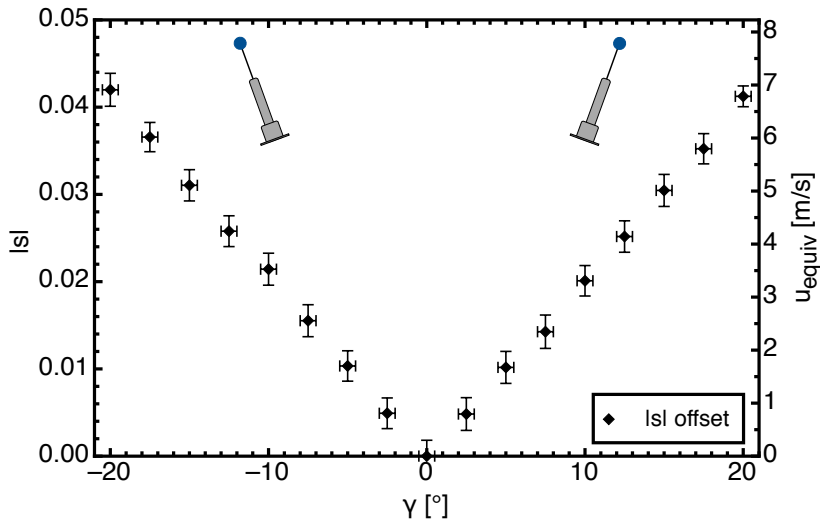
Figure 7.14: Offset signal from the sphere anemometer when it is tilted at $u_{\text{Ref}} = 0$ m/s. The displacement magnitude $|s|$ increases for positive and negative inclinations γ due to the effect of gravitation.

Two different reference wind speeds $u_{\text{Ref}} \approx 6.5$ m/s and $u_{\text{Ref}} \approx 9$ m/s are investigated to characterize the cross flow response. The sphere anemometer is tilted in both positive and negative directions from the vertical position, resulting in mimicked vertical wind components of up to ±2.2 m/s and ±3 m/s, respectively. The offset signals obtained from the previous experiment without wind flow are subtracted from the calculated displacement magnitudes $|s|$ and the offset-corrected data is calibrated using the 1D calibration function recorded prior to the experiment. Figure 7.15 shows the calibrated wind speed magnitude $|s|$ plotted against the tilt angle γ. Only the wind speed component perpendicular to the tube contributes to the sphere anemometer deflection and thus, the projected wind speed

$$u_{\text{proj}} = u_{\text{Ref}} \cdot cos(\gamma) \tag{7.7}$$

for each reference wind speed is represented with the dotted line. The two investigated cases are not differentiated in the following analysis, since the response of the sphere anemometer to the vertical flow is similar for both reference wind speeds.

For the vertical anemometer position ($\gamma = 0°$) a slightly higher wind speed is obtained with the sphere anemometer compared to the reference sensor. Slowly de-

creasing measured wind speeds u_{Sphere} are found for the upwind scenario of positive tilt angles $\gamma > 0°$. In this range, the measured wind speeds agree well with the expected projection of the respective reference wind speed u_{Ref}. On the contrary, the measured wind speeds of the sphere anemometer deviate from the projected reference for all negative tilt angles, starting at $\gamma = -2.5°$. The effects seen for negative
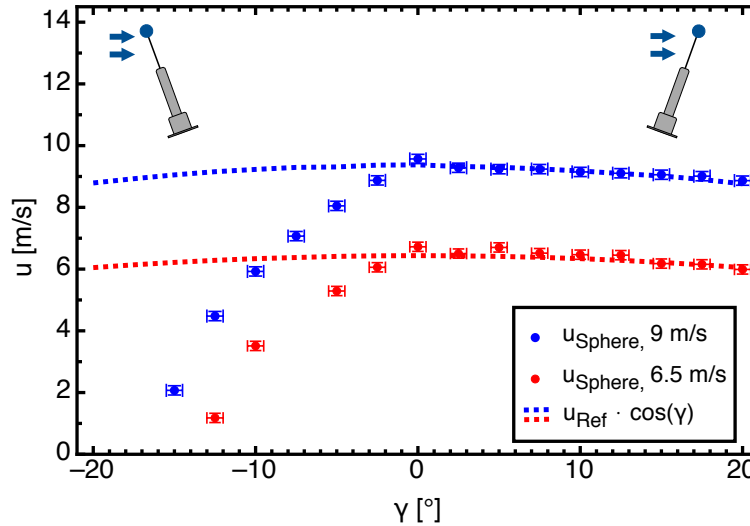
Figure 7.15: Measured wind speed u_{Sphere} of the the sphere anemometer (bullets) compared to projection of the reference wind speed u_{Ref} (dotted line). Data for $u_{\text{Ref}} = 9$ m/s is plotted in blue and data for $u_{\text{Ref}} = 6.5$ m/s are shown in red.

inclinations are unexpected, since an ideal system response would result in a symmetric cosine projection of the wind speed at $\gamma = 0°$. Nevertheless, an attempt to explain the asymmetric cross-flow response can be made based on the knowledge of the flow around a sphere with a support normal to the flow direction:

The flow around an ideal, i.e. unsupported, sphere is characterized by a front stagnation point in the center plain of the sphere and a symmetric flow around the sphere. In this case, the mean flow separation occurs symmetrically on both sides at a separation angle ϑ_s between 80° and 102° from the front stagnation point. The actual value of ϑ_s depends on the Reynolds number regime, which is affected by the sphere surface properties and background turbulence [Son et al., 2010]. The flow separation and definition of the separation angle is depicted in Figure 7.16, for a subcritical (a) and a supercritical Reynolds number (b). The separation line indicates the plain of the great circle of the symmetric flow separation on the sphere surface, which is shifted further downstream with the flow becoming supercritical. As already discussed in Section 3.2, the drag coefficient c_D decreases in the supercritical region, because a smaller fraction of the sphere surface is immersed in the sphere wake. Raithby and Eckert [1968] investigated the flow around a sphere on a support normal to the flow direction with flow visualization techniques and compared it to the flow around a sphere, which is supported from its back side as the experimental equivalent of the ideal case. They found the separation locations to be altered due to the impact of the normal support

at certain Reynolds numbers. Almost no effect of the support on the flow separation is found for the subcritical case as depicted in Figure 7.16 (c), since the flow separation at $\vartheta_s \approx 80°$ sets in upstream of the support rod. Consequently, the wake is not increased by the support and c_D remains the same as in the unsupported case. As the flow becomes supercritical (Fig. 7.16, d), the separation region moves downstream and the location of the support is in the (ideally) attached flow region. Raithby and Eckert showed by flow visualizations, that the support causes a premature separation of the flow at a different separation angle ϑ_s' in the lower hemisphere. The separation line is bent as indicated by the dashed red line and as the wake of the sphere increases compared to the ideal case (dashed line) also the drag coefficient c_D does, which they claim to be inversely proportional to the separation angle, $c_D \propto 1/\vartheta_s$.

Raithby and Eckert [1968] did not consider a tilted support of the sphere in their study. An attempt to explain the tilt response of the sphere anemometer will therefore be made by carrying their results forward in a gedanken experiment of the flow around the sphere with forward and backward tilted support, which is illustrated in Figures 7.16 (e–h).

Once the sphere is tilted forward at negative tilt angles γ, the support is moving further leewards. The separation would thus be unaffected in the subcritical regime and occur symmetrically at ϑ_s as sketched in Figure 7.16 (e). Supercritical flow occurring at high wind speeds or higher background turbulence would shift the separation location further downstream and cause the support to trigger premature separation on the lower hemisphere (Fig. 7.16, f). In this case, the wake would be extended compared to the ideal case, but presumably reduced compared to the upright support. The opposite case of positive tilt angles is treated in Figure 7.16 (g, h) for both Reynolds number regimes. Here, even in the subcritical range, a premature separation due to the support is present in the lower hemisphere and thus the wake and consequently the drag of the sphere are increased compared to the negatively tilted and upright case. This effect gets more severe for the supercritical regime in which the largest increase of the wake region will be present compared to the cases without and with upright support. A result of the premature flow separation on the lower hemisphere would be an increased drag coefficient, i.e. also an increased drag force F_D, of the sphere due to the larger wake.

Raithby and Eckert's investigations were performed on a 12.06 cm diameter sphere with a 1.27 cm support, resulting in a support-sphere-ratio of 10.5%. Although this ratio is almost identical to the support-sphere-ratio of 11.4% of the sphere anemometer, the geometry of the sphere anemometer support varies slightly from the considerations by Raithby and Eckert due to the additional thread right underneath the sphere. The prevailing Reynolds numbers $Re \approx 68,000$ and $Re \approx 95,000$ in the cross-flow experiment are well in the subcritical range and will stay subcritical up to approximately 40 m/s by design. However, the resulting tilt response resembles the above cases for a supercritical flow as the measured wind speed agrees well with the expected projection for positive tilt angles γ and the drag force F_D appears to be constant. The
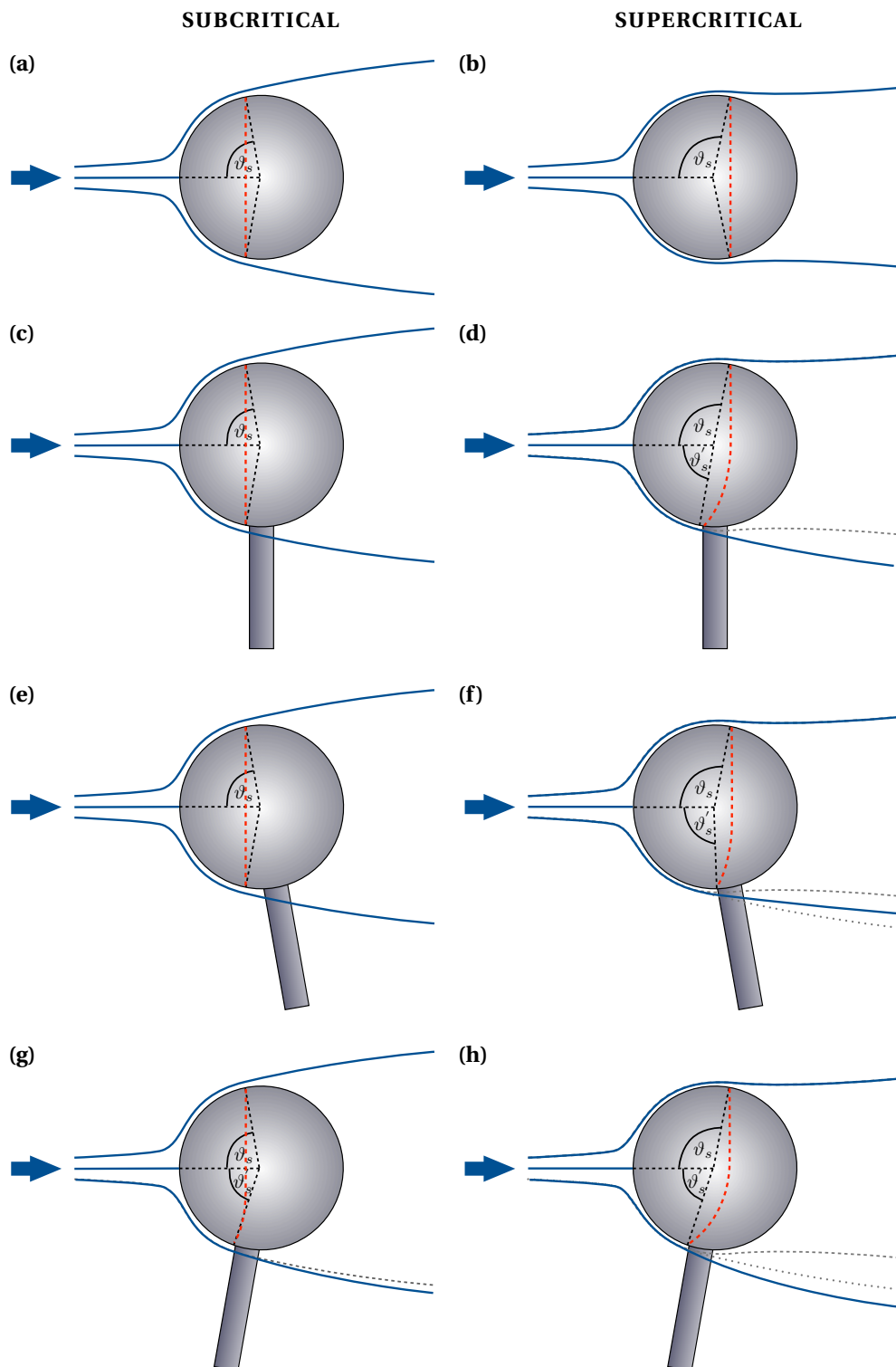
Figure 7.16: Illustration of the flow separation associated with the plain sphere (a, b) compared to the sphere on a support normal to the flow. The supported sphere is considered for both Reynolds numbers with upright support (c, d) as well as forward (e, f) and backward tilted (g, h) support. A subcritical Reynolds number is depicted in the left column and a supercritical Reynolds number in the right including the separation line (red) and the respective separation angles ϑ_s and ϑ_s'. The wakes of the unsupported (dashed) and untilted (dotted) case are marked, when different.

deviation from the expectation in the range of negative tilt angles is an indication for a reduced drag force $F_D' < F_D$ acting on the sphere. Consequently, the two cases of upright support ($\gamma = 0°$) and positive tilt ($\gamma < 0°$) of the support tube with upstream shifted tube fixation seem to impact the flow around the sphere and tube such that premature separation of the flow occurs. It can be suspected that premature separation is triggered even at $\gamma = 0°$ by the additional thread (Fig. 7.17), which increases the support-sphere-ratio and disturbs the flow further upstream. In this case, both ane-
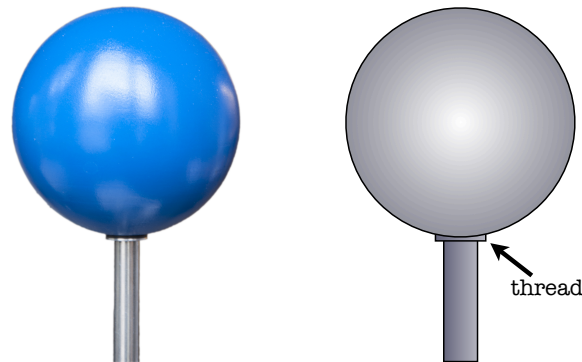
Figure 7.17: Photo and sketch of the sphere with widened support due to the thread at the bottom of the sphere.

mometer alignments cause premature separation and thus generate a drag forcing F_D, which is larger than expected without premature separation, as sketched in Figure 7.18 (a) and (b). This larger drag force is reflected in the anemometer calibration function, since it occurs already in the upright alignment used during the calibration. On the contrary, the negative tilt of the anemometer ($\gamma < 0°$) causes a downstream shift of the sphere fixation beyond the separation point of the sphere. This yields a lower drag force $F_D' < F_D$ compared to the calibration (Fig. 7.18, c), which would result in the steeper wind speed decrease found for negative tilt angles. This is however only the case, if the the upright support is already causing premature separation and an additional drag force. Further knowledge about the flow separation is required for this geometry in order to prove this hypothesis. These investigations are beyond the scope of this thesis, though.

7.6 Summary & Discussion

Based on the material choice and the setup of the previous chapter, the sphere anemometer setup was optimized toward the application in turbulent atmospheric flows. This 3rd anemometer generation features a slender housing to reduce the wind load. It is completely water-tight to withstand the environmental impacts, which are expected for the installation on wind turbines and met-masts. The sphere construction was re-designed to improve the robustness of this crucial component and, most notably, the sensor electronics was overhauled to comply with commercial data logger systems and include the power supply for the laser diode. A characterization of the
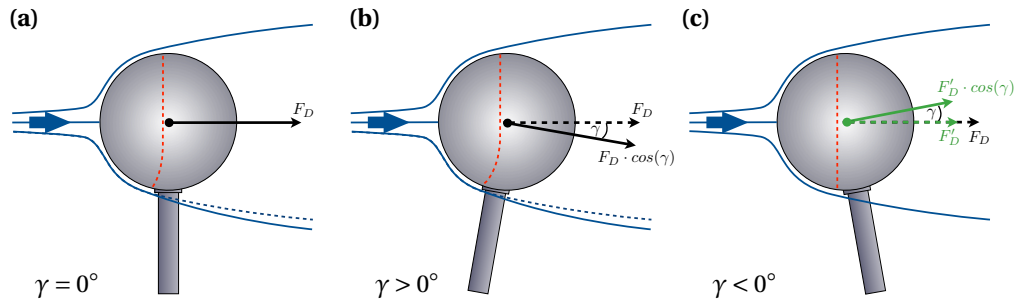
Figure 7.18: Illustration of flow separation line (red) and drag force acting on the sphere in the upright case (a) and for positive (b) and negative (c) tilt angles γ. (c) shows the reduced drag force F'_D (green) and the projection of the horizontal drag force F_D and F'_D (dashed) on the plain normal to the support (solid) is included in (b) and (c). The blue line indicates the wake for each case (solid) compared to the case without premature separation (dashed).

anemometer's 1D and 2D calibration functions was performed in a similar procedure as presented for both previous sphere anemometer development stages. Both calibration functions agreed well with the expectations, although the 2D calibration function deviated slightly from the ideal case of perfectly concentric circles. Theoretical considerations of a synthetic 2D calibration confirmed this effect to originate from the individually amplified sphere anemometer channels, which were introduced in the re-designed sensor electronics. As a consequence, the individual gain factors should be abandoned for future setups or at least the gain resistors should be set to the same value for all four channels of the 2D-PSD, in order to achieve the highest degree of rotational symmetry for the 2D calibration function and thus facilitate the sensor calibration procedure.

The 3rd sphere anemometer generation constitutes the final development stage presented in this thesis. Its properties were therefore characterized in more detail than the previous setups, assessing the precision and accuracy of the anemometer as well as its frequency response to different wind speeds in wind tunnel experiments. Both, precision and accuracy of the sphere anemometer, were found to be competitive to commercial cup and sonic anemometers, while the temporal resolution even exceeds the typical resolution of those anemometers.

Additionally, the cross flow response of the sphere anemometer was investigated. Results of the performed tilt experiments showed good agreement with the expectations for the scenario of vertical upwinds, while deviations from the expected wind speed projection were found for down-winds. An attempt to explain this behavior was made based on the occurrence of premature flow separation on the lower hemisphere for horizontal winds and upwinds, which yield higher drag forces compared to the down-wind case without premature separation.
Although this hypothesis is supported by the flow visualization experiments by Raithby and Eckert [1968], a detailed experimental investigation of the flow around the sphere

anemometer is necessary to improve the understanding of its cross flow response. The impact of turbulent inflow should also also incorporated in such investigations, since turbulence reduces the critical Reynolds number at which transition between subcritical and supercritical flow occurs. Non-intrusive measurement techniques like Laser Doppler Anemometry (LDA) and Particle Image Velocimetry (PIV) used in particular in the sphere-support region are required to fortify the knowledge of the underlying mechanisms of drag increase or reduction and would therefore be of great benefit. Results from such investigations could be used in combination with additional techniques to detect the flow separation on the sphere in order to correct for cross flow effects or even detect the vertical wind component. However, significant experimental effort is required for a detailed investigation of the boundary layer flow in the vicinity of sphere, partly because of the three-dimensional surface curvature and partly because of the common challenges of using laser-based measuring techniques close to reflecting surfaces. These investigations are beyond the scope of this work and are left for future studies.

Chapter 8

Turbulent Wind Measurements

This chapter describes the first characterization of the 3rd generation sphere anemo-meter in turbulent wind conditions. Wind tunnel experiments are presented with the sphere anemometer and two commercial anemometers for wind energy and meteo-rology applications. The measurements are analyzed regarding the wind speed and wind direction to assess the performance of the anemometers and identify their lim-itations.

8.1 Turbulent Inflow Measurements Behind the Active Grid

The sphere anemometer is designed for the operation on wind turbines and met-masts and it is therefore meant to measure turbulent atmospheric flows. Flow con-ditions in field experiments can however neither be controlled nor reproduced. To avoid the uncertainties of field sites, the performance of the sphere anemometer is first investigated under turbulent inflow conditions in the wind tunnel.

8.1.1 Experimental Setup

The measurements in the acoustic wind tunnel at the University of Oldenburg are performed using the 3rd generation sphere anemometer (Ch. 7) as well as two com-mercial sensors for atmospheric applications – the Thies First Class Advanced cup anemometer and the Gill WindMaster Pro 3D sonic anemometer (Sec. 2.2 & 2.3). A reference measurement to compare all three anemometers to is conducted with a single wire hot-wire probe connected to a Dantec Dynamics Streamline frame and operated with Dantec's Streamware software. The hot-wire probe is calibrated with a Dantec Dynamics Flow Unit calibrator.

Turbulent inflow is generated by means of an active grid, which was developed at the University of Oldenburg. The active grid consists of 16 shafts with attached squared flaps with a diagonal of 0.105 m [Knebel et al., 2011; Weitemeyer et al., 2013]. Each of the nine vertical and seven horizontal shafts can be individually rotated by a stepper motor in a customized way at 900°/s maximum angular velocity. The move-ment pattern, called grid protocol, is controlled by a LabVIEW software such that the
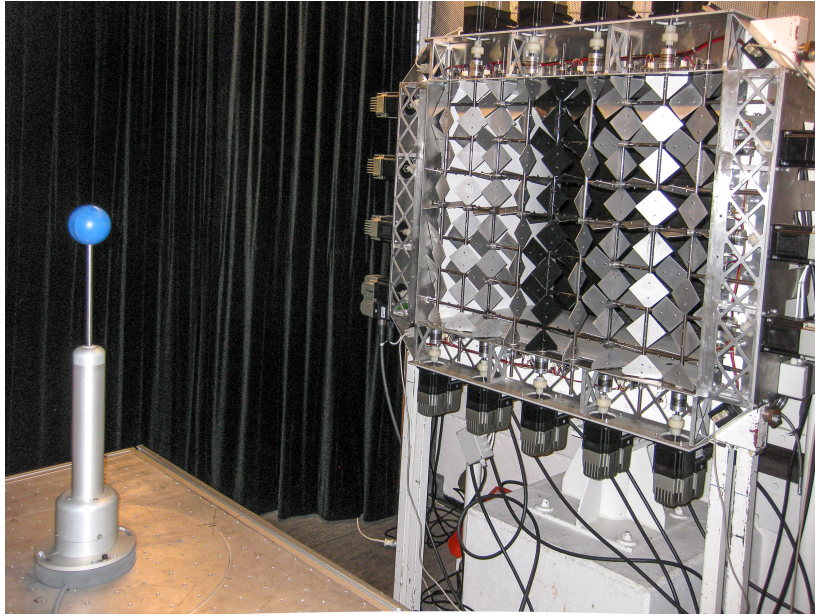
Figure 8.1: Photo of the sphere anemometer placed 1.35 m downstream of the active grid on the wind tunnel center line.

total blockage of the wind tunnel cross-section remains constant. The grid protocol can be repeated to reproduce the same flow pattern at a certain downstream position [Wächter et al., 2012] and even customized patterns from field measurements can be mimicked in the wind tunnel [Reinke et al., 2017]. The grid protocol for the comparison of the sphere anemometer to the other anemometers generates a 30 minute pattern of artificial turbulent fluctuations in the center region of the active grid wake.

For the investigations of the anemometers, all sensors are subsequently placed in a downstream distance of 1.35 m from the active grid, with the center of their respective measuring volume (i.e. sphere center, rotor center or crossing point of sound paths) located on the wind tunnel center line as shown in Figure 8.1. The Gill Wind-Master Pro 3D sonic anemometer features two significantly different orientations: the northern orientation (0°) with the support upstream of the measuring volume and the southern orientation (180°) with free inflow into the measuring volume. To cover possible differences, both orientations are measured with the sonic anemometer. Although the sonic anemometer is principally capable of measuring the 3D wind speed vector, only the 2D contribution to the horizontal wind speed magnitude and direction is considered in this experiment.

8.1.2   Data Acquisition & Processing

The analogue output signals of the sphere anemometer, sonic anemometer and cup anemometer are acquired during subsequent runs of the grid protocol by using the DT9816-A AD converter at a sampling rate $f_s = 1$ kHz per channel, while a sampling rate of $f_s = 10$ kHz is used for the higher resolving hot-wire reference. The raw voltage

data for the subsequently acquired measurements is calibrated with the respective sensor calibration functions recorded prior to the measurements. Since no triggering system is available to synchronize the active grid movement with the start of the measurements, signals are shifted during post-processing to allow for a time series comparison. In order to find the correct time shift between the signals of hot-wire, sonic, sphere and cup anemometer, the cross-correlation coefficient

$$CCF(\tau) = \sum_{i=1}^{N} a_1(i) \cdot a_2^*(i + \tau) \tag{8.1}$$

is calculated for different time lags τ between the hot-wire reference a_1 and the recorded data from each atmospheric anemometer a_2. Here $(\cdot)^*$ denotes the complex conjugate of the quantity. An excerpt of 29 minutes is extracted from each data set, starting at the determined time shift of the respective signal. All subsequent analyses are carried out based on this cut time series of equal length and common starting pattern.

While the hot-wire is capable of measuring at 10 kHz temporal resolution, the 1 kHz sampling of the atmospheric anemometers constitutes already a significantly over-sampling of the data. The hot-wire data is therefore down-sampled to 1 kHz by means of block-wise averaging for the spectral comparison presented in the following. As a consequence of the limited temporal resolution of the three atmospheric sensors, further down-sampling of all measured time-series was performed. Although all anemometers provide significantly different temporal resolutions, the data has been down-sampled to 50 Hz for all of them in order to allow for a comparison of mean values $\overline{u}$, standard deviations σ_u and turbulence intensity

$$I_u = \frac{\sigma_u}{\overline{u}} \tag{8.2}$$

without effects of different sample size and resolution.

8.2   Comparison of the Horizontal Wind Speed Measurements

The described experiment is performed for two different reference wind speeds – one at a rather low speed of approximately 8 m/s and one at about 20 m/s. While the comparison of the data for both wind speeds yields similar tendencies, some differences in the results are present.

Figure 8.2 shows an excerpt of 60 seconds of the horizontal wind speed measurements with cup, sonic and sphere anemometer at the lower reference wind speed of approximately 8 m/s. The plotted time series are complemented by the recorded time series of the hot-wire reference anemometer. All three anemometers are qualitatively capable of following the general structure of the gusts produced with the active grid. The cup anemometer measurements in Figure 8.2 (a) over-estimates the wind speed in most cases for the sudden gusts with strong negative wind speed gradient. This can be clearly identified throughout the entire 60 s excerpt, but is particularly evident for

the pronounced dips in the wind speed between 15 s and 20 s. In contrast to the cup anemometer, the sonic anemometer is following the strong gusts reasonably well. No significant difference between the 0° orientation (Fig. 8.2, b) and the 180° orientation (Fig. 8.2, c) of the sonic anemometer is found. Similar to the sonic anemometer, the sphere anemometer (Fig. 8.2, d) is also capable of resolving the imposed gusts. The time series appears to be shifted towards higher wind speeds compared to the hot-wire, though.
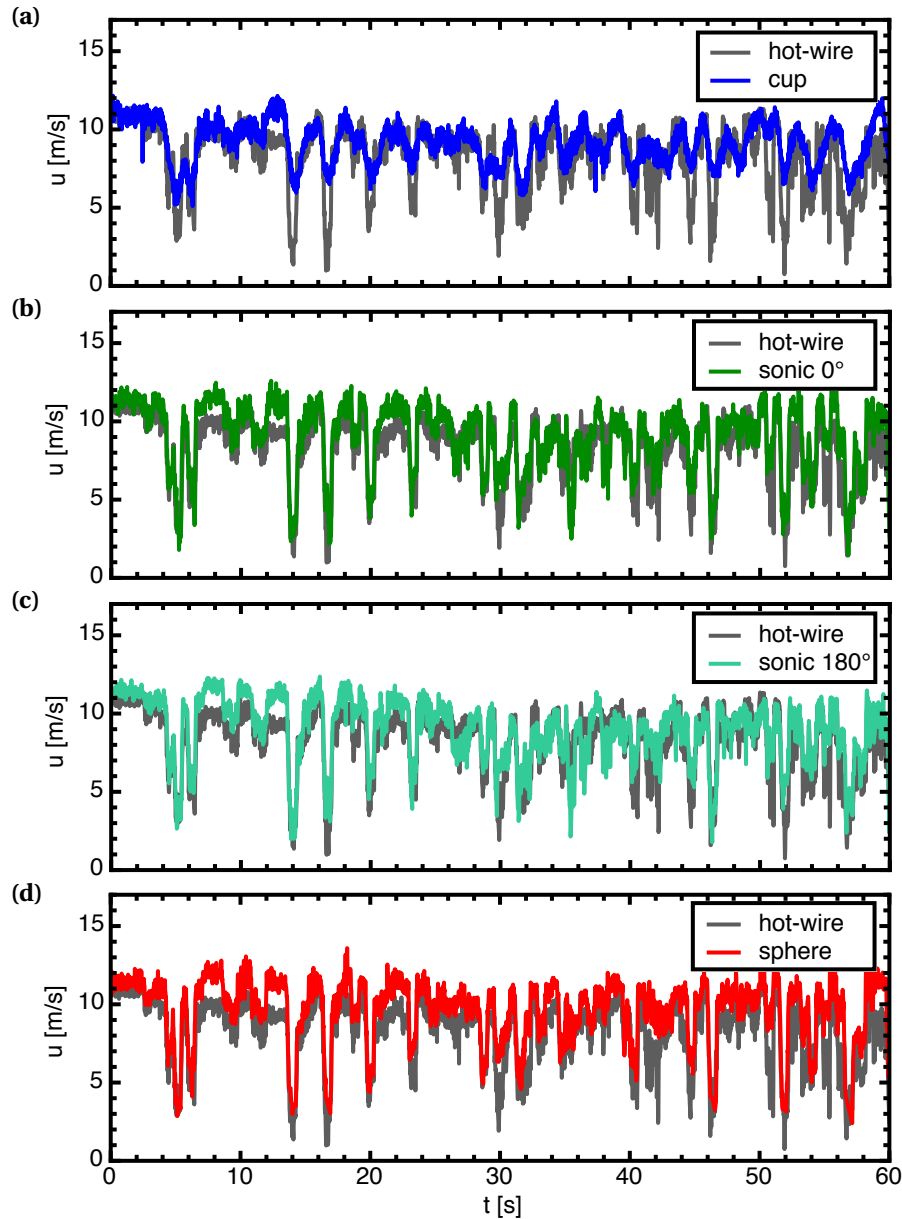

Figure 8.2: Excerpts of the first 60 seconds of the down-sampled time series measured behind the active grid at $\overline{u} \approx 8$ m/s. The hot-wire reference (gray) is compared to (a) cup anemometer, (b) sonic anemometer in 0° orientation and (c) in 180° orientation as well as (d) sphere anemometer.

The mean values $\overline{u}$ of the recorded wind speed of all anemometers a listed in Table 8.1, along with the standard deviation σ_u and the resulting turbulence intensity I_u. The mean values of the wind direction, $\overline{\Phi}$ and its standard deviation σ_Φ are also listed for completeness, although the wind direction comparison is treated later in Section 8.3.

The impression of the time series excerpts is confirmed by the evaluation of the mean values, as all atmospheric anemometers over-estimate the horizontal wind speed compared to the hot-wire reference, which is particularly evident for the sphere anemometer. While a general tendency to measure higher wind speeds for these anemometers can be attributed to the larger spatial extent of the sensor being exposed to a non-uniform flow, the deviation of the cup anemometer found for the strong negative gusts may hardly be attributed to this. Instead it is caused by the high inertia of the cup anemometer as a rotating system compared to the more responsive sphere anemometer with very low inertia and the sonic anemometer, which both resolve the gusts well. The cup anemometer is significantly less responsive to the underlying turbulence in the flow. This results in a lower standard deviation σ_u and consequently yields also a lower measured turbulence intensity I_u. While the sonic anemometer in 0° orientation is matching the turbulence intensity of the hot-wire well, it is slightly below it in 180° orientation. This is similarly observed for the sphere anemometer, which measures also a higher mean wind speed $\overline{u}$. As pointed out before for the mean wind speed, the deviation of I_u from the hot-wire reference is caused by the significantly different measurement volumes of the atmospheric sensors.

It is striking, that the sonic anemometer measures a higher turbulence intensity in its 0° orientation with support upstream of the measuring volume than in the 180° orientation with free inflow. I_u agrees well for the undisturbed 180° orientation of the sonic anemometer and the sphere anemometer.

Table 8.1: Mean value $\overline{u}$ and standard deviation σ_u of the horizontal wind speed as well as turbulence intensity I_u measured with the four different anemometers in turbulent flow with approx. 8 m/s reference wind speed. The mean wind direction $\overline{\Phi}$ and its standard deviation σ_Φ a listed for sonic and sphere anemometer.

	$\overline{u}$ [m/s]	σ_u [m/s]	I_u [%]	$\overline{\Phi}$ [°]	σ_Φ [°]
hot-wire	7.8	1.8	23	–	–
cup	8.8	1.4	16	–	–
sonic 0°	8.8	2.0	23	181.2	5.9
sonic 180°	8.6	1.7	20	181.6	5.9
sphere	9.6	1.8	19	180.6	12.6

An excerpt of the first 60 seconds of the horizontal wind speed u measured with hot-wire, cup, sonic and sphere anemometer at about 20 m/s wind speed is shown in Figure 8.3. Each plot contains the hot-wire reference measurements for compar-

ison with the respective atmospheric anemometer. Given the deviations apparent in the lower wind speed measurements, the cup anemometer shows some surprisingly good agreement with the hot-wire data for the first couple of seconds including some strong gusts (Fig. 8.3, a). As time evolves past 20 seconds, however, the deviations from the reference measurements increase notably towards the end of the 60 second excerpt. One possible reason for this behavior of the cup anemometer may be a spatially extended flow pattern, which hits a larger part of the cup anemometer rotor and is not resolved by the smaller hot-wire probe. One could argue, that a pattern like this would be present in the measurements of the other two sensors, which are also affected by larger structures due to their extended measuring volumes. Neither the sonic anemometer in any orientation (Fig. 8.3, b & c) nor the sphere anemometer (Fig. 8.3, d) exhibit a similar wind speed drop with comparable deviations, although the measuring volumes of the anemometers are comparable. Spatial variations in the flow cannot be ruled out entirely to cause the cup anemometer deviation, since the part of the wind tunnel cross-section covered by each of the anemometers is slightly different and each anemometer may be affected in a different way. However, a more likely explanation for the cup anemometer deviation is the inertia of the rotor, which prevents the cup anemometer from reaching the "equilibrium state" for the wind speed in time before a following gust hits the anemometer and thus causes a lock-in on a lower wind speed.

The sonic anemometer measurements in both orientations match reasonably well with the hot-wire reference, albeit some of the gusts are not fully covered by the anemometer. Since the sonic anemometer has no inertia, the reason for these rather small deviations are either the spatial extent of the flow structure or a bias due to the internal signal processing and averaging procedure. This cannot be distinguished from the conducted experiment.

Good consistency between the hot-wire reference measurement and the sphere anemometer wind speed is found for this comparison in Figure 8.3 (d). The overall qualitative agreement seems to be significantly better than found for the reference anemometer and cup anemometer, while a similar level of agreement with the sonic data can be concluded. Some of the gusts are not entirely covered by the sphere anemometer, but the results are matching the data obtained with sonic anemometer in this regard.

The comparison of the basic statistical values, i.e. mean value $\overline{u}$, standard deviation σ_u and turbulence intensity I_u of the time series are given in Table 8.2 along with the directional average $\overline{\Phi}$ and its standard deviation σ_Φ for 20 m/s reference wind speed.

The hot-wire reference measurement shows a mean value of 17.0 m/s at 20% turbulence intensity. The sonic anemometer at 180° and the sphere anemometer measure slightly higher wind speeds, which has already been observed for the experiment with lower reference wind speed. An underestimation of 0.5 m/s for the mean value is found for the sonic anemometer in 0° orientation, which seems to be caused by the support rod upstream of the measuring volume. The lowest mean wind speed
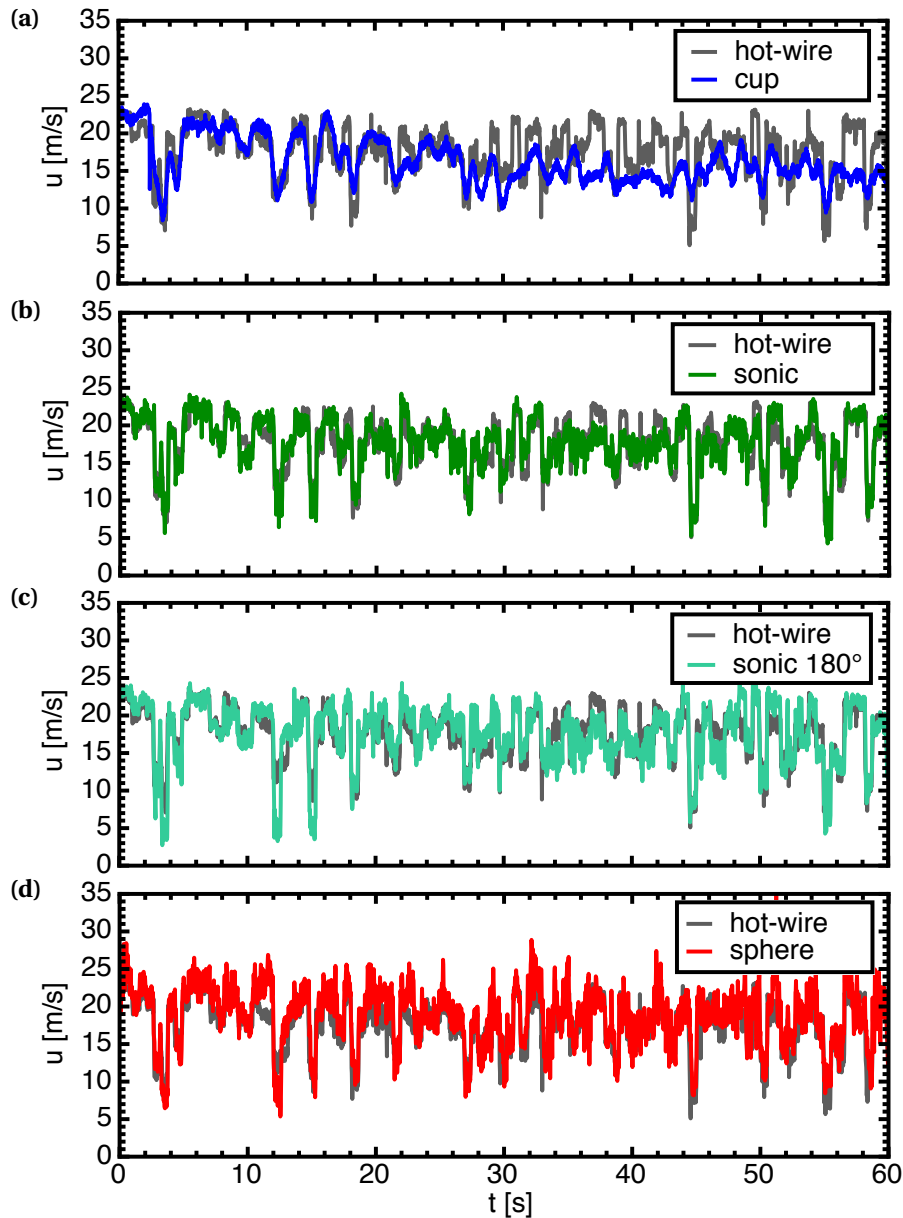
Figure 8.3: Excerpts of the first 60 seconds of the down-sampled time series measured behind the active grid at $\overline{u} \approx 20$ m/s mean velocity. The hot-wire reference (gray) is compared to (a) cup anemometer, (b) sonic anemometer in 0° orientation and (c) in 180° orientation as well as (d) sphere anemometer.

of $\overline{u} = 15.9$ m/s is measured by the cup anemometer, which confirms the impression gained from the 60-second excerpt of the time series. At the same time the cup anemometer measurement exhibits by far the lowest standard deviation σ_u and turbulence intensity I_u due to its inertia and lack of temporal resolution. The sonic and sphere anemometer agree well and match the hot-wire reference in both regards. It is worth noting, that the over-estimation of the turbulence intensity, which is found

Table 8.2: Mean value $\overline{u}$ and standard deviation σ_u of the horizontal wind speed as well as turbulence intensity I_u measured with the four different anemometers in turbulent flow with approx. 20 m/s reference wind speed. The mean wind direction $\overline{\Phi}$ and its standard deviation σ_Φ a listed for sonic and sphere anemometer.

	$\overline{u}$ [m/s]	σ_u [m/s]	I_u [%]	$\overline{\Phi}$ [°]	σ_Φ [°]
hot-wire	17.0	3.4	20	–	–
cup	15.9	2.58	16.2	–	–
sonic 0°	16.5	3.4	21	182.0	5.9
sonic 180°	17.6	3.5	20	180.6	5.2
sphere	17.8	3.5	20	180.2	13.7

in the 8 m/s wind speed case for the 0° orientation of the sonic anemometer, is not observed at 20 m/s inflow. Although this contradicts the findings of the 8 m/s case at first sight, the internal calibration correction of the sonic anemometer can be assumed to cause the different effects.

The comparison of the power spectra of the four anemometers for the 8 m/s and 20 m/s inflow, respectively, is based on the fully resolved 1 kHz data of all sensors and the resulting spectra are depicted in Figure 8.4.
The hot-wire anemometer as a reference sensor features the highest temporal resolution and hence it is expected that the power spectral density slope covers the entire range of frequencies up to 500 Hz. One peak at 3 Hz can be clearly seen in the spectrum for $\overline{u} \approx 8$ m/s (Fig. 8.4, a), while two peaks at about 3 Hz and 4.5 Hz are present in the flow for $\overline{u} \approx 20$ m/s (Fig. 8.4, b). The power spectra of the cup anemometer data for both inflow velocities show a significant drop-off in power spectral density even below frequencies of 1 Hz and show no response at all to frequencies above 2 Hz. This is not surprising, since cup anemometers are known for their limited temporal resolution in the order of 1 Hz. The sonic anemometer spectra follow those of the hot-wire reference well up to approximately 10 Hz for the low wind speed and up to 5 Hz for the higher wind speed. A reduced dynamic response can be seen beyond 10 Hz and a dip at the maximal temporal resolution of 32 Hz is clearly visible. This first minimum of the power spectral density is followed by recurring periodic dips. Structures like these indicate a moving averaging, which has not been performed during post-processing, but is probably part of the sonic anemometer's internal signal processing.
Moreover, the power spectral densities for both reference wind speeds saturate at a higher level in case of the 0° orientation of the sonic anemometer than for the 180° orientation. This can be presumed to stem from wake effects due to the upstream support structure in the 0° orientation.

A well-matching power spectral density at the lower mean wind speed is observed for the sphere anemometer, which resolves the peak at 3 Hz and is fairly close to the
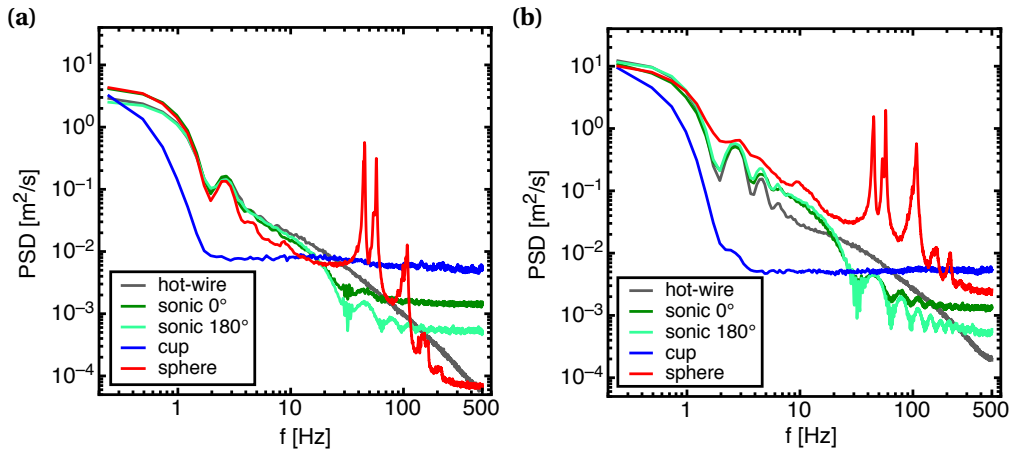
Figure 8.4: Power spectral density of the horizontal wind speed measurements with hot-wire (gray), cup (blue), sphere anemometer (red) and sonic in 0° (dark green) and 180° orientation (light green). The spectra are shown for approx. (a) 8 m/s mean wind speed and (b) 20 m/s mean wind speed.

sonic and hot-wire signals up to 20 Hz. Unlike for the sonic anemometer, no drop-off of the spectral density is found beyond 20 Hz, but two pronounced peaks at the two natural frequencies of 45 Hz and 57 Hz are present as well as their harmonics. An almost similar spectrum is found for the higher wind speed of approximately 20 m/s, albeit the peaks at 3 Hz and 4.5 Hz are not resolved, but instead appear to be merged to one broader peak.

8.3   Comparison of the Wind Direction Measurements

The wind direction measurements of the sphere anemometer can only be compared to the sonic anemometer measurements, since neither hot-wire nor cup anemometer are capable of directional measurements. Although reproducible inflow patterns are generated with the active grid protocol, it is not designed to generate distinct inflow angle variations, but rather to produce varying wind speeds due to changes in the local wind tunnel blockage.

The measurements with the sonic anemometer performed in two different orientations are analyzed in order to estimate the impact of the support structures on the wind direction measurements. The 0° orientation with the support rod upstream the measuring volume and the 180° orientation with the support exactly downstream the measuring volume are selected for the experiment, since these cases are likely to exhibit the largest differences. The wind direction measurements in the 0° case include sudden jumps between values around 0° and values close to 360° due to the fluctuations in the flow. Wind directions close to $\Phi = 360°$ are therefore wrapped to be around 0°. The measured wind directions for the sphere anemometer and the sonic anemometer in 0° alignment are shifted by 180° in order to match the data range from the sonic anemometer's 180° orientation for easier comparison.

Exemplary, the first 60 seconds of the wind direction measurements with sphere anemometer and both sonic anemometer orientations are depicted in Figure 8.5 (a) for $\overline{u} \approx 8$ m/s and in Figure 8.5 (c) for $\overline{u} \approx 20$ m/s inflow velocity. The measured inflow angle variations agree for both sonic anemometer orientations, and several pronounced wind direction peaks from the turbulent inflow are resolved. The inflow angle time series from the sphere anemometer covers these peaks as well, but the magnitude of the peaks is larger. The mean wind directions $\overline{\Phi}$ and corresponding standard deviations σ_Φ are listed in Tables 8.1 and 8.2 for the reference wind speeds of 8 m/s and 20 m/s, respectively. The sphere anemometer means agree well with the sonic anemometer measurements for both considered wind speeds. However, the overall fluctuations around the mean wind direction are increased for the sphere anemometer, which is also evident in the standard deviation of the 1-minute mean values of the wind direction Φ, presented in Figures 8.5 (b) and (d). This is probably caused by the mechanical oscillations due to vortex shedding from the sphere and is further analyzed by means of the power spectra from both anemometers.

The power spectral density of both sonic anemometer measurements and of the sphere anemometer measurement are compared in Figure 8.6. A higher power spectral density is observed in the sphere anemometer direction measurements, which exceeds the sonic anemometer data by about a half order of magnitude in the frequency range up to 10 Hz. This can be attributed to the mechanical excitation of the anemometer. The two natural frequencies of the sphere anemometer at about 45 Hz and 57 Hz are present in the spectrum as well as their higher harmonics. A comparison of the two sonic anemometer orientations reveals a higher power spectral density for the case of the 0° orientation than the 180° case with undisturbed inflow to the measuring volume. Both spectra feature the periodic dips beyond 32 Hz, which were also found in the wind speed spectra presented in Section 8.2. A striking difference between the spectra of both anemometer orientations is the appearance of sharp peaks coinciding with these spectral minima in the 0° case. It is worth noting, that these spikes are not present in the spectra of horizontal wind speeds for the 0° case (Fig. 8.4), which is somewhat surprising and cannot be explained based on the measurements. Both effects are likely caused by the internal data processing and calibration correction of the sonic anemometer.

8.4   Summary & Discussion

A comparison of the 3$^{\text{rd}}$ generation sphere anemometer and two commercial anemometers in wind tunnel experiments has been presented.
The response of cup, sonic and sphere anemometer was thereby assessed for two different reference wind speeds in reproducible turbulent inflow conditions generated with an active grid.

For the higher reference wind speed of 20 m/s, the evaluated average wind speeds of the sphere anemometer matched the sonic anemometer data and – considering
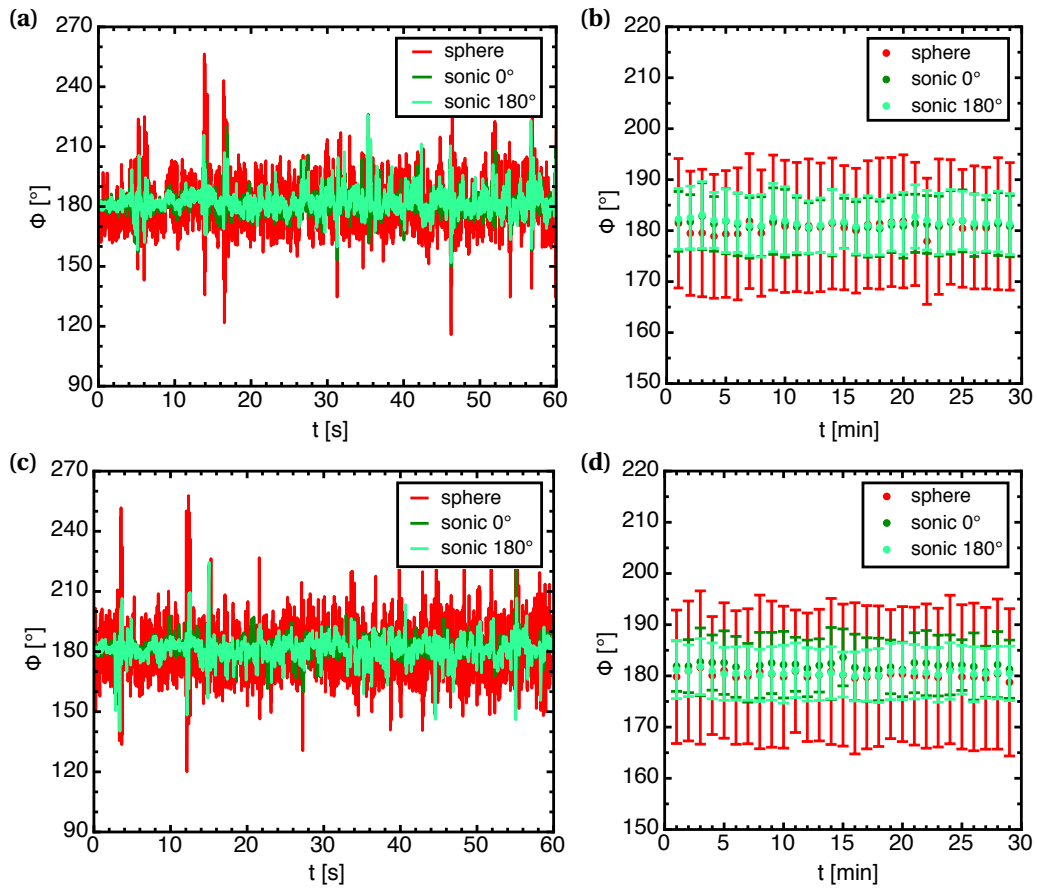
Figure 8.5: 60-seconds excerpt of the wind direction measured with sphere anemometer (red), sonic anemometer in 0° orientation (dark green) and 180° orientation (light green) for (a) $\overline{u} \approx 8\,\text{m/s}$ and (c) $\overline{u} \approx 20\,\text{m/s}$ mean wind speed. Figures (b) and (d) show the respective wind direction averages for 1-minute bins and the corresponding standard deviation.
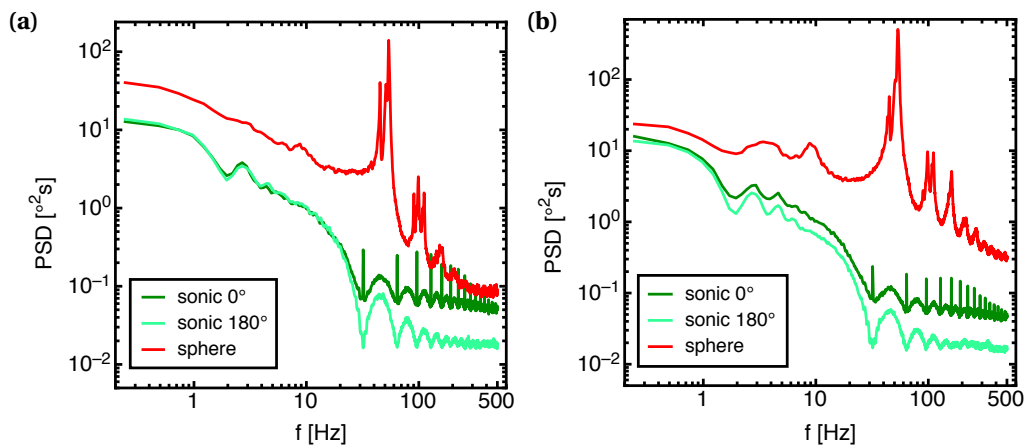

Figure 8.6: Power spectral density of the wind directions measured with sonic in 0° orientation (dark green) and 180° orientation (light green) as well as sphere anemometer (red) for (a) $\overline{u} \approx 8\,\text{m/s}$ and (b) $\overline{u} \approx 20\,\text{m/s}$ mean velocity.

the significantly different spatial resolutions – agree well with the hot-wire reference. Larger deviations of the mean value were found for 8 m/s reference speed, but in this case deviations occurred for all atmospheric anemometers. The turbulence intensities of sphere and sonic anemometer were similar in both wind speed cases, while the cup anemometer under-estimated it. The capability of the sphere anemometer to resolve gust events and fast fluctuations on a sub-second scale is evident from the considered time series excerpts. The power spectral analysis of the horizontal wind speeds showed fair agreement with the sonic anemometer, and it also confirmed the known issues of cup anemometry, i.e the high inertia and limited temporal resolution.

A good agreement of the measured mean wind directions was observed between the sphere anemometer and the sonic anemometer in both orientations. Nevertheless, the sphere anemometer directions feature a higher standard deviation, which is likely caused by the mechanical oscillations of the sensor due to vortex shedding. This is also reflected in the higher levels of the power spectral density of the wind direction measurements with the sphere anemometer.

Both investigated orientations of the sonic anemometer exhibited almost similar response behavior, although the upstream support in 0° orientation induced higher standard deviations of the wind direction and a higher noise level in the power spectra of wind speed and direction. However, these effects have not been observed to the same extent for both wind speeds. Impacts of the internal calibration correction scheme may be responsible for this, but one can only speculate about this without access to the proprietary correction algorithm, which is not shared by the manufacturer.

The overall capability of the sphere anemometer to resolve the turbulent structures in the flow is evident from the experimental investigations. The assessment proves its competitiveness to commercial sonic anemometers regarding wind speed measurements and temporal resolution.

Chapter 9

The Sphere Anemometer Field Test

The characterization of the sphere anemometer in an outdoor installation is treated in this chapter. The investigated anemometers – the 3rd generation sphere anemometer along with a This First Class Advanced cup anemometer and a Gill WindMaster Pro 3D sonic anemometer – are subject to a field test in order to investigate the anemometer behavior under realistic operational conditions. They are installed on the flat top roof of the WindLab building (W33) of University of Oldenburg's physics department. Although the site is clearly not comparable to met-mast installations, it is selected for the benefit of easy accessibility and little constraints regarding the data acquisition system.
Experiments to prepare the installation of the sensors on a common boom are presented and the actual setup of the on-site installation is introduced. The results from this field test are analyzed regarding horizontal wind speed and direction measurements, to assess the performance of the sphere anemometer prototype.

9.1 Preparative Experiments

The spacing between the installed sphere, sonic and cup anemometer on one common boom is limited in the field test and thus preparative experiments are conducted to assess possible cross-talking effects between the anemometers.
A wind tunnel experiment is set up using two of the anemometers in defined constant flow while varying the distance between the anemometers. The main focus of the work is on the evaluation of the sphere anemometer, so the cross-talking is only investigated between sphere and sonic anemometer and between sphere and cup anemometer. However, the cup anemometer is finally located next to the sonic anemometer and therefore the sphere anemometer signal was not influenced by the cup anemometer.

A measuring setup similar to the one of the calibration is used. The acoustic wind tunnel is operated in open jet configuration and the anemometers are installed on the turntable in its lower position. The experiments are performed at two different inflow

wind speeds of approximately 8.5 m/s and 19 m/s. Reference wind speeds u_{Ref} are measured with the pairings of Pitot tubes in the settling chamber and static pressure holes in the wind tunnel nozzle, which are connected to an analogue Betz micro-manometer. The electric signals of the sphere anemometer and the respective commercial sensor are recorded using a Data Translation DT9816-A AD-converter connected to the measuring PC with LabVIEW software. Signals are acquired for 15 seconds at f_s = 1 kHz sampling frequency for each combination of sensor position and reference wind speed.

As first pairing, sphere and sonic anemometer are placed next to each other on a aluminum x-profile in the center of the turntable, so the that the distance of both sensors can be varied. The center of the measurement volumes for both sensors are on the same height level in 35 cm downstream distance from the wind tunnel outlet. The sonic anemometer is used in southward orientation (180°) with its two support rods located at $\pm 60°$ from the flow direction as sketched in the top view of the setup in Figure 9.1 (a). The center of the sphere is at the same downstream distance of the wind tunnel nozzle as the two support rods of the sonic anemometers. The arrangement of the sensors is sketched in Figure 9.1. The variation of the signal is measured depending on the distance between the front support rod and the sphere edges. While the sonic anemometer is fixed at its position, the sphere anemometer is initially located in a distance of 56 cm (8 D) and is gradually moved closer in steps of 3.5 cm (0.5 D) up to a distance of 2.5 cm.

(a)   **(b)**
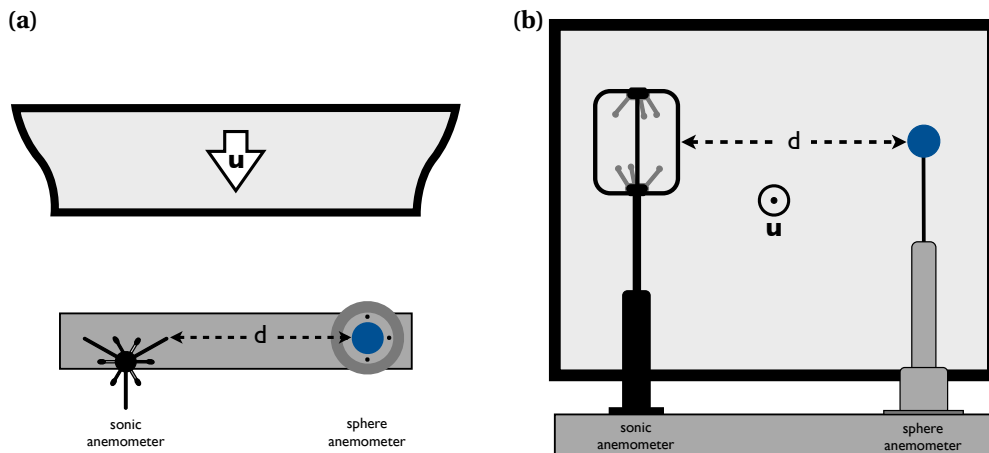
Figure 9.1: Sketched setup for the measurement of the anemometer cross-talk. The distance d between the edge of the sphere anemometer and the support rod of the fixed sonic anemometer was varied. (a) Top view of the setup with the center of the sphere anemometer being in the same distance to the wind tunnel as the two front rods of the sonic anemometer in southward orientation. (b) View from downstream. The measurement volume of the sonic anemometer is on the same height as the center of the sphere.

Figure 9.2 shows the dependency of the measured wind speeds on the distance d between the two sensors for the sphere and the sonic anemometer. The measured wind speed is normalized with the reference wind speed from the pressure probes

and the distance is given in absolute values d and normalized to the sphere diameter D in both plots. As seen in Figure 9.2 (a), there is no noticeable influence of the sphere anemometer on the sonic anemometer measurements for almost all distances. Only a minimal speed-up can be observed for the lower reference wind speed at very short distances below 5 cm. Similarly, no influence on the sphere anemometer measurements is visible for spacings larger than 30 cm. A slight increase of the measured wind speed is present for closer distances, which yields in a significant drop-off in the very vicinity of the sonic anemometer support rod (d<5 cm). In general, the mutual influence of the sensors distance on the measurement is more pronounced for the lower reference wind speeds. The widely unaffected sonic anemometer measurement can
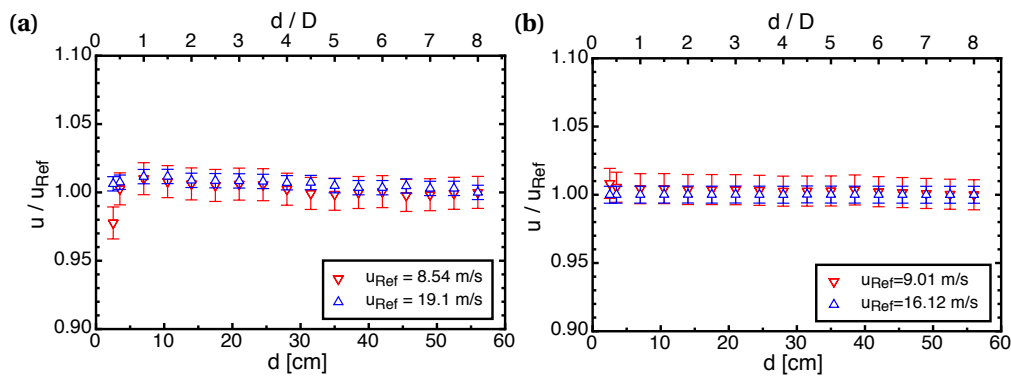

Figure 9.2: (a) Normalized sphere anemometer wind speed over distance to sonic anemometer rod and (b) normalized sonic anemometer wind speed as function of the sphere anemometer distance.

be explained by its sensor construction. Only the passive support structures are in the immediate vicinity of the altered flow region around the sphere anemometer. The measuring volume of the sonic anemometer is located further inboard and remains therefore widely unaffected. On the contrary, the active sphere-tube-element of the sphere anemometer is directly exposed to the altered flow in the vicinity of the sonic support rod. Although the support is small, this effect is found in the wind speed measurements for close distances as seen in Figure 9.2 (a). Consequently, the spacing between the anemometers in the field experiment needs to be larger than 30 cm and should likely be chosen to be even larger.

A similar treatment is performed for the cup anemometer and sphere anemometer pairing. Although both anemometers are not installed directly next to each other in the field experiment, the general behavior of the sphere anemometer in the vicinity of the cup anemometer rotor might be of interest for future installations. Similar to the above mentioned experiment, the cup anemometer is moved towards the sphere anemometer. The wind speed measurements with both sensors are normalized with the reference wind speed for two different inflow velocities around 10 m/s and around 20 m/s. As a consequence of the cup anemometer rotation, two different situations are accounted for in the experiment. In the first case, the cup anemometer is moved towards the sphere anemometer from the right, causing the closer cup to

move against the inflow, while in the second case, the anemometer is approaching the sphere anemometer from the left, and thus the closer cup is moving downstream with the wind. Both cases are treated for the lower wind speed of approximately 10 m/s and the normalized wind speeds are plotted against the distance d and the normalized distance d/D in Figure 9.3. The normalized cup anemometer wind speeds shown in Figure 9.3 (a) collapse for large distances to the sphere anemometer, but the effect of the anemometer becomes clear for smaller distances below approximately 20 cm. Moreover, the two different cases can be easily distinguished. Approaching the sphere anemometer from the right, the upstream movement of the cup in its vicinity leads to a speed-up before the wind speed measurement collapses at distances below 5 cm. On the contrary, the approach from the left with the closer cup moving downstream with the wind, starts to impact the wind speed measurements earlier. A slight wind speed decrease can already be noticed at distances of 20 cm between cup and sphere anemometer and the effect is significantly stronger compared to the other case.
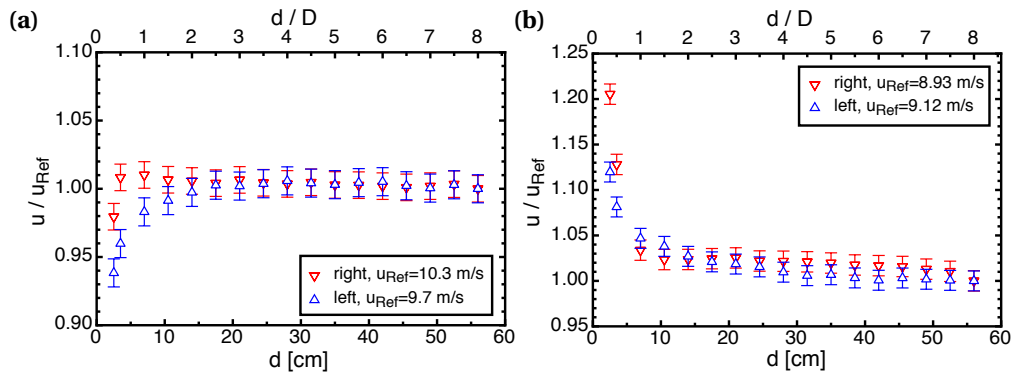

Figure 9.3: (a) Normalized cup anemometer wind speed depending on distance to the sphere anemometer. (b) Normalized sphere anemometer wind speed depending on distance to cup anemometer.

Considering the sphere anemometer measurements (Fig. 9.3, b), an increasing wind speed is found for the case of the cup approaching form the left for distances closer than about 40 cm. The other case of the cup movement from the right causes a speed-up of the sphere anemometer measurement already at around 52 cm, which remains at a constant level up to 10 cm distance. Below 10 cm, the measured wind speed increases drastically, exceeding the case of an approach from the left by about 0.1. As a consequence from these considerations, the sphere anemometer should not be located closer than 56 cm from the cup anemometer, regardless of the side.

In order to estimate the acceptance angles of the anemometer depending on the distance, the above experiment is conducted for three rotations of the anemometer boom (x-profile) exposing it to flow directions of 30°, 45° and 60°. Only the combination of sphere anemometer and cup anemometer is treated, since the previous experiment for 0° inflow showed a stronger distance dependence between those two anemometers than between sphere and sonic anemometer. It is thus considered a "worst-case" scenario. Measurements are taken with the sphere anemometer posi-

tioned left of the cup anemometer. The counter-clockwise rotations of 30°, 45° and
60° with respect to the anemometer's 0° position result in the sphere anemometer
moving further downstream and thus being subject to the wake of the upstream cup
anemometer.

Figure 9.4 shows the dependency of the normalized sphere anemometer wind speed
(Fig. 9.4,a) and the dependency of the normalized cup anemometer wind speed mea-
surement (Fig. 9.4,b) on the the distance for the three different inflow angles between
30° and 60°. The sphere anemometer wind speed measurement shows no impact of
the presence of the upstream cup anemometer for all inflow angles down to a distance
of $d = 30$ cm between both anemometer edges. Smaller spacing causes a speed-up of
the signal at the largest inflow angle $\Phi = 60°$. The speed-up occurs at closer distances
for smaller inflow angles, which is expected as the projected distance

$$d_{\mathrm{proj}} = d \cdot cos(\Phi) \qquad (9.1)$$

between both anemometers is larger for smaller inflow angles Φ. The cup anemome-
ter on the other hand shows only a relatively small effect of the presence of the down-
stream sphere anemometer. An impact can be seen only for spacings below 20 cm for
the largest inflow angle $\Phi = 60°$.
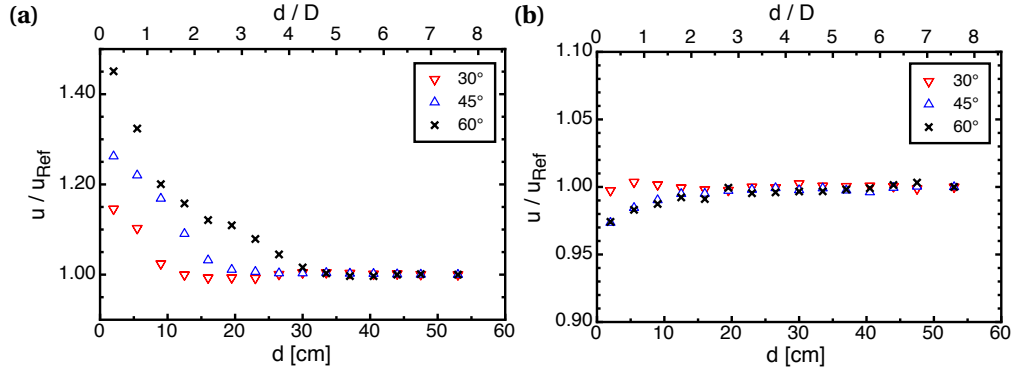
Figure 9.4: Impact of the distance between sensors on the measured wind speed for 30°, 45°
and 60° inflow direction. Horizontal wind speed of (a) the sphere anemometer and (b) the
cup anemometer measurements.

As a consequence of the wind tunnel experiments on the impact of the distance
between the anemometers on the common anemometer boom for the field experi-
ment, it can be concluded, that a distance of 50 cm or more between the anemome-
ters is desirable in order to avoid cross-talking and wake effects in a wide range of
inflow angles. For this anemometer spacing, the experiments also confirm that an ac-
ceptance angle of ±60° can be chosen without the risk of wake effects impacting the
measurements with the three sensors.

9.2   Installation & Site Description

The first field testing of the sphere anemometer is performed on the flat roof of the WindLab building (W33) of the University of Oldenburg. The designated experimental area on the roof is framed on the south-west by an elevated engineering room of about 3 m height and on the south by lower, but also elevated roof-lights. The other wind directions are free of obstacles. An aerial view of the test site is presented in Figure 9.5. All sensors are installed on a common anemometer boom taking the find-
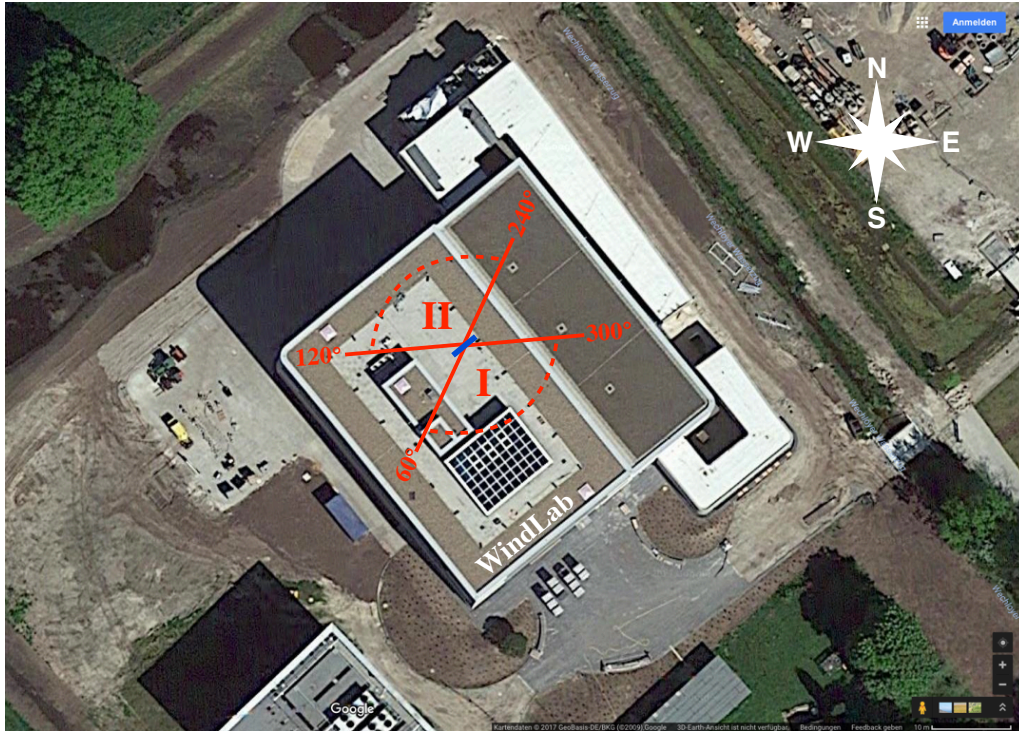

Figure 9.5: Aerial view of the anemometer installation site on the flat roof of the WindLab building. The position of the anemometer boom (blue, not to scale) is sketched as well as the selected wind direction sectors I and II (red) in the anemometer coordinate system. (Images ©DigitalGlobe, GeoContent, Map data © 2017 GeoBasis-DE/BKG (© 2009), Google)

ings of the preparatory experiments of Section 9.1 into account regarding the minimal distance between the sensors and the selected wind direction sectors. The boom, depicted in Figure 9.6, is mounted on a tripod at about 1.5 m height above the roof level. The tripod is not set up directly at the edge of the roof due to constraints at the site, but it is placed in the center of the experimental area as marked in Figure 9.5. In general north-westerly wind directions are predominant at the site of the WindLab and the anemometer boom alignment perpendicular to the north-westerly wind direction is therefore selected. However, the building and its elevated structures on the roof alter the flow directions and increase the turbulence level at the site. It is nevertheless considered reasonable for a first field test with the aim of assessing the sphere anemometer against the two reference sensors rather than performing a common site

assessment. The benefit of this easily accessible site therefor outweighs possible issues linked to altered wind conditions.

Figure 9.6: Photo of the anemometer boom with sphere, sonic and cup anemometer (left to right) installed on the roof top of the WindLab building. View from 0° wind direction (south-east).

9.3   Data Acquisition & Processing

The data acquisition (DAQ) at the test site is performed using a measurement PC with two connected USB analog-digital converters. A combination of a Data Translations DT9816-A AD converter and a National Instruments NI-6211 AD converter is set up in order to be able to acquire the four sphere anemometer signals and the five signals of the reference sensors (4× sonic, 1× cup). Both AD converters provide 16 Bits resolution for an input range of ±5 V. Synchronization of the sphere anemometer channels is crucial, since the four signals are used to calculate the instantaneous components of the laser displacement (x, y). The DT9816-A allows for the simultaneous sampling of the input signals and is thus chosen for the sphere anemometer, while the NI-6211 acquires the channels in multiplexed operation. It is used for the acquisition of the four sonic anemometer signals, i.e. the horizontal wind speed magnitude, horizontal wind direction, vertical wind speed and anemometer status signal, and the cup anemometer signal. A minimal time lag between the reference signals is inevitably caused by the multiplexing in this setup, but it is not considered crucial due to the low temporal resolution of the anemometers and the independence of the acquired signals.

The data acquisition with the two AD converters is controlled by a LabVIEW program. Signals are sampled at $f_s = 200$ Hz with both devices and the buffered data is stored in two minute intervals. However, the use of two separate DAQ devices results in a timing disparity beyond the multiplexing as each AD converter uses its internal sample clock. The synchronization of the signals is thus addressed in the first step of post

processing by shifting the calibrated signals of the sphere anemometer against those of the reference sensors based on the maximum of the cross-correlation function as described in Appendix D.

The full data set comprises measurements of all anemometer channels during five consecutive days from 23.–27. December 2016. Data corresponding to the two preferred wind direction sectors of $0°\pm60°$ (I) and $180°\pm60°$ (II) is extracted from the full data set. The wind direction Φ is selected based on the sonic anemometer measurements, since it is the designated reference sensor. Averaged properties of the entire measuring period are summarized in Table 9.1 for the full data and the selected data sets I and II. At 58% data share, the majority of the recorded data is found for wind directions in the sector II, which is expected as it is centered around the designated main wind direction at the WindLab site. The rather free inflow conditions for this sector are reflected in higher horizontal mean wind speeds $\overline{u}$ = 3.4 m/s compared to very low speeds or $\overline{u}$ = 1.9 m/s for the obstructed wind sector I, which has a data share of only 18% during the measured five days. Both sectors feature a slight downward vertical wind component $\overline{w}$ = −0.4 m/s.

Table 9.1: Properties of full data set and selected wind direction sectors from five days of field testing. The data share of each selected sector is given as well as the mean horizontal and vertical wind speeds, $\overline{u}$ and $\overline{w}$, and the direction $\overline{\Phi}$ measured with the sonic anemometer reference.

wind sector	$0° - 360°$	I $0°\pm 60°$	II $180°\pm 60°$
data share [%]	100	18	58
$\overline{u}$ [m/s]	3.2	1.9	3.4
$\overline{w}$ [m/s]	-0.5	-0.4	-0.4
$\overline{\Phi}$ [°]	6	22	156

As a result of the site conditions, it is desirable for the anemometer evaluation to limit the further data analysis to the unobstructed wind direction sector II of $180°\pm 60°$ with respect to the sonic and sphere anemometer orientation. However, the horizontal mean wind speed for this sector (Tab. 9.1) is very low regarding typical wind energy applications and for the sphere anemometer measuring range in particular. A subset of the data from sector II is thus chosen for the comparison of sonic, sphere and cup anemometer in the field test. The subset contains three hours of measured data from 26. December 2016, 12:30 h to 15:30 h, which features an 83% data share in wind direction sector II. At a mean wind speed of about 7 m/s, this subset is more suitable for a comparison of the three anemometers than the entire data set of sector II. For better visibility of trends, the selected data set has been down-sampled to 20 Hz for the wind speed and 1 Hz for the wind direction measurements. The spectral analyses

are however based on the fully resolved 200 Hz data in order to cover all contained natural frequencies.

9.4 Anemometer Comparison

9.4.1 Wind Speed Measurements

The measurements with all anemometers are analyzed regarding the average horizontal wind speed and turbulence intensity for the entire three hour interval. Mean wind speeds are within an interval of 0.3 m/s, as listed in Table 9.2. Taking the three hour average $\overline{u} = 6.7$ m/s of the 3D sonic anemometer as a reference, the cup anemometer exhibits some over-speeding of $\overline{u} = 6.9$ m/s, while the sphere anemometer mean is slightly below at $\overline{u} = 6.6$ m/s. These can be considered minor deviations given the highly turbulent wind conditions with measured turbulence intensities I_u between 33% and 44%. In these conditions, the cup anemometer is expected to be suffering from its inertia and thus exhibit the observed over-speeding. The turbulent conditions are not necessarily expected to affect the wind speed measurements with sphere anemometer, as has been shown in Chapter 8, but the analyzed data set is characterized by a comparably large negative wind component $\overline{w}$, as listed in Table 9.2. This may impact the sphere anemometer measurements according to the investigations of the cross-flow response in Section 7.5.

Table 9.2: Mean quantities of the data sets for the selected wind direction sector II. The mean horizontal and vertical wind speeds, $\overline{u}$ and $\overline{w}$, as well as turbulence intensity I_u, mean wind direction $\overline{\Phi}$ and its standard deviation σ_Φ are listed for the compared anemometer (if available).

<div align="center">

Sector II (180° ± 60°)

	$\overline{u}$ [m/s]	I_u [%]	$\overline{w}$ [m/s]	$\overline{\Phi}$ [°]	σ_Φ [°]
sphere	6.6	33	–	116	14
sonic	6.7	44	-1.1	146	11
cup	6.9	39	–	–	–

</div>

Exemplary time series of the horizontal wind speed measured with the sonic, sphere and cup anemometer are presented in Figure 9.7. Although only 20 minutes are plotted in Figure 9.7 (a), the excerpts are representative for the selected three hour period. The overall course of the horizontal wind speed time series in Figure 9.7 (a) is in agreement for all anemometers, as sudden wind speed increases or drops are well covered. A further zoom into the time series, given by the plotted two minute interval in Figure 9.7 (b) underlines this observation.

The average values for intervals of ten minutes constitute a commonly considered quantity in wind energy and meteorology. A comparison of the computed ten-minute mean wind speeds and turbulence intensities for the three anemometers is displayed
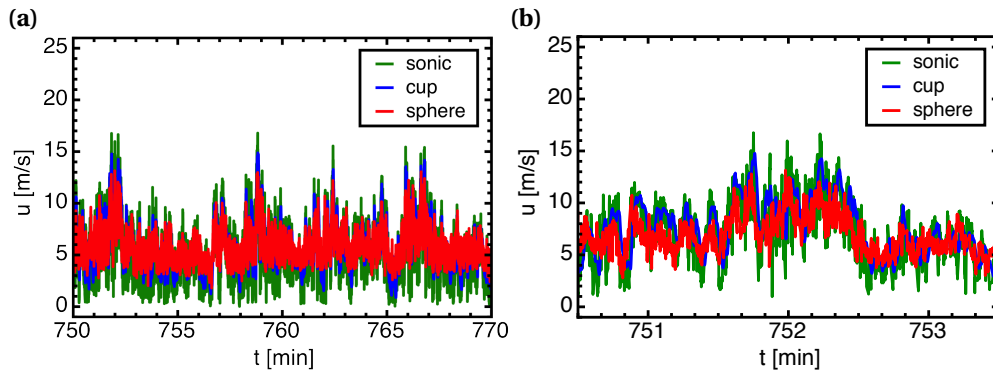
(a)

(b)

Figure 9.7: Measured time series with sonic (green), cup (blue) and sphere anemometer (red) from wind directions sector of $180° \pm 60°$. (a) 20-minutes excerpt and (b) 2-minute excerpt of the horizontal wind speed measurements.
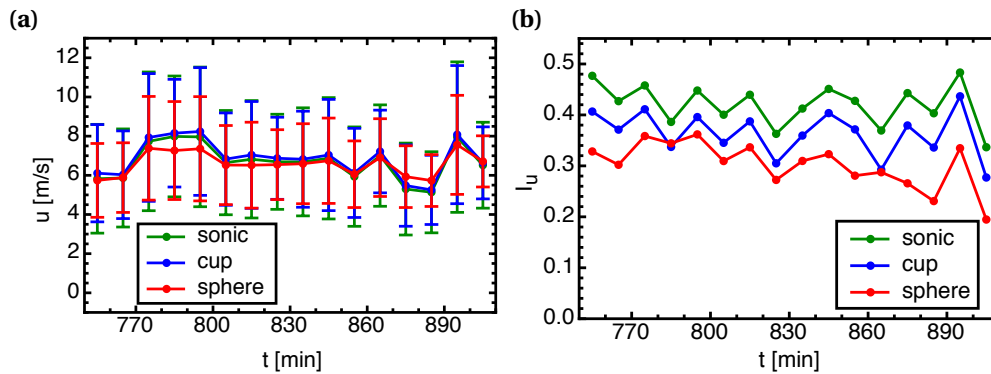
(a)

(b)

Figure 9.8: 10-minute averages of (a) horizontal wind speed u and (b) corresponding turbulence intensity I_u for sonic (green), cup (blue) and sphere anemometer (red) from wind directions sector of $180° \pm 60°$. The error bars indicate the standard deviation σ_u on the 10-minute scale.

in Figure 9.8. The plotted wind speeds agree well for most 10-minute intervals. Deviations with respect to the commercial anemometers are however observed in the sphere anemometer data, showing a reduced 10-minute wind speed between 770 and 800 minutes, while it is increased between 870 and 880 minutes. Moreover, the standard deviation σ_u is reduced for the sphere anemometer and cup anemometer compared to the sonic anemometer, as visible in the plotted as error bars (Fig. 9.8, a). This also affects the turbulence intensity I_u in Figure 9.8 (b), with the lowest values measured by the sphere anemometer and the highest values by the sonic anemometer.

In the comparison of the wind time series, the sphere anemometer and the cup anemometer appear to exhibit less dynamics than the sonic anemometer. This is reflected in a smaller range of the measured velocities and lower standard deviations. A closer look at the dynamics is gained by means of the wind speed histograms and the power spectra for the three anemometer.

The histogram of the 50 Hz wind speed measurements with all anemometers is cal-
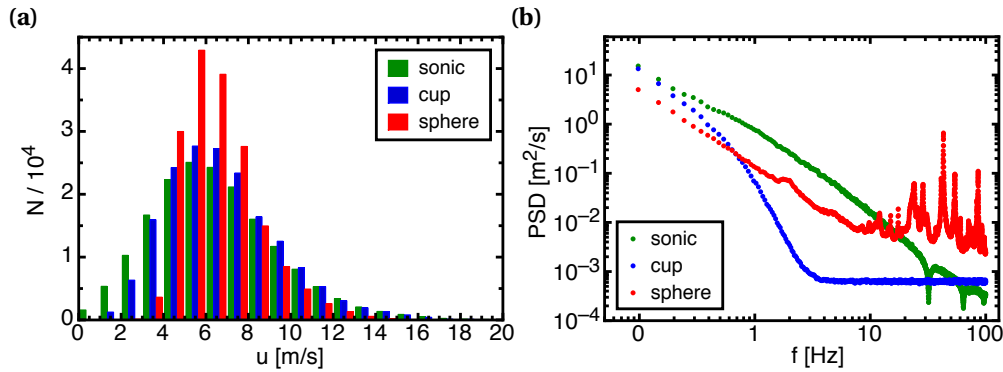
(a)   **(b)**

Figure 9.9: (a) Histogram of horizontal wind speeds for the three hour interval and (b) power spectral density of the horizontal wind speed measurements for sonic (green), cup (blue) and sphere anemometer (red) in wind sector II ($180° \pm 60°$).

culated for bin sizes of 1 m/s. The number of counts N per wind speed bin is plotted against the wind speed u in Figure 9.9 (a). The cup anemometer histogram agrees with the sonic anemometer histogram for the higher wind speeds. Lower wind speeds are less frequently measured, while values close to the mean are overly present. The sphere anemometer histogram covers an even smaller range of measured wind speeds leading to a narrower histogram with reduced counts at the higher and lower end of the wind speed bins. This is compensated for by an over-estimation for the wind speed bin around the mean value. The reduced dynamic range, i.e. the narrowed histogram, is expected for cup anemometry due to inertial effects and spatial averaging. It is however surprising that the range of the sphere anemometer data is lower than that of the sonic anemometer – and even the cup anemometer – measurements.

A better estimate of the dynamics can be obtained from the plot of the power spectral density of the 200 Hz wind speed data given in Figure 9.9 (b). The sonic anemometer spectrum is characterized by an almost linear decay region for frequencies lower than $f \approx 30$ Hz, before effects of the internal averaging procedures can be identified at $f = 32$ Hz and beyond. This is consistent with the observations from the wind tunnel tests in Section 8.2.

The cup anemometer spectrum is on the same level with the sonic anemometer only for the very low frequencies at $f \approx 0.1$ Hz, but it drops off significantly for higher frequencies and reaches the noise level for $f \leq 3$ Hz. It can thus be concluded, that the cup anemometer dynamics is reduced due to its inertial properties, which limits its temporal resolution and causes the spectral drop-off. This effect has already been identified in the spectral comparison of the wind tunnel measurements treated in Section 8.2 and is therefore independent of the field operation.

The spectrum of the sphere anemometer features lower power spectral densities compared to the sonic reference across all frequencies up to $f \approx 10$ Hz, although the decay region is also almost linear. Pronounced peaks are present for higher frequencies due to vortex shedding and natural frequencies. The reduced magnitude of the sphere anemometer in this frequency range has not been observed in the wind tunnel

measurements presented in Section 8.2, when sonic and sphere anemometer spectra agreed quite well up to about 20 Hz. The reason of the different spectral response is thus likely related to the conditions during the field test.

Two possible effects can be plausibly assumed to affect the sphere anemometer performance in the field measurements:
First, the observed deviations can be caused by an altered sphere anemometer calibration function between the wind tunnel calibration and the field installation. An increased air density due to lower ambient temperatures results in an increased slope m of the anemometer's calibration function, and higher wind speed readings for similar laser deflections are consequently calculated for the field measurements. The assumption of increased the air density due to temperature differences between the wind tunnel measurements and field operation is very likely to hold in case of these exemplary measurements, since the calibration was performed at room temperature of about 20°C, while the ambient temperature during the selected measuring period was approximately 7°C. The deviations of the air density between both cases are thus in the order of 5%. However, the impact of the changed air density affects lower wind speeds stronger than higher speed due to the non-linearity of the calibration, which can explain the significant disparity between sonic and sphere anemometer histograms at the low wind speeds, while it is marginal for the high wind speed bins.

A second contributing effect to the deviations between sonic and sphere anemometer measurements is related to its cross-flow response, assessed in Section 7.5. Information of the vertical wind component are therefore incorporated in the evaluation of the sphere anemometer field test.
The vertical wind component w at the site is analyzed from the sonic anemometer measurements, since it is the only sensor to resolve this wind component. A 20-minute excerpt of the 50 Hz time series is shown in Figure 9.10 (a). The vertical wind exhibits a net downward speed $\overline{w} = -1.1$ m/s averaged over the three hour interval (Tab 9.2) and based on the average horizontal wind speed $\overline{u}$, the angle of the net down-wind is $\gamma \approx 9°$. The 10-minute averages of the vertical wind component w and the horizontal wind speed u from sonic and sphere anemometer are plotted in Figure 9.10 (b). The underestimation of the horizontal wind speed by the sphere anemometer occurs for intervals with strong negative vertical wind component, while the small overestimation is related to the smallest vertical down-wind. This is explained by the findings of Section 7.5, since the vertical wind component causes the sphere anemometer to underestimate of the horizontal wind speed and thus deviate from the sonic anemometer. Consequently, the downward wind component also contributes to the deviation of the power spectral densities of sphere and sonic anemometers.

The altered calibration function due to the changed air density and the presence of a pronounced down-wind component are two concurring effects, which both affect the wind speed measurements with the sphere anemometer. While the higher air density yields an overestimation of the measured wind speed, a reduced wind speed reading is caused by the down-wind component. The question which of these effects is dominating depends on the boundary conditions, in particular on ambient temper-
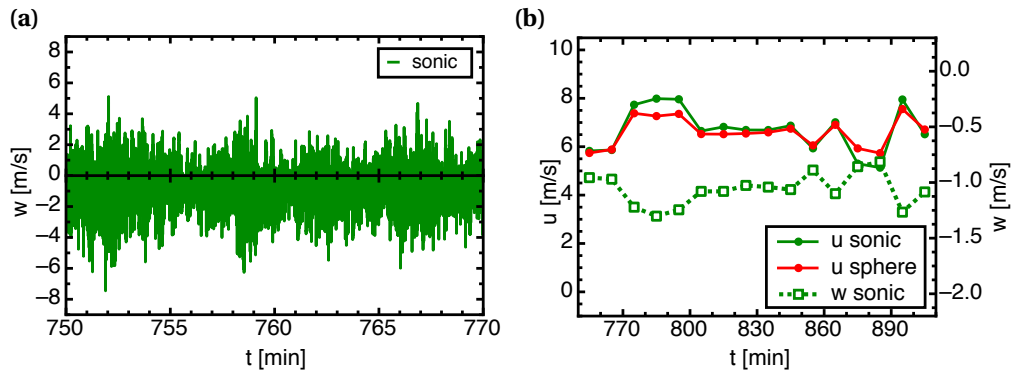
(a)

(b)

Figure 9.10: (a) Measured time series of the vertical wind component w with the sonic anemometer. (b) 10-minute means of the horizontal wind speed u measured with sonic (green solid) and sphere anemometer (red) as well as vertical wind speed w (green dashed)

ature, vertical and horizontal wind speed, due to the non-linearity of the calibration function.

9.4.2 Wind Direction Measurements

Wind direction measurements from the field test are only available for sonic and sphere anemometer, because the cup anemometer is insensitive to wind direction changes. Both time series are compared for the entire three hour period in terms of the overall mean wind direction and one-second averages. As listed in Table 9.2 for the entire data set, the mean sphere anemometer wind direction $\overline{\Phi} = 116°$ deviates from the sonic wind direction $\overline{\Phi} = 146°$ by 30°. Figure 9.11 (a) shows a 20-minute excerpt of both direction measurements on a one-second scale, which is representative for the entire three hours of selected data. The systematic difference is clearly visible in the plotted time series. Two pronounced peaks are present in the this excerpt of the sphere anemometer data, while one peak in the sonic data is apparent. These peaks are not occurring simultaneously, which indicates different prevailing inflow angles even though both anemometers are not far apart. However, the overall difference between the mean values of both direction measurements can hardly be caused by these peaks. Figure 9.11 (b) shows the histogram of wind direction fluctuations, $\Phi' = \Phi - \overline{\Phi}$, measured with sonic and sphere anemometer during the three hours. Both histograms are covering similar angle fluctuations, but the sphere anemometer histogram features slightly less counts around the mean value while positive angle fluctuations are occurring more frequent. These differences between the sonic and sphere anemometer direction fluctuations Φ' appear to be minor. Nevertheless, the higher standard deviation $\sigma_\Phi = 14°$ for the sphere anemometer compared to the sonic anemometer ($\sigma_\Phi = 11°$) indicates the impact of mechanical oscillations on the sphere anemometer direction measurements. A similar result was obtained for the comparison of wind directions measurements in the wind tunnel experiments of Section 8.3. The mean wind directions of both anemometers were matching well, in the wind tunnel experiments, though. The larger deviation of 30° found in the field
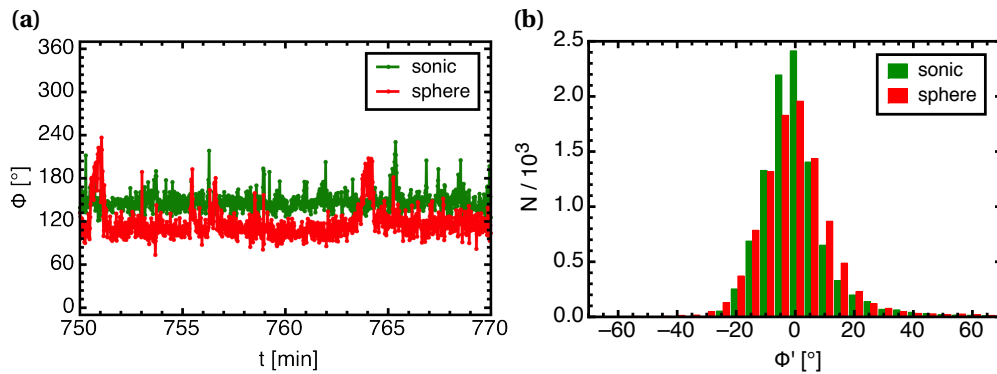
(a)

(b)

Figure 9.11: (a) 20-minutes excerpt of the wind direction measurements with sonic (green) and sphere anemometer (red) for the sector of $180° \pm 60°$ and (b) histogram of wind direction fluctuations Φ' for the three hour interval.

test is thus likely to stem from the imperfection of the installation site which affects the wind conditions. In particular, the elevated engineering building of the WindLab may alter the wind directions as sketched in Figure 9.12.
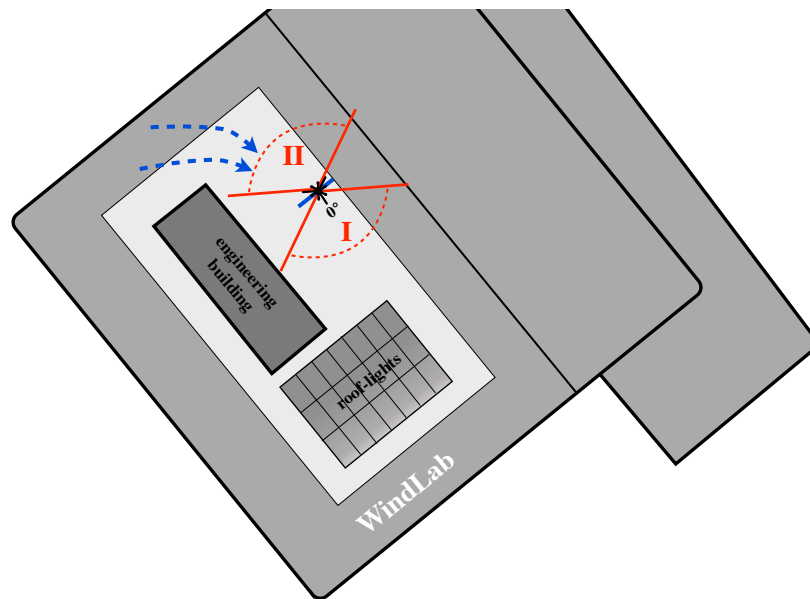

Figure 9.12: Sketch of the experimental area with adjacent engineering building and roof-lights. The anemometer boom (blue), wind sectors (red) are sketched as well as the possibly altered wind directions (dashed arrow).

9.5 Summary & Discussion

The field tests presented in this chapter were prepared in wind tunnel experiments to find limitations to the sensor spacing on a common anemometer boom and to estimate the possible acceptance angle of wind directions. As a result of these ex-

periments a minimal distance of about 30 cm between the cup anemometer and any other sensor was found to be necessary, but an even larger spacing was chosen for the final construction of the boom as a safety margin. Regarding the direction, an acceptance angle of $\pm 60°$ was found to be reasonable and it was thus used for the data selection in the field measurements.

The flat roof of the WindLab building of the University of Oldenburg was selected as site for the anemometer field test, although it cannot offer perfect conditions for the anemometer comparison. Installed on the common boom, the anemometers were placed on a tripod in the center of the experimental area on the roof. Data was acquired for a duration of five days during December 2016. The calibrated data of two rather free wind direction sectors was compared regarding their mean velocities and a significant difference in the data share of each wind direction sector was found. A more detailed comparison of the sphere anemometer and the two reference sensors was based on a three-hour data set with a high data share in the free wind sector (II), which coincides roughly with the expected main wind direction at the site.

The analyzed mean values of the horizontal wind speeds agree within 0.3 m/s for all three anemometer, while the measured turbulence intensities at about 40% were quite high. The time series of all anemometers resolved similar wind speed trends and covered the occurring gusts. However, histograms and power spectra of the horizontal wind speeds revealed a reduced dynamical range of the sphere anemometer data, which can likely be attributed to an altered calibration due to temperature and air density changes. Measurements indicate an additional impact of the negative vertical wind component in the highly turbulent environment. Although the occurring underestimation of the mean wind speed in case of the strong down-winds can be explained with the sphere anemometer's response behavior to cross-flows, further investigations are needed on this topic (cf. Sec. 7.5).

Wind direction measurements with the sonic and sphere anemometer exhibited an offset of about 30°, which cannot be explained by anemometer properties. It can be assumed, that the imperfections of the installation site with its elevated building structures caused these deviations. The fluctuations of the wind directions matched very well for the sphere and sonic anemometer, albeit the histogram of wind direction fluctuation was slightly wider spread for the sphere anemometer measurements. This is also reflected in the about 3° higher standard deviation found for the sphere anemometer.

The overall performance of the sphere anemometer in the field test is quite promising, although some subjects for future research have been identified. These include the impact of the air density and vertical wind components on the wind speed measurements, as well as the effect of mechanical vibrations of the wind direction measurement.

Chapter 10

Conclusions

This chapter summarizes the presented work on the development of the sphere anemometer at its different stages and conclusions are drawn from the characterization of the latest anemometer. Recommendations for further improvements and required investigations are also given.

10.1 Summary

The presented work aimed at the optimization of a drag based sphere anemometer for wind speed and direction measurements. It is intended to operate in the complex conditions of atmospheric wind flows, which is always present in meteorology and wind energy applications.

Its principle of operation exploits the deflection of the anemometer's flexible support tube due to the drag force exerted on the tube and an attached sphere. The highly resolving light pointer principle introduced in Chapter 3 translates the sphere deflection in a laser spot displacement on a two-dimensional position sensitive detector, which can be subsequently linked to the wind speed and direction via calibration. A square-root function for the relation between wind speed and laser displacement is expected in case of a constant drag coefficient of a smooth sphere and tube. The impact of the surface pattern on the drag of the sphere has been explained and a deviation from the square-root function is expected for patterned spheres. Although the constant drag coefficient can only be considered an approximation, it may by design be assumed for a wide range of Reynolds numbers in the subcritical regime for the smooth and dimpled spheres used on the sphere anemometer.

The first truly two-dimensional sensor constructed by Heißelmann in 2008 served as a foundation to built the further optimizations on. While some severe problems of the earlier anemometers, like the creeping and hysteresis of the acrylic glass tube, had already be addressed in this sensor, more critical issues of this anemometer design remained to be solved. In particular the pronounced scattering and anisotropy of the two-dimensional calibration spoiled this anemometer's functionality.

The first stage of the sphere anemometer development, the 1st generation sphere anemometer, was set up addressing these issues. The polystyrene sphere used by Heißelmann [2008] was replaced by a set of ABS spheres with similar diameter but varying surface patterns. A regular dimple alignment was tested at first, and while the overall 1D and 2D calibrations showed improved isotropy, still some angular dependency of the deflection remained. Since neither the regularly dimpled sphere pattern nor the tube structure could be ruled out in this setup, a further modification was made to the setup. The addition of a threaded sphere support at the tip of the GFP tube allowed for the investigation of different spheres on the very same tube. Two irregularly patterned spheres and a smooth sphere of similar size were tested in order to discriminate between effects of the sphere pattern and the tube properties on the anemometer's calibrations. While no significant difference was found between the two irregularly dimpled patterns in the one-dimensional calibration, the comparison of both irregularly dimpled spheres with the smooth sphere confirmed the drag reduction due to the surface pattern. It was reflected in a steeper calibration function, which deviated from the theoretical square-root shape. This was expected from the design considerations of the sphere anemometer and had already been accounted for by using a more general power-law function instead for the calibration.

In the analysis of the two-dimensional calibration, the coarse irregularly dimpled sphere and the smooth sphere were attached to the same GFP tube. The overall anisotropy of the 2D calibration was reduced for both spheres compared to the first approach with a regularly dimpled sphere. Nevertheless, the comparison revealed the problematic angular dependence of the anemometer deflection caused by the internal fiber alignment within the epoxy matrix. These structural anisotropies resulted in sudden jumps of the tube deflection in a approximately 60° steps.

In order to overcome the angular anisotropy of the tube deflection caused by the fiber structure, the glass-fiber material was abandoned and a stainless steel tube was chosen instead to support the sphere in the 2nd generation sphere anemometer. This consequently implied changes regarding the tube length and subsequently also the height of the anemometer housing. Both changes, the reduction of the tube length and the increased laser path in the housing, helped to improve the anemometer's natural frequency from 30 Hz to 36 Hz while maintaining the desired measuring range. The characterization of the 1D and 2D calibrations for the 2nd generation anemometer gave evidence of a greatly improved isotropy. The optimizations consequently yielded significantly reduced angular deviations of the laser deflection below 3% off of a perfectly circular shape for the wind speed range above 5 m/s.

As a consequence of the promising results obtained with the 2nd anemometer generation, the materials and geometry of this sensor remained unchanged for the 3rd generation. Improvements were focused towards the installation in the complex conditions associated with field experiments. The housing was therefor modified in order to reduce the wind load and in particular to provide water-tightness with the addition of rubber sealings between sphere, tube and housing. Moreover, the electric circuit was completely remodeled in order to comply with the industrial standards

of 4-20 mA current signals and the power supply for the laser diode was at the same time integrated in the signal amplification circuit. Investigations of the 2D calibration function revealed an increase of the angular dependence of the deflections signals, which was caused by the changes to the sensor electronics due to different amplification factors for the individual channels. However, the angle-dependence did not manifest in sudden jumps of the calibration as caused by the previously used tube materials. Instead, it resulted in a smooth, slightly elliptic shape of the 2D calibration. The eccentricity of the elliptic shape is depending on the difference between the individual amplification factors, as was theoretically confirmed.

The 3rd generation sphere anemometer has been thoroughly assessed beyond the characteristics of the 1D and 2D calibration functions, as the precision and accuracy of the wind speed readings were investigated in wind tunnel experiments. Measuring uncertainties of only 0.05 m/s were found in the relevant wind speed range above 3 m/s. This uncertainty is absolutely comparable to values for commercial anemometers, as is the sphere anemometer's only marginal deviation of 2% from the "true" reference wind speed. The temporal resolution, limited by the anemometer's natural frequency, was pushed to 45 Hz for the latest development stage of the sphere anemometer, even exceeding the commercial sonic anemometer used for comparisons. Tilt experiments in the wind tunnel were carried out to identify the impact of cross-flow components, i.e. up- and down-winds, on the anemometer readings. It features an asymmetric response characteristic with a cosine projection for the upwind case and a strong under-estimation for the down-wind case. An attempt to explain the asymmetry has been made by considering the effect of the support tube on the flow separation angles. The support may yield an increased wake region by triggering premature separation on the lower hemisphere. The consequence is an altered drag force for the upwind and down-wind scenario, which plausibly explains the observed cross-flow response. However, the experimental investigation of this hypothesis was not within the scope of this work and constitutes a basis for further investigations.

The latest stage of the sphere anemometer development has been applied to turbulent wind flows in two fundamentally different scenarios: A comparison of the sphere anemometer against the commercial cup and sonic anemometers was therefore conducted in wind tunnel experiments and in a multi-day field test. The wind tunnel experiment was performed using reproducible turbulent inflow generated for two different wind speeds with an active grid. A common and repeated motion pattern of the flaps was employed and the turbulent flow was measured with the sphere anemometer, a Thies First Class Advanced cup anemometer, a Gill WindMaster Pro 3D sonic anemometer and a highly resolving hot-wire anemometer as a reference. The wind speed measurements with the sphere anemometer were in good agreement with the sonic anemometer regarding mean wind speed and turbulence intensity. Minor deviations between these sensors and the hot-wire reference could be explained with the significantly different sensor dimensions. The cup anemometer suffered from its low temporal resolution, which resulted in a limited coverage of the large wind speed fluctuations and consequently lead to lower mean values and an under-

estimated turbulence intensity. Both, the agreement of sphere and sonic anemometer as well as the limitations of the cup anemometer were also present in the analysis of the power spectral density. Besides the horizontal wind speeds, the wind direction measurements with sonic and sphere anemometer were compared. The sonic anemometer was used in both distinct orientations – with an upstream support rod (north alignment, 0°) and with free inflow (south alignment, 180°). Due to its rotational symmetry only one orientation of the sphere anemometer was considered. Wind direction measurements agreed quite well for both anemometers. The sphere anemometer exhibits larger fluctuations, though, which could be seen in the standard deviations of the averaged wind directions as well as in the power spectral densities of the direction data. A likely cause of these larger fluctuations is the lateral vibration of the sphere due to vortex shedding.

In the field experiment, the sphere, sonic and cup anemometer were installed on a common anemometer boom on the flat roof of the University of Oldenburg's Wind-Lab building for several days of continuous wind measurements.
As preparation for the site installation, experiments were performed to investigate necessary spacing between the anemometers and the acceptance angles in order to obtain reliable measurements. The anemometer boom with the three sensors was than placed on a tripod in the center of the experimental area of the flat roof. Two wind direction sectors have been selected based on the previously analyzed acceptance angles. While one of the wind sectors was spoiled by the elevated structures of the WindLab building, the other one featured rather free inflow from the north-west, which is the predominant wind direction at this site. A three hour interval with a high data share in the free sector was thus selected for the assessment of the anemometers' performance. While all three sensors agreed well in terms of the three-hour horizontal mean wind speed, deviations were found for the turbulence intensity. However, turbulence intensities in the range of 40% were present on-site and the contributing short term fluctuations may thus be different depending on the very anemometer location.
In general, a reduced dynamic range of the horizontal wind speed measured with the sphere anemometer was found compared to the sonic anemometer. A possible explanation is the reduced ambient temperature compared to the calibration in the wind tunnel, which alters the air density by about 5% and would cause an over-estimation of the wind speed. An additional impact of the vertical wind was suspected, since a strong down-wind component was observed. Consideration of the cross-flow response, as quantified during the anemometer assessment in the wind tunnel, bears a reduction of the measured wind speed due to the down-wind conditions. Both effects can be suspected to play a role in the field experiment, but their concurring nature makes it impossible to discriminate them in this field experiment.
Large deviations of 30° were observed for the wind direction measurements with sphere and sonic anemometer. These deviations were not expected, since the wind direction measurements with both anemometers agreed well in the wind tunnel experiments. The consideration of the wind direction fluctuations revealed only minor differences

between both anemometers, as the sphere anemometer exhibited a marginally higher standard deviation. This effect, presumably caused by lateral oscillations due to vortex shedding, could hardly explain the large offset. It was thus concluded to be caused by the site conditions, which feature complex wind flows around the elevated building structures.

The performance of the latest development stage of the sphere anemometer is quite satisfying, despite the remaining challenges discovered in the field test.
The reliability of its calibration has been greatly improved by optimizations of the sphere properties and the choice of the tube material. The achieved degree of isotropy for the 2D calibration facilitates the sensor calibration procedure significantly, which is crucial for the future commercialization of the sphere anemometer.
The precision and accuracy of the 3$^{\text{rd}}$ generation sphere anemometer are competitive to commercial cup and sonic anemometers, while its temporal resolution exceeds those of industrial sonic anemometers.
The attempted transition from a conceptual laboratory sensor towards a capable anemometer for the operation in the more complex atmospheric conditions has thus been successfully achieved with the development of the latest sphere anemometer prototype – the 3$^{\text{rd}}$ generation sphere anemometer.

10.2   Outlook and Recommendations

The optimizations presented in this thesis constitute a significant advancement of the sphere anemometer toward field applications. Nevertheless, some topics have not been treated in-depth or have yet to be addressed because they were beyond the scope of this work.
Among those topics, which have already been handled during this work, is at first and foremost the sensor electronics circuit. It needs to be remodeled with particular emphasis on the equal signal amplification in order to cause less angular dependency of the 2D calibration. The aim for the 2D calibration should be the highest possible degree of isotropy, to allow for a simple and fast calibration procedure for only few inflow angles.
The reduction of the power consumption of the anemometer should also be pursued. Despite this topic has not be treated through the course of this thesis, several experienced sensor developers in the meteorology branch have urged during personal discussions to bring it well below the approximately 3 W of the latest sphere anemometer.

Another interesting and relevant characteristic to be further investigated is the anemometer's response to cross-flows. Only a brief test of this feature has been conducted in the tilt experiment and a hypothesis of the possible cause has been stated. Deeper understanding of not only the anemometer response for a broader range of wind speeds, but also in-depth scrutiny regarding the underlying flow around the

sphere and its support is required. Resolving the flow in the boundary layer and in particular the separation point poses a challenge to both experimental and computational studies. Non-invasive measuring techniques like Particle Image Velocimetry (PIV) or Laser-Doppler Anemometry (LDA) need to be employed in order to grasp these sensitive flow properties. However, the vicinity of the sphere boundary severely increases the difficulties due to reflections and the surface curvature alike. On the other hand, computational investigations would need to resolve the boundary layer flow around the curved surface and the support. This poses quite a challenge on both the mesh resolution and quality to ensure stable and yet accurate simulations and consequently increases the computational costs. It is inevitable, though, to follow either path in order to gain more insight into the root cause of the asymmetric tilt characteristics found in the experiments shown in Chapter 7.

Once the flow for different tilt angles is characterized, one can proceed by re-designing the sphere such that the asymmetric deflection is mitigated. Possible designs should remain symmetric in the horizontal plane in order to retain the circular 2D calibration, but need to deviate from the symmetry in vertical direction. A suggestion for such a sphere design is sketched in Figure 10.1. However, coming up with a suitable design of a drag body, which compensates tilt effects, can be a tedious challenge by itself.
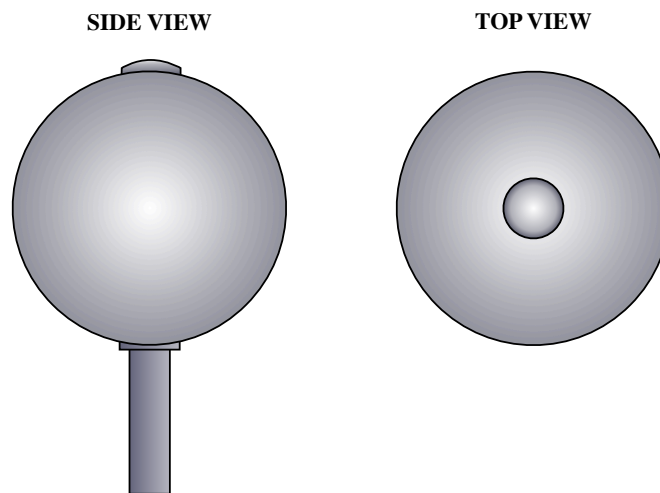
SIDE VIEW   **TOP VIEW**

Figure 10.1: Sphere design suggestion to improve cross-flow response

Some other aspects of the sphere anemometer improvement reside on the engineering side of the development. The operation on wind turbine sites and meteorological masts in cold climate regions and even in Germany during winters requires for the prevention of icing of the sphere anemometer. Although all atmospheric anemometers are prone to icing, this topic is of particular importance for the sphere anemometer. Ice accretion on the sphere surface, as shown in Figure 10.2, changes its drag characteristics while accretion on the tube will also affect the stiffness and the natural frequency of the anemometer. Thus, also the calibration function of the sphere ane-
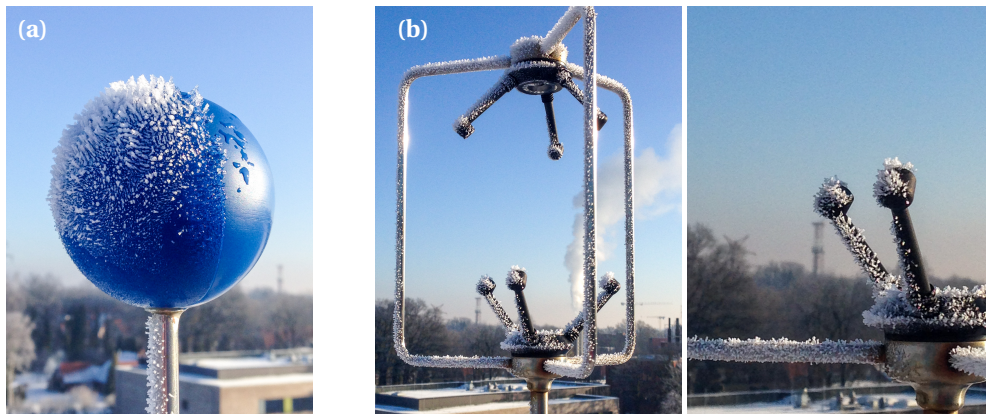
Figure 10.2: Ice accretion on the sensing elements of (a) sphere anemometer and (b) sonic anemometer.

mometer would be altered. Research regarding the severity of the impact of icing is necessary as well as a mechanism to prevent or mitigate icing on the functional components. A heating system for the support tube and possibly also the sphere needs to be implemented. Additional measures might include the use of repellent coatings to minimize dirt and ice accretion on the sphere surface without requiring a powerful heating system.

Appendix A

Convergence of the Mean Values Used for the Calibration

The use of ten-second averages of the recorded signals per wind speed and inflow angle is the basis of the one- and two-dimensional calibration functions of the sphere anemometers presented in Chapters 5, 6 & 7. However, this approach is only feasible, if the signal readings converge to their mean value within this time span. A convergence test is thus performed starting with the raw signal time series, of which the mean value is calculated over gradually expanded sample windows. The displacement magnitude $|s|$ is therefor averaged for the first n samples of the signal, corresponding to a window of length τ. The relation of samples n and time τ is given by the sampling frequency f_s.

$$|s|_\tau \quad = \frac{1}{n} \sum_{i=0}^{\tau} |s|_i \qquad \forall \tau \in]0; 10] \, s \qquad \qquad \text{(A.1)}$$
$$\text{with} \quad n = \tau \cdot f_s$$

Figure A.1 (a) shows a ten-second time series of the displacement magnitude $|s|$ of the sphere anemometer reading at $u_{\text{Ref}} = 17$ m/s and $\Phi = 0°$ inflow angle. Variations of $|s|$ in the course of the time series occur due to the impact of vortex shedding from the sphere, but the evolution of the mean value in Figure A.1 (a) pinpoints the convergence of the mean within the tenseconds interval. For this particular case, the mean value $|s|_\tau$ is found to be within $\pm 0.5\%$ of the ten-second mean after approximately 1 s (Fig. A.1, b).

However, a closer look at the actually calibrated wind speed is worthwhile, since the non-linearity of the calibration function itself may alter the outcome for the wind speed evolution and the implications on the convergence test. Using the aforementioned procedure with the calibrated wind speed time series u, the resulting convergence of the mean value $|u|_\tau$ in dependence on the averaging window is shown in Figure A.2, where $|u|_\tau$ is defined analogous to $|s|_\tau$ in Equation (A.1). While the overall shape of the fluctuating time series is similar to those of the raw displacements $|s|$, a significantly faster convergence of the averaging is observed. Approximately 0.5 s are sufficient for $|u|_\tau$ to reach the $\pm 0.5\%$ interval around the ten second mean wind speed
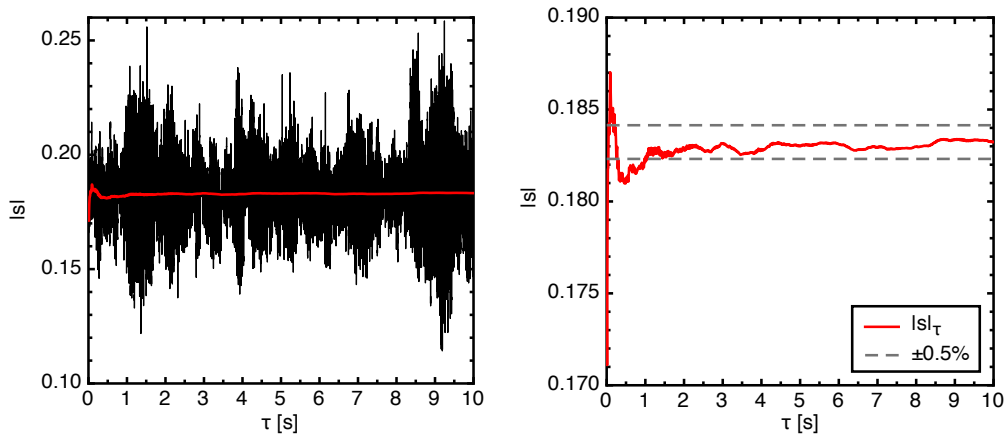
Figure A.1: (a) Fully resolved time series of the laser displacement magnitude $|s|$ (black) and mean value $|s|_\tau$ (red) as function of averaging time τ. (b) Zoom in the mean value $|s|_\tau$. The dashed lines mark the interval of $\pm 0.5\,\%$ deviation from the mean value of the entire time series.
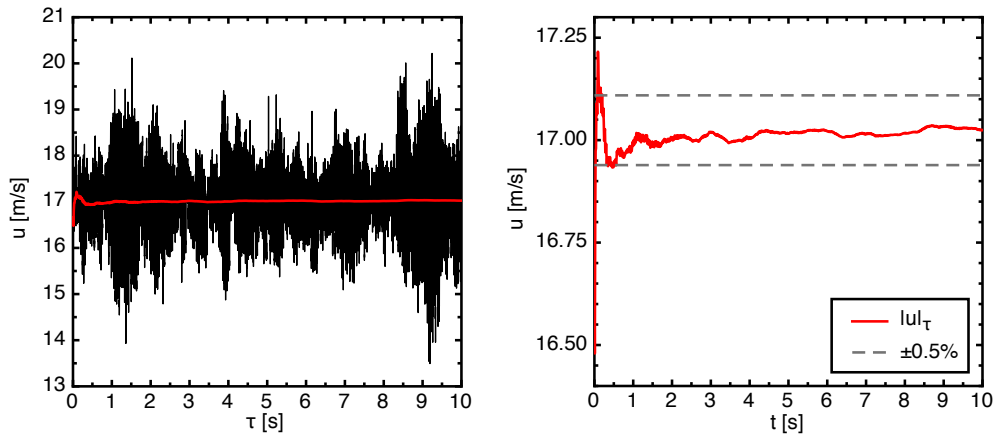
as is apparent in Figure A.2 (b).

Figure A.2: (a) Fully resolved wind speed time series $|u|$ (black) and mean value $|u|_\tau$ (red) as function of averaging time τ. (b) Zoom of the mean wind speed $|u|_\tau$. The dashed lines mark the interval of $\pm 0.5\,\%$ deviation from the mean value of the entire time series.

Similar levels of convergence have been found throughout the entire calibrated wind speed range. Taking these results into consideration, the ten-second mean values can safely be assumed to constitute a sound basis for the one- and two-dimensional calibration functions of the sphere anemometer setups.

Appendix B

Electronics of the 1$^{\text{st}}$ & 2$^{\text{nd}}$ Generation Sphere Anemometer

The sensor circuit of the first sphere anemometer versions makes use of a two-dimensional Hamamatsu P5990-S1 position sensitive detector (2D-PSD). The sensor outputs four photo currents at its anodes which are used for the calculation of the location of the laser spot's center of gravity. In order to be able to measure the small photo currents, a trans-impedance circuit is used to convert the signals to voltages and amplify them at same time. The circuit drawing for the trans-impedance amplifier circuit used in the 1$^{\text{st}}$ and 2$^{\text{nd}}$ generation sphere anemometers is depicted in Figure B.1. A pair of OPA2227 dual channel operational amplifiers is used to amplify the four anemometer channels. Each signal of the 2D-PSD is passing the trans-impedance circuit – a combination of a fixed metallic resistor and a capacitor – prior to the amplification. The resistor for the trans-impedance circuit also serves as a gain resistor. All amplified output voltages $U_1 \ldots U_4$ are connected to the signal ground via a 100nF capacitor to reduce signal noise. Figure B.2 shows the layout of the board with its top and bottom layer. No particular constraints had to be matched for the layout since both anemometer housings offer enough space.
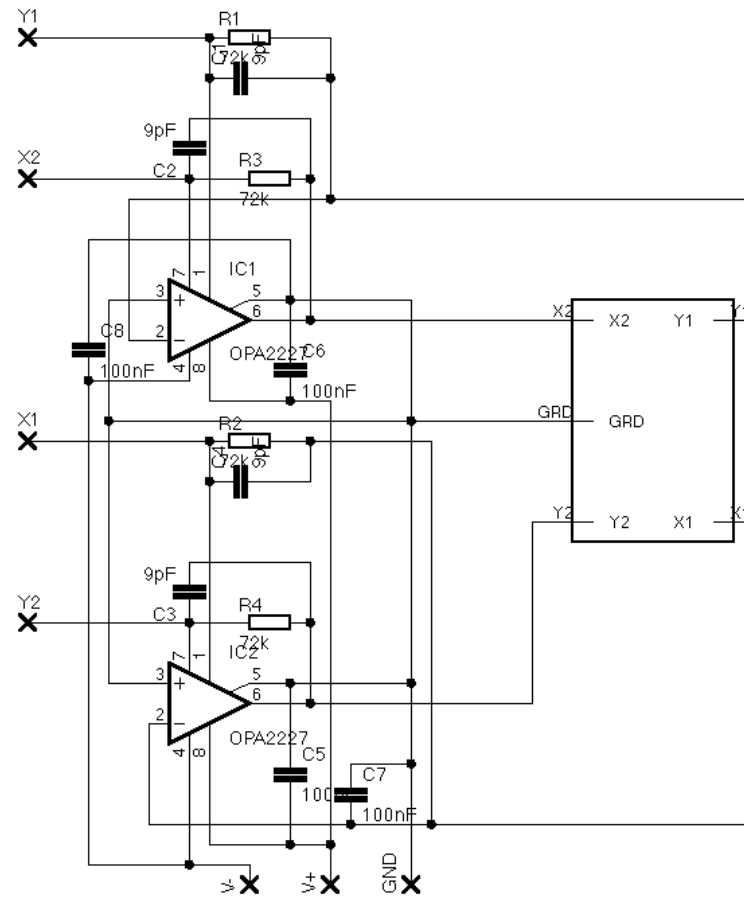
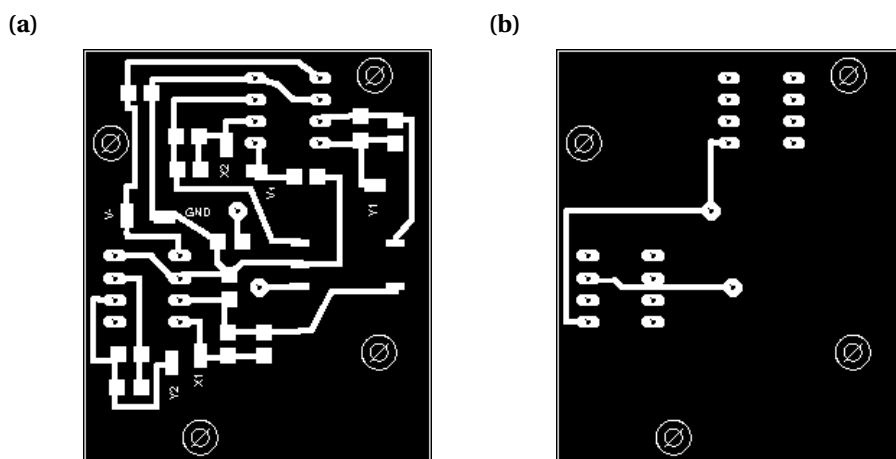**Figure B.1:** Plan of the sensor circuit for the 1st and 2nd generation sphere anemometers.

(a)   **(b)**

Figure B.2: Board design of sensor circuit for the 1st and 2nd generation sphere anemometers. (a) top layer; (b) bottom layer

Appendix C

Electronics of the 3$^{\text{rd}}$ Generation Sphere Anemometer

The 3$^{\text{rd}}$ generation sphere anemometer was designed for the operation in field campaigns. The electronics has therefore been re-designed to match the standard inputs of 4–20 mA currents required by industrial data loggers. The complete overhaul lead to a combination of the laser supply circuit and the sensor and amplification circuit with the two-dimensional position sensitive detector (2D-PSD) as main component. The entire circuit takes a supply voltage of ± 10 V from an external Mean Well T-40B switching power supply [Mean Well, 2010]. The voltage is reduced to supply the four signal amplifiers of the 2D-PSD. Additionally, it is utilized to provide the supply voltage of approximately +3.3 V for the laser diode, which can be adjusted by means of a variable resistor to prescribe a desired laser intensity.

The four channels of the induced photo currents on the 2D-PSD are amplified individually and the gain factor G_i of each amplifier is set separately by means of a variable resistor. The variable resistors are set such that the required value of 20 mA maximum current is reached for each channel when the laser spot has its maximal displacement from the center. As a consequence different amplification factors can occur for each channel.

The circuit plan of the sensor electronics is depicted in Figure C.1 and its board design is shown in Figure C.2.
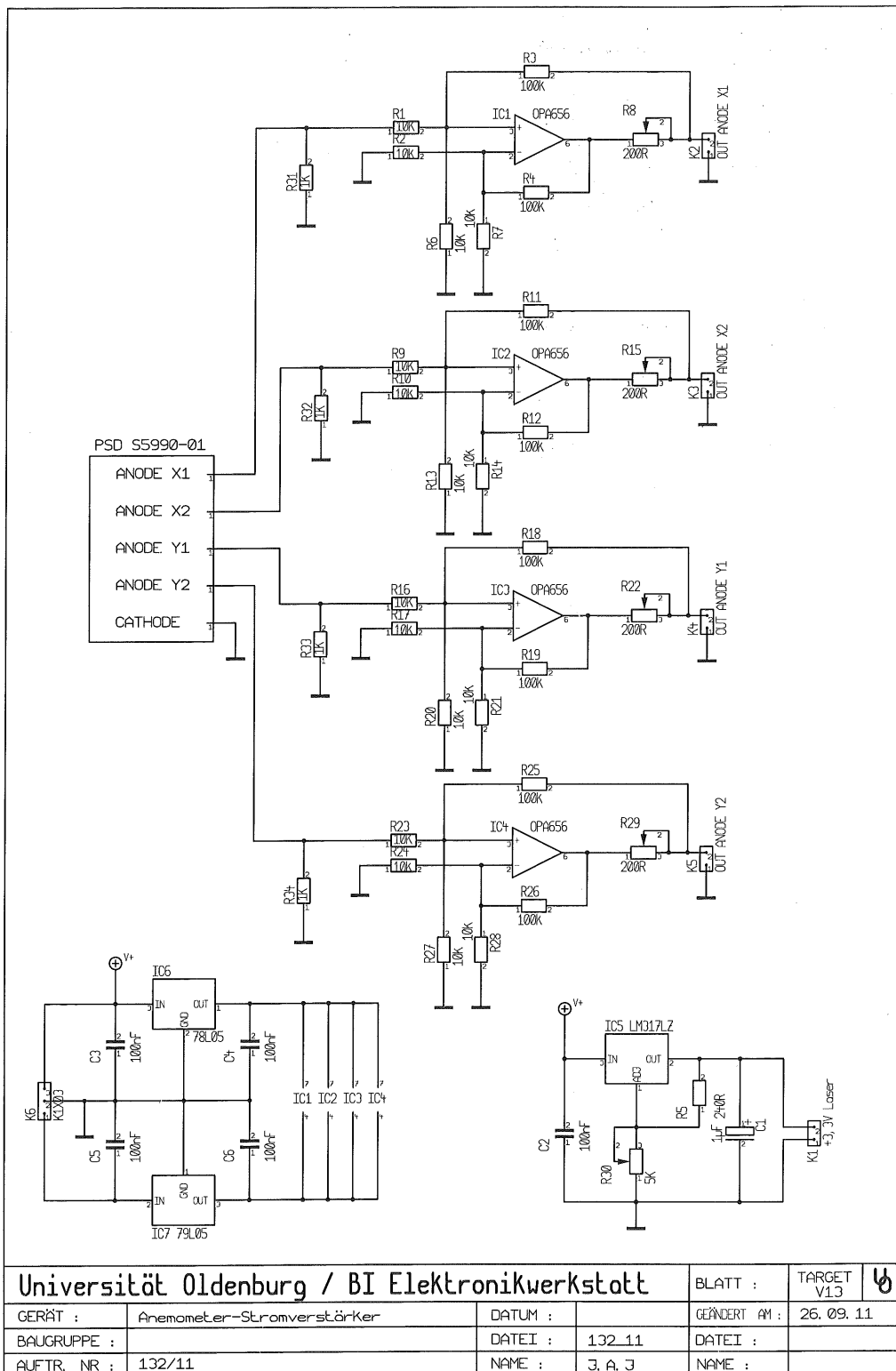
Figure C.1: Circuit diagram of the sphere anemometer sensor electronics for the application in field sites.
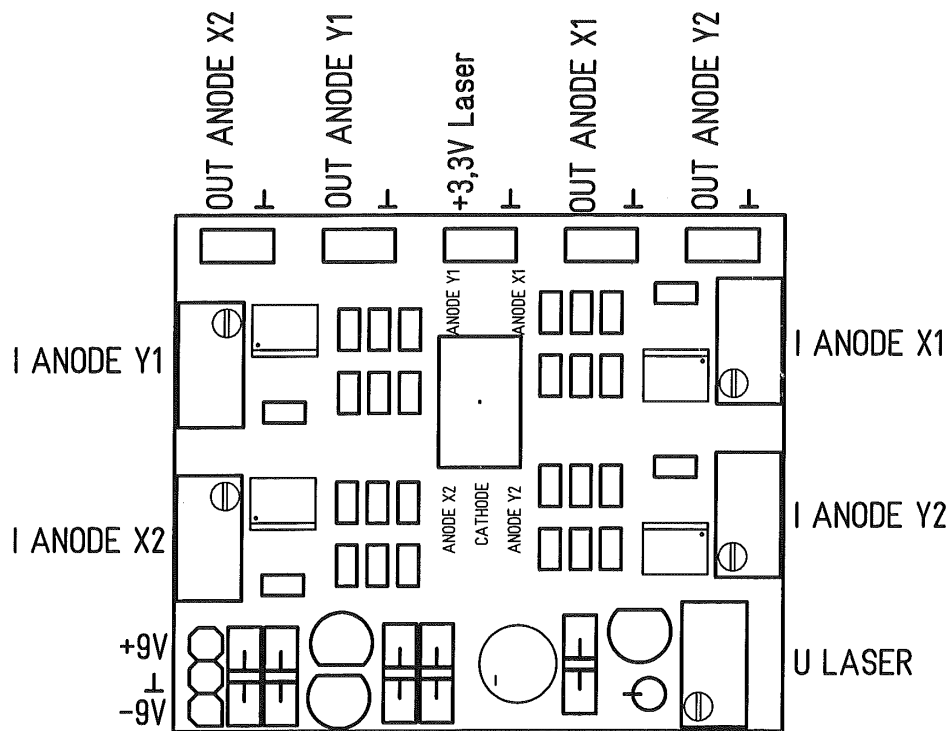
Figure C.2: Circuit board of the sphere anemometer sensor electronics for the application in field sites. The 2D-PSD was fitted on the board such that it was located in the center of the anemometer housing.

Appendix D

Synchronization of the Field Test Data

A data logging system based on a measuring PC with two different USB AD converters (ADC) was used during the field installation of the sphere, sonic and cup anemometer presented in Chapter 9. While the four sphere anemometer channels were acquired simultaneously with a Data Translations DT9816-A AD converter, a multiplexing National Instruments NI-6211 ADC was used for the signals of the reference sonic and cup anemometers. The data of the reference sensors and of the sphere anemometer are temporally shifted due to a different buffering of the two DAQ devices. Moreover, both devices use their own internal sample clock to time the data acquisition, which results in a gradual de-correlation of the measured signals. An additional time shift occurs between signals acquired with the NI-6211 due to the multiplexing, but it is in the order of μs and may be neglected. While the effect of the different sample clocks can also be neglected for short data acquisition periods, it has to be accounted in longer measurements as in the five days of field experiment.

The amount of de-synchronization was therefore assessed using a known signal, which was acquired with both DAQ devices. A saw tooth voltage variation was generated with a period of 20 seconds and the same data storage intervals were used as in the actual measurements with the anemometers in order to replicate the same conditions. An excerpt of the first channels of both AD converters is shown in Figure D.1 (a). The cross-correlation of the two signals was calculated for various time lags τ between the signals and the maximum of the cross-correlation coefficient was used to determine the time shift between the signals. The calculated time shift for each two-minute-block of measured data is shown in Figure D.1 (b). An initial time lag $\tau_0 = 9.8078$ s occurred between the channels of the two AD converters which gradually increased over time. The linear fit to the time lag data shows a rate of 8.2 ms per minute for the time lag evolution. This is well below the temporal resolution of the anemometers, which is between 22 ms for the sphere anemometer and 500 ms (cup anemometer). However, the time shift resulting from the de-correlating sample clocks needs to be considered for the comparison of the anemometer on larger time
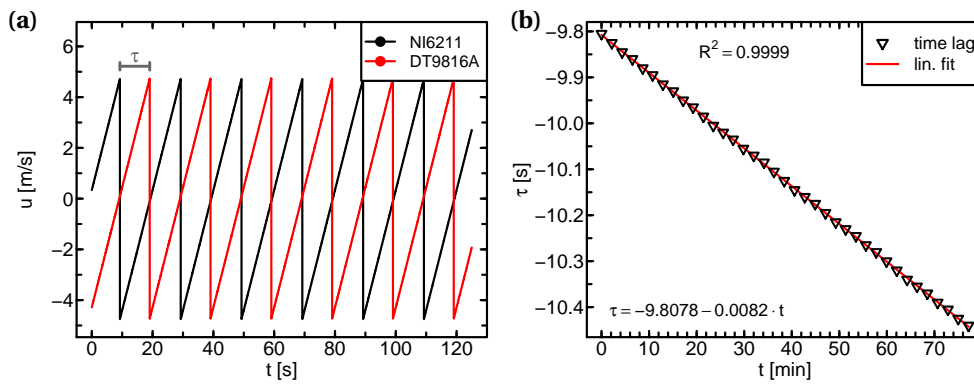
(a)

(b)

Figure D.1: Assessment of the data logging system. (a) Saw-tooth signals recored with both AD converters and (b) time lag τ derived from the cross-correlation for each recorded two-minute block.

scales. The data analysis in Chapter 9 is therefore based on time signals, which have been shifted by the time lag τ_t calculated for the respective measuring interval.

Bibliography

Achenbach, E. (1972). Experiments on the flow past spheres at very high Reynolds numbers. *Journal of Fluid Mechanics*, 54(3):565–575.

Achenbach, E. (1974a). The effects of surface roughness and tunnel blockage on the flow past spheres. *Journal of Fluid Mechanics*, 65:113–125.

Achenbach, E. (1974b). Vortex shedding from spheres. *Journal of Fluid Mechanics*, 62(02):209–221.

acin instrumenten bv (2013). *Betz Micromanometer - Factory Standard For Pressure Calibration*. Handelskade 76, 2288 Bg Rijswijk, The Netherlands.

Bailey, S. C. C., Kunkel, G. J., Hultmark, M., Vallikivi, M., Hill, J. P., Meyer, K. A., Tsay, C., Arnold, C. B., and Smits, A. J. (2010). Turbulence measurements using a nanoscale thermal anemometry probe. *Journal of Fluid Mechanics*, 663:160–179.

Baker, R. C. (2000). *Flow Measurement Handbook: Industrial Designs, Operating Principles, Performance, and Applications*. Cambridge University Press.

Barth, S. (2004). *Entwicklung eines hochauflösenden Geschwindigkeitssensors*. PhD thesis, University of Oldenburg, Carl-von-Ossietzky-Str. 9-11, D-26111 Oldenburg.

Bearman, P. and Harvey, J. (1976). Golf ball aerodynamics. *Aeronautical Quarterly*, 27:112–122.

Bruun, H. H. (1995). *Hot-wire Anemometry - Principles and Signal Analysis*. Oxford University Press, USA.

Busch, N. and Kristensen, L. (1976). Cup anemometer overspeeding. *Journal of Applied Meteorology*, 12(12):1328–1332.

Choi, J., Jeon, W.-P., and Choi, H. (2006). Mechanism of drag reduction by dimples on a sphere. *Physics of Fluids*, 18(4):041702.

Dantec Dynamics A/S (2003). *StreamLine®/StreamWare®Installation Guide & User's Guide*. Dantec Dynamics A/S, P.O. Box 121, Tonsbakken 18, DK–2740 Skovlunde, Denmark, 2 edition.

Data Translation, Inc. (2013). *ECONseries - Low Cost USB Data Acquisition Modules.*

Deacon, E. L. (1951). The over-estimation error of cup anemometers in fluctuating winds. *Journal of Scientific Instruments*, 28(8):231.

Eckelmann, H. (1997). *Einführung in die Strömungsmeßtechnik.* Teubner Studienbücher.

EIA (2016). International energy outlook 2016. Report DOE/EIA-0484(2016), US Energy Information Administration.

FT Technologies Ltd. (2015). http://www.fttech.co.uk/acu-res-technology/. Checked online on 17. December 2015.

Gill Instruments Ltd. (2009). *WindMaster Pro.* Gill Instruments Ltd., Saltmarsh Park, 67 Gosport Street, Lymington, Hampshire, SO41 9EG UK.

Green, A., Judd, M., McAneney, J., Astill, M., and Prendergast, P. (1991). A rapid-response 2-d drag anemometer for atmospheric turbulence measurements. *Boundary-Layer Meteorology*, 57:1–15.

Gunnlaugsson, H. P., Holstein-Rathlou, C., Merrison, J. P., Jensen, S. K., Lange, C. F., Larsen, S. E., Madsen, M. B., Nørnberg, P., Bechtold, H., Hald, E., Iversen, J. J., Lange, P., Lykkegaard, F., Rander, F., Lemmon, M., Renno, N., Taylor, P., and Smith, P. (2008). Telltale wind indicator for the mars phoenix lander. *Journal Of Geophysical Research*, 113.

Hamamatsu (2007). *Two-dimensional PSD S5990-01, S5991-01.* Hamamatsu Photonics K.K., 1126-1 Ichino-cho, Higashi-ku, Hamamatsu City, 435-8558 Japan.

Heißelmann, H. (2008). Optimierung des Kugelanemometers für die Messung zweidimensionaler Strömungen. Diplomarbeit, University of Oldenburg, Carl-von-Ossietzky-Str. 9-11, D-26111 Oldenburg.

Heißelmann, H., Hölling, M., and Peinke, J. (2008). Dynamic behavior of the sphere anemometer. In *Proceedings of DEWEK 2008.*

Henning, A. and Mehmet, M. (2004). Das Kugelanemometer. Bachelor's thesis, University of Oldenburg, Carl-von-Ossietzky-Str. 9-11, D-26111 Oldenburg.

Hoffmann, K. (1987). *Eine Einführung in die Technik des Messens mit Dehnungsmeßstreifen.* Hottinger Baldwin Messtechnik GmbH Darmstadt.

Hölling, M. (2008). *Sensorentwicklung für Turbulenzmessungen.* PhD thesis, University of Oldenburg, Carl-von-Ossietzky-Str. 9-11, D-26111 Oldenburg.

Hristov, T. S., Miller, S. D., and Friehe, C. A. (2000). Linear time-invariant compensation of cup anemometer and vane inertia. *Boundary-Layer Meteorology*, 97:293–307.

IEC (2005). Wind Turbine Generator Systems, Part 12: Wind turbine power performance testing. International Standard 61400-12-1, International Electrotechnical Commission.

IEC (2015). Wind Turbines – Part 12-1: Performance measurements of electricty producing wind turbines. International Standard 61400-12-1 (Ed.2), International Electrotechnical Commission.

Kaganov, E. I. and Yaglom, A. M. (1976). Errors in wind speed measurements by rotation anemometers. *Boundary-Layer Meteorology*, 10:1–11.

Kirwan, Jr, A., McNally, G., and Mehr, E. (1975). Response characteristics of a three-dimensional thrust anemometer. *Boundary-Layer Meteorology*, 8(8):365–381.

Knebel, P., Kittel, A., and Peinke, J. (2011). Atmospheric wind field conditions generated by active grids. *Experiments in Fluids*, pages 1–11. 10.1007/s00348-011-1056-8.

Kötter, H. (2009). *Ein Beitrag zum Schrägschneiden von Leichtbauprofilen.* PhD thesis, Fakultät Maschinenwesen, Technische Universität Dresden.

Kristensen, L. (1993). *The Cup Anemometer – And Other Exciting Instruments.* PhD thesis, Risø National Laboratory, Roskilde, Denmark.

Kristensen, L. (1998). Cup anemometer behavior in turbulent environments. *Journal of Atmospheric and Ocean Technology*, 15:5–17.

Kristensen, L. (1999). The perennial cup anemometer. *Wind Energy*, 2:59–75.

Labisch, S. and Weber, C. (2013). *Technisches Zeichnen: Selbstständig lernen und effektiv üben.* Springer Vieweg, 4 edition.

Laser Components (2007). *APC Laser Diode ADL-65055sA2.* Laser Components GmbH, 2 edition.

Laser Components (2008). *Datasheet Plastic Collimator Lens CAW100.* Laser Components GmbH.

MacCready, P. B. and Jex, H. R. (1964). Response characteristics and meteorological utilization of propeller and vane wind sensors. *Journal of Applied Meteorology*, 3:182–193.

Martin, Y., Williams, C. C., and Wickramasinghe, H. K. (1987). Atomic force microscope - force mapping and profiling on a sub 100-a scale. *Journal of Applied Physics*, 61(10):4723–4729.

McNally, G. J. (1970). A thrust anemometer for the measurement of the turbulent wind vector. Technical report, New York University. School of Engineering and Sciences, Department of Meteorology and Oceanography.

Mean Well (2010). *T40 Series – 40W Triple Output Switching Power Supply.*

Norwood, M., Cariffe, A., and Olszewsiki, V. (1966). Drag force solid state anemometer and vane. *Journal of Applied Meteorology*, 5:887–892.

Puczylowski, J. (2015). *Sensor development for highly resolved measurements in turbulent flows.* PhD thesis, University of Oldenburg, Carl-von-Ossietzky-Str. 9-11, D-26111 Oldenburg.

Raffel, M., Wereley, C. E. W. A. T., and Kompenhans, J. (2007). *Particle Image Velocimetry - A Practical Guide.* Springer-Verlag Berlin Heidelberg, 2 edition.

Raithby, G. D. and Eckert, E. R. G. (1968). The effect of support position and turbulence intensity on the flow near the surface of a sphere. *Wärme - und Stoffübertragung*, 1(2):87–94.

Reed III, W. H. and Lynch, J. W. (1963). A simple fast response anemometer. *Journal of Applied Meteorology*, 2:412–416.

Reinke, N., Homeyer, T., Hölling, M., and Peinke, J. (2017). Flow Modulation by an Active Grid. *ArXiv e-prints*, pages 1–17.

Rubin, H. (2004). Analytische Berechnung der Eigenfrequenzen von Stäben mit konstantem Querschnitt und konstanter Massenbelegung. *Stahlbau*, 73(11):916–922.

Ruck, B. (1987). *Laser-Doppler-Anemometrie.* AT-Fachverlag.

Sakamoto, H. and Haniu, H. (1990). A study on vortex shedding from spheres in a uniform flow. *Journal of Fluids Engineering*, 112(4):386–392.

Schlichting, H. (2000). *Boundary Layer Theory.* Springer, 8 edition.

Schrenk, O. (1929). Über die Trägheitsfehler des Schalenkreuz-Anemometers bei schwankender Windstärke. *Zeitschrift für technische Physik*, 10(2):57–66.

Schulte, B. (2007). Entwicklung und Untersuchung der Dynamik eines Widerstandsanemometers für Anwendungen in der Windenergie. Diplomarbeit, University of Oldenburg, Carl-von-Ossietzky-Str. 9-11, D-26111 Oldenburg.

Scruton, C. and Eugene, J. (1963). Stabilisation of wind-excited structures. Patent US 3076533 A.

Setra Systems Inc. (2013). *Model 239 – High accuracy, low-differential pressuretransducer.*

Silcon Sensors, Inc. (2010). *Pacific Silicon Sensors Quadrant Series Data Sheet – Part Description QP100-6-SM.* Silcon Sensors, Inc.

Smith, S. D. (1980). Evaluation of the mark 8 thrust anemometer-thermometer for measurement of boundary-layer turbulence. *Boundary-Layer Meteorology*, 19(3):273–292.

Son, K., Choi, J., Jeon, W.-P., and Choi, H. (2010). Effect of free-stream turbulence on the flow over a sphere. *Physics of Fluids*, 22(4):045101.

Strangeways, I. (2003). *Measuring the Natural Environment*. Cambridge University Press.

Strutz, D. (2014). Messung des Strömungswiderstandskoeffizienten stumpfer Körper mittels DMS Messtechnik. Master's thesis, University of Oldenburg, Carl-von-Ossietzky-Str. 9-11, D-26111 Oldenburg.

Taylor, G. I. (1938). The spectrum of turbulence. *Proc R Soc Lond A Math Phys Sci*, 164(919):476–.

Thies Clima (2009). *Anemometer First Class Advanced*. Adolf Thies GmbH & Co. KG.

Tritton, D. (1988). *Physical Fluid Dynamics*. Oxford Science Publications, 2 edition.

Wächter, M., Heißelmann, H., Hölling, M., Morales, A., Milan, P., Mücke, T., Peinke, J., Reinke, N., and Rinn, P. (2012). The turbulent nature of the atmospheric boundary layer and its impact on the wind energy conversion process. *Journal of Turbulence*, 13:N26.

Wales, D. J. and Ulker, S. (2006). Structure and dynamics of spherical crystals characterized for the Thomson problem. *Phys. Rev. B*, 74.

Wandinger, J. (2007). Elastodynamik 2, Kapitel 3. Skript zur Vorlesung.

Weitemeyer, S., Reinke, N., Peinke, J., and Hölling, M. (2013). Multi-scale generation of turbulence with fractal grids and active grids. *Fluid Dyn. Res.*, 45:061407 (16pp).

Werner, C. (2005). *Lidar: Range-Resolved Optical Remote Sensing of the Atmosphere*, chapter Doppler Wind Lidar, pages 325–354. Springer New York, New York, NY.

Wieselsberger, C. (1914). Mitteilungen aus der Göttinger Modelversuchsanstalt: Der Luftwiderstand von Kugeln. *Zeitschrift für Flugtechnik und Motorluftschiffahrt*, 5(9):140–145.

Wiesner, A., Fiedler, F., and Corsmeier, U. (2001). The influence of the sensor design on wind measurements with sonic anemometer systems. *Journal of Atmospheric and Oceanic Technology*, 18:1585–1608.

Wyngaard, J. C. (1981). Cup, porpeller, vane, and sonic anemometers in turbulence research. *Ann. Rev. Fluid Mech.*, 13:399–423.

Danksagung

Bei meinen Freunden und meiner Familie – insbesondere bei meinen Eltern – möchte ich mich dafür bedanken, dass sie mich stets in meiner Entscheidung für die Wissenschaft unterstützt haben. Meinem Bruder Daniel danke ich für die Unterstützung in unseren Diskussionen über die fachlichen und menschlichen Herausforderungen des Doktorandendaseins.

Den Soundtrack zur Erstellung dieser Dissertation steuerte die Band Bush bei.

Curriculum Vitae

Persönliche Daten

Name	Hendrik Heißelmann
Geburtsdatum	24. August 1980
Geburtsort	Osnabrück

Schulbildung

08/1987–07/1991	Grundschule Hollage, Wallenhorst
08/1991–07/1993	Orientierungsstufe Thomas-Morus-Schule, Osnabrück
08/1993–06/2000	Angelaschule Gymnasium in kirchlicher Trägerschaft, Osnabrück

Studium

10/2001–12/2008	Physikstudium (Diplom) an der Carl-von-Ossietzky Universität Oldenburg
11/2007–11/2008	Studentische Hilfskraft in der Arbeitsgruppe Hydrodynamik und Windenergie
12/2007–12/2008	Diplomarbeit mit dem Thema *Optimierung des Kugelanemometers für die Messung zweidimensionaler Strömungen* in der Arbeitsgruppe Hydrodynamik und Windenergie
seit 06/2012	Promotionsstudent an der Universität Oldenburg, Fakultät V, Institut für Physik

Wissenschaftliche Arbeit

seit 2/2009	Wissenschaftlicher Mitarbeiter bei ForWind – Zentrum für Windenergieforschung Carl-von-Ossietzky Universität Oldenburg

Erklärungen

Ich erkläre hiermit, dass ich die vorliegende Arbeit selbst verfasst habe und nur die im Literaturverzeichnis (Bibliography) angegebenen Quellen und Hilfsmittel verwendet habe.

Ich erkläre hiermit, dass die vorliegende Arbeit weder in Teilen noch in ihrer Gesamtheit einer anderen wissenschaftlichen Hochschule zur Begutachtung in einem Promotionsverfahren vorgelegen hat.

Ich erkläre hiermit, dass die vorliegende Arbeit bereits in Teilen veröffentlicht wurde.

Oldenburg, den 27. Juni 2017   ....
                                      Hendrik Heißelmann

List of Publications

Parts of this thesis have been published in the following publications:

Journals & Proceedings

M. Wächter, H. Heißelmann, M. Hölling, A. Morales, P. Milan, T. Mücke, J. Peinke, N. Reinke, and P. Rinn
Wind energy and the turbulent nature of the atmospheric boundary layer and its impact on the wind energy conversion process
Journal of Turbulence, 13, 2012

H. Heißelmann, J. Puczylowski, M. Hölling and J. Peinke
Development of highly resolving drag-based anemometers
in *Progress in Turbulence IV, Springer Proceedings in Physics 141*, eds. J. Peinke, M. Oberlack, A. Talamelli and L. Castillo (Springer, Berlin) pp. 101 - 104, 2012

H. Heißelmann, J. Peinke and M. Hölling
The sphere anemometer: characteristics and results from field test
DEWEK 2012 Proceedings, Bremen, Germany, 2012

H. Heißelmann, J. Peinke and M. Hölling
Comparing the sphere anemometer to standard anemometers for wind energy
Proceedings of the 7th EAWE PhD Seminar on Wind Energy in Europe, Delft, The Netherlands, 2011

H. Heißelmann, M. Hölling and J. Peinke
The sphere anemometer - A fast alternative to cup anemometry
in *Progress in Turbulence III, Springer Proceedings in Physics 131*, eds. J. Peinke, M. Oberlack, and A. Talamelli (Springer, Berlin) pp. 69 - 72, 2010

H. Heißelmann, M. Hölling and J. Peinke
Using the sphere anemometer for wind speed and direction measurements
TORQUE 2010 - The Science of Making Torque from Wind, Heraklion, Greece, pp. 13-18, 2010

H. Heißelmann, M. Hölling and J. Peinke
Development and characterisation of the sphere anemometer

Proceedings of the 5th EAWE PhD Seminar on Wind Energy in Europe, Durham, United Kingdom, 2009

H. Heißelmann, M. Hölling, M. Wächter and J. Peinke
Wind velocity measurements using the sphere anemometer
EWEC2009 Proceedings, Marseille, France, 2009

Oral Presentations

H. Heißelmann, J. Peinke and M. Hölling
Evaluation of the sphere anemometer for atmospheric wind measurements
67rd Annual Meeting of the American Physical Society Division of Fluid Dynamics, 23.–25.11.2014, San Francisco, USA, 2014

H. Heißelmann, J. Peinke and M. Hölling
Experimental investigation of a sphere anemometer: Wind tunnel and field tests
66th Annual Meeting of the American Physical Society Division of Fluid Dynamics, 24.–26.11.2014, Pittsburgh, USA, 2013

H. Heißelmann, J. Peinke and M. Hölling
Near-Shore Wind Measurements with the Sphere Anemometer and Standard Sensors in Wind Energy
9th EAWE PhD Seminar on Wind Energy in Europe, 18.–20.09.2013, Visby, Sweden, 2013

H. Heißelmann, D. Strutz, J. Peinke and M. Hölling
Drag coefficient measurements of spheres with different surface patterns
65th Annual Meeting of the American Physical Society Division of Fluid Dynamics, 18.–20.11.2012, San Diego, USA, 2012

H. Heißelmann, J. Puczylowski, M. Hölling and J. Peinke
Development of highly resolving drag based anemometers
iTi - Conference on Turbulence, Bertinoro, Italy, 2012

H. Heißelmann, J. Peinke and M. Hölling
The sphere anemometer: characteristics and results from field test
DEWEK, 07.–08.11.2012, Bremen, Germany, 2012

H. Heißelmann, J. Peinke and M. Hölling
Comparing the sphere anemometer to standard sensors for 2D wind measurements
64th Annual Meeting of the American Physical Society Division of Fluid Dynamics, 20.–22.11.2011, Baltimore, USA, 2011

H. Heißelmann, J. Peinke and M. Hölling
Comparing the sphere anemometer to standard anemometers for wind energy
7th EAWE PhD Seminar on Wind Energy in Europe, 27.–28.10.2011, Delft, The Netherlands, 2011

H. Heißelmann, M. Hölling and J. Peinke
A new anemometer for 2D atmospheric flow measurements in rough environments
63rd Annual Meeting of the American Physical Society Division of Fluid Dynamics, 21.–23.11.2010, Long Beach, USA, 2010

H. Heißelmann, J.Puczylowski, M. Hölling, M. Wächter and J. Peinke
Development and characterisation of highly resolving wind speed and direction sensors
DEWEK, 17.–18.11.2010, Bremen, Germany, 2010

H. Heißelmann, M. Hölling and J. Peinke
The sphere anemometer - A fast alternative to cup anemometry
iTi - Conference on Turbulence, 19.–23.09.2010, Bertinoro, Italy, 2010

H. Heißelmann, M. Hölling and J. Peinke
Using the sphere anemometer for wind speed and direction measurements
TORQUE 2010 - The Science of Making Torque from Wind, 28.–30.06.2010, Heraklion, Greece 2010

H. Heißelmann, M. Hölling and J. Peinke
Wind speed and direction measurements using the sphere anemometer
62rd Annual Meeting of the American Physical Society Division of Fluid Dynamics, 22.–22.11.2009, Minneapolis, USA, 2009

H. Heißelmann, M. Hölling and J. Peinke
Development and characterisation of the sphere anemometer
5th EAWE PhD Seminar on Wind Energy in Europe, 30.09.–01.10.2009, Durham, United Kingdom, 2009

Poster Presentations

H. Heißelmann, J. Puczylowski, J. Peinke and M. Hölling
New anemometers for atmospheric flow measurements on different scales
International Conference Renewable Energy 2030 - Experts' Visions, 01.–02.10.2012, Oldenburg, Germany, 2012

H. Heißelmann, J. Puczylowski, J. Peinke and M. Hölling
New anemometers for atmospheric flow measurements on different scales
DPG Frühjahrstagung der Sektion Kondensierte Materie, 25.–30.03.2012, Berlin, Germany, 2012

H. Heißelmann, J. Puczylowski, J. Peinke and M. Hölling
New anemometers for atmospheric flow measurements on different scales
EUROMECH Colloquium 528, 22.–24.02.2012, Oldenburg, Germany, 2012

H. Heißelmann, M. Hölling, M. Wächter and J. Peinke
Wind velocity measurements using the sphere anemometer
European Wind Energy Conference, 16.–19.03.2009, Marseille, France, 2009

M. Hölling, J. Puczylowski, H. Heißelmann and J. Peinke
New anemometers based on the laser pointer principle
12th EUROMECH European Turbulence Conference (ETC), 07.–10.09.2009, Marburg, Germany, 2009